Inorganic fouling control and removal in oceanic carbon capture via *in situ* mineralization using bipolar membrane electrodialysis (BPMED).

Student:	Hannah van der Wal (4710274)
	MSc. Environmental Engineering
Faculty:	Civil engineering and Geosciences (CiTG)
Thesis committee:	Henri Spanjers (chair)
	Ralph Lindeboom
	David Vermaas
	Rose Sharifian (daily supervisor)

Groningen, 29-11-2021

Inorganic fouling control and removal in oceanic carbon capture via in situ mineralization using bipolar membrane electrodialysis

MSc. Thesis Environmental Engineering

By

H.C. van der Wal

Master of Science

in Civil Engineering

at the Delft University of Technology,

Supervisor:	Rose Sharifian
Thesis committee:	Henri Spanjers (chair)
	Ralph Lindeboom
	David Vermaas

Preface

Before you lies my master thesis titled *'inorganic fouling control and removal in oceanic carbon capture via electrochemical bipolar membrane electrodialysis'*. This thesis was written to fulfil the graduation requirements for the master's in civil engineering of the Delft university of technology (Environmental Engineering track).

The research was carried out at Wetsus *'European centre of excellence for sustainable water technology'*. Wetsus provided many possibilities regarding the lab setup and an encouraging workplace, with a lot of inhouse knowledge. My nine months at Wetsus were a great experience.

First, I would like to thank my daily supervisor, Rose. For investing her time in me, for being critical but respectful, to encourage me to growth during my master thesis. I want to thank my thesis committee making time to have meetings with me and providing me advice and direction.

Research in CO_2 capture has never been more crucial than it is today, which was great motivation to work on this subject every day in the past months. I hope you will have as much fun reading this thesis as I had writing it.

Hannah van der Wal

31 October 2021, Groningen

Abstract

Oceanic CO_2 capture technology can be used as a negative emission technology, or pre-treatment to reduce inorganic fouling (i.e., scaling) potential when further processing seawater. In this work CO_2 from (synthetic) seawater was captured electrochemically via bipolar membrane electrodialysis. Although previous studies showed promising results regarding energy consumption (kJ/mole $CaCO_3$), inorganic fouling in the base compartment of the cell is a drawback, which is why an inorganic fouling control and removal study was done. The effect of applied current density (i = 5, 10, 12.5 and 15 $mA \cdot cm^{-2}$) and flowrate (24 and 72 $mL \cdot min^{-1}$ per compartment) on inorganic fouling build-up and dissolved organic carbon removal was investigated for an AEM-BPM and CEM-BPM cell pair configuration. The build-up of inorganic fouling was lower when using higher flowrate and lower current density (between 5-10 $mA \cdot cm^{-2}$) and for the AEM-BPM configuration. A pronounced advantage of the AEM-BPM configuration over the CEM-BPM was that for the AEM-BPM the configuration electrical energy consumption did not increase over time, were it did in the CEM-BPM configuration (based on the Ohmic resistance increase). For inorganic fouling removal 5 methods were investigated: gas sparging (using CO_2 (g) and air), flowrate increase, backpressure, and acid wash. Acid wash showed the highest recovery of pressure drop and voltage. Combing this method with back pressure decreased the cleaning time, making the method more feasible. As this research was a proof of concept, there are opportunities to optimize the cell performance and inorganic fouling removal.

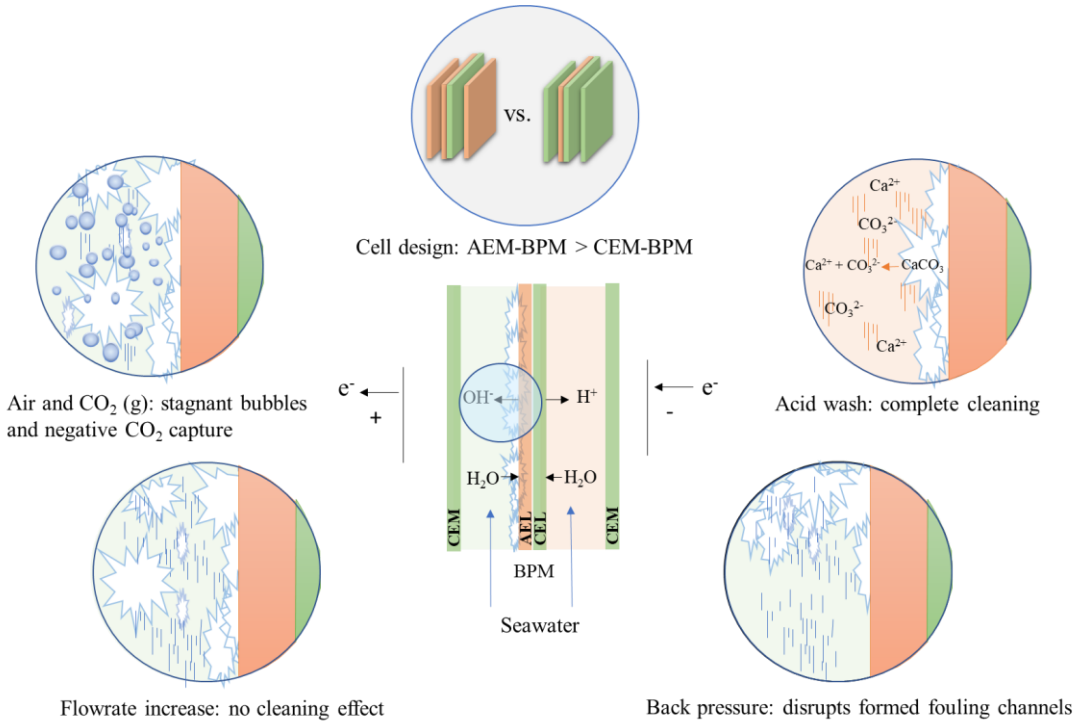

Table of Contents

1. Introduction

1.1. Background

With CO_2 concentrations in the atmosphere increasing, so does our responsibility to capture and convert CO_2 that is derived from human activities (Digdaya et al., 2020). CO_2 (g) is recognized as the main greenhouse gas (GHG) that can be anthropologically controlled to influence climate change (Sharifian et al., 2021a). The Paris agreement has been drawn up to lay down global climate goals (United Nations, 2016). Its overarching climate goal is to keep the increase in the global average temperature below 2 °C above pre- industrial levels. Looking at GHG emissions, around two thirds of the 'available budget' to keep below 2 °C increase, has already been emitted (Rogelj et al., 2016). Therefore, the Paris agreement addresses the necessity of GHG emissions neutrality. In order to achieve this, a balance needs to be found between emission and capture of GHG (Kram et al., 2000). Capture of already emitted GHG can be realized through negative emission technologies (NETs). An important criteria of a NET that *'the quantity of atmospheric greenhouse gases removed and permanently stored is greater than the total quantity of greenhouse gases emitted to the atmosphere'* (Tanzer & Ramírez, 2019).

Negative emission of CO_2 by capture form CO_2 sinks will play an important role in the development of NET's. The ocean is one of the larger CO_2 sinks, storing about 40% of CO_2 emitted by humans since the start of the industrial revolution in the 18th century (Digdaya et al., 2020). CO_2 is stored in seawater as dissolved organic carbon (DIC) and has a concentration of 2.3-2.5 mM (Sharifian et al., 2021a) in equilibrium with the atmosphere, which is 120 times more concentrated than in the atmosphere (Digdaya et al., 2020). CO_2 capture from seawater (or decarbonization of seawater) causes a shift in the carbonate equilibrium. Consequentially, CO_2 from the atmosphere can be absorbed by the alkaline decarbonized seawater, ultimately lowering the concentration in the atmosphere (de Lannoy et al., 2018). Seawater decarbonization can also be useful as a pre-treatment for inorganic fouling prevention in e.g., reverse osmosis for desalination, as seawater is the main source of desalination. Desalination as a 'drought proof' water source has been growing in use over the past 30 years. Global production is currently 100 million cubic meters per year and is expected to double before 2030 due to water shortages (S. Salinas, 2021). Considering membrane fouling is still the main shortcoming for R.O. membrane technology and calcium carbonate ($CaCO_3$) is one of the most common minerals which affects R.O. performance (S. G. Salinas et al., 2021), removing the carbonate as a pre-treatment can reduce this risk.

Electrochemical CO_2 capture from seawater has been reported for various types of electrodialysis designs (Eisaman et al., 2012), (Willauer et al., 2017), (de Lannoy et al., 2018), (Zhao et al., 2020), (Digdaya et al., 2020). Creating a system to capture CO_2 as energy efficiently as possible is a central theme in publications. However, the range in energy consumption is still large. Ranging from 1080–2880 kJ/mole $CaCO_3$ (Zhao et al., 2020) to 330 kJ/mole $CaCO_3$ (Boer, 2020), the latter is lowest achieved energy consumption reported so far (achieved by previous researchers within the overarching PhD project of this thesis).

The carbonate equilibrium is affected by pH, as it effects the dominant DIC form in seawater (H_2CO_3, HCO^- or CO_3^{2-}) (Stumm & Morgan, 1995). Therefore, the pH-swing concept can be used to capture CO_2 in gas or solid form (Figure 1B). The pH swing in this work is electrochemically created, using bipolar membrane electrodialysis (BPMED). A bipolar membrane (BPM) consists of two layers: an anion exchange layer (AEL) and a cation exchange layer (CEL), laminated together. As the layers are of opposite charge, (ideally) only uncharged molecules such as the water molecule can pass through the membrane. Upon applying a sufficient current, the BPM can dissociate water into H^+ and OH^- ions, enabling a pH-swing with a controllable ΔpH over the BPM (Figure 1A).

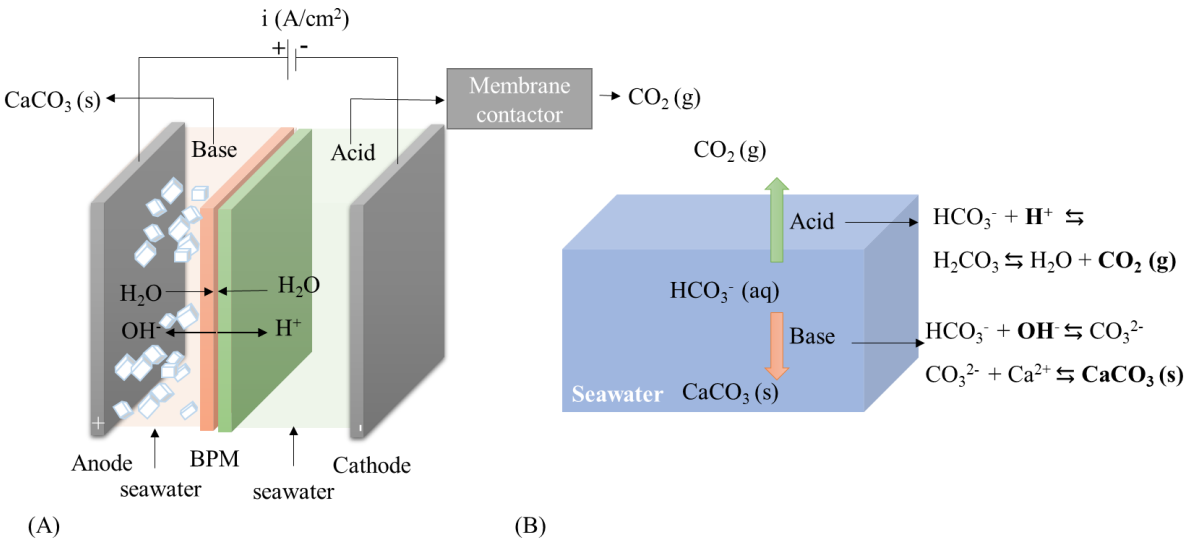

Figure 1, A: Schematic figure of a bipolar membrane (BPM). Water molecules pass the membrane and dissociate into H^+ and OH^- upon application of a sufficient current, creating respectively an acid and a base stream. B: Schematic overview of how the pH-swing concept is used to shift the carbonate equilibrium. The acidic stream converts bicarbonate to carbonic acid and dissolved CO_2 (aq), which can be converted to CO_2 (g), subsequently using a membrane contactor or a vacuum pump (Agrahari et al., 2011). The base stream converts bicarbonate to carbonate, which can react with Ca^{2+} or Mg^{2+} ions and form carbonate minerals precipitation.

In this work, the flux of OH^- and H^+ ions produced by the BPM are added to the seawater directly, as is shown in Figure 1A. An advantage is that the range for the pH-swing can be smaller than for CO_2 capture via ex-situ BPMED, were (de Lannoy et al., 2018) use a ΔpH over the BPM of 0-14, here ΔpH 4-10 is sufficient. Theoretically, creating a smaller ΔpH over the BPM results in lower energy consumption (Vermaas et al., 2018). Furthermore, in the in-situ method no additional chemicals (e.g., NaCl, HCl or NaOH) are required as it is for ex-situ methods (de Lannoy et al., 2018). However, via the in-situ route, mineral precipitation is initiated inside the BPMED cell, which can lead to membrane fouling. This type of fouling is called inorganic fouling (i.e., mineral scaling) and is the focus in this research. Considering the low pH in the acidic channels, it is assumed no inorganic fouling develops in this channel.

Membrane fouling is generally known to shorten the lifetime of membranes (Guo et al., 2015), decrease the process efficiency and increases the process cost (Mikhaylin & Bazinet, 2016). Fouling deposit on or inside an ion exchange membrane (IEM) surface increase the electrical resistance (Pintossi et al., 2019) and decrease perm selectivity (Casademont et al., 2008a). Finally, fouling inside a membrane stack increases the pressure drop, causing increase in pumping energy (Moreno et al., 2017).

In literature, various methods for fouling control and removal are reported. Gas sparging (Moreno et al., 2017) (Vermaas et al., 2014a), chemical wash (Guo et al., 2015), osmotic shock (Vermaas et al., 2014a), flow rate increase and pre-treatment (Vital et al., 2021) are used. Fouling control or removal for in-situ CO_2 capture via BPMED has not been reported on.

1.2. Objective and research questions

The goal of this research is to investigate inorganic fouling control and removal in the base compartments during In-situ CO_2 capture from (synthetic) seawater via bipolar membrane electrodialysis (BPMED). Under inorganic fouling control, we consider choices made while designing a BPMED system to mitigate inorganic fouling. The influence of cell pair configuration, applied current density and flowrate on inorganic fouling build-up inside the BPMED cell were researched. Regarding inorganic fouling removal, five methods were tested: gas sparging (using CO_2 (g) and air), flowrate increase, backpressure and acid wash using hydrochloric acid and acid produced by the BPM.

Based on this goal, the following research questions are answered:

1. What is the effect of flow rate (i.e., cell resident time) on DIC removal and build-up of inorganic fouling under constant current density?

2. Which of the following cell pair configurations is more effective regarding energy consumption (in kJ/mole $CaCO_3$) and inorganic fouling build-up: CEM-BPM or AEM-BPM?

3. Which of the following methods are more effective to remove inorganic fouling: (1) air sparging, (2) CO_2 sparging (3) flowrate increase (4) applying backpressure and (5) acid wash?

Which leads to the overarching research question:

'What combination of the above-mentioned cell design and inorganic fouling removal methods results in the lowest energy consumption (in joule/mole $CaCO_3$) in this BPMED system for oceanic carbon capture?'

To answer the research questions, a combination of literature research, simulations and laboratory research was used. First, a background on involved theory is given in chapter 2: theory. Thereafter the methods and materials used for the simulations and laboratory research are described in chapter 3:materials and methods. Then, results and discussion will be presented in section chapter 4: results and discussion. Finally, the conclusions of this research and future recommendations are shown in chapter 5 and chapter 6.

2. Theory

This chapter reports on how bipolar membrane electrodialysis (BPMED) can be used to capture carbonate from the seawater. Also, membrane fouling is discussed, and finally methods to remove fouling.

2.1. Principle of carbon capture trough Bipolar Membrane Electrodialysis (BPMED)

2.1.1. Carbonate equilibrium

When gasses and liquids are in contact with each other, the gasses partly dissolve in the liquid. The extent of this interaction is related to the partial pressure of the gas. In equilibrium, the concentration of dissolved CO_2 is proportional to the partial pressure of CO_2 in the gas phase and is described by Henry's law (Stumm & Morgan, 1995):

$$[CO_2(aq)] = K_0 \cdot p_{co_2(g)} \qquad \textbf{Equation 1}$$

In which K_0 is Henry solubility of the CO_2(g) ($3.3 \cdot 10^{-2}$ mol·L^{-1}·atm^{-1} for a salinity of 3.5% (Teng et al., 1996)) and $p_{CO2(g)}$ the partial pressure of CO_2(g) ($10^{-3.38}$ atm based on 420 ppm). The carbonate equilibrium has a dependency on pH. Depending on the pH value, dissolved carbonate exists in three forms (Stumm & Morgan, 1995):

1. Dissolved CO_2 (aq) and carbonic acid, where: $H_2CO_3^* = CO_{2(aq)} + H_2CO_3$
2. Bicarbonate ion: HCO_3^-
3. Carbonate ion: CO_3^{2-}

The effect of pH on the dominant carbonate form is shown in Figure 2. Dissolved carbonate is expressed as dissolved inorganic carbon (DIC) and its concentration is a summation of the three above mentioned carbon species, in a pure CO_2-H_2O system (Stumm & Morgan, 1995):

$$DIC = [H_2CO_3^*] + [HCO_3^-] + [CO_3^{2-}] \qquad \textbf{Equation 2}$$

In a closed system, the total concentration of DIC remains constant, though the dominant species varies (Figure 2). The figure shows that for average sweater, bicarbonate will be the dominant DIC species.

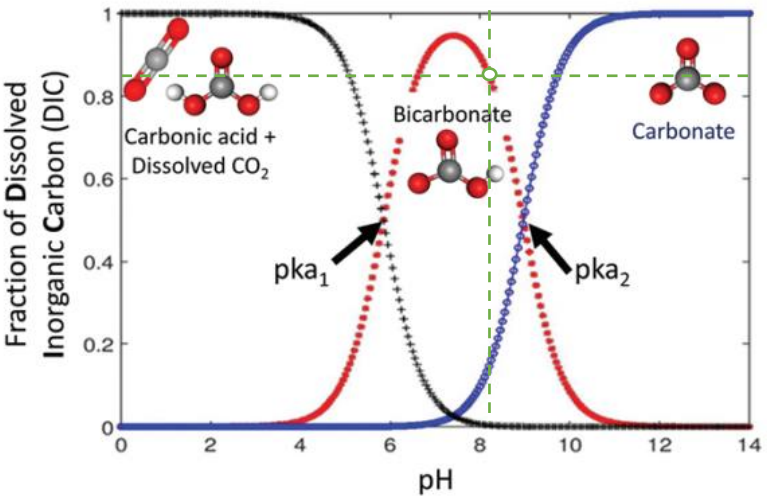

- Average pH seawater ~ 8.1.

Figure 2, Fraction of dissolved inorganic carbon (DIC) dependent on pH, for a closed system. (Temperature: 25 C and salinity of 35 ppt). At pKa_1 $[H_2CO_3] = [HCO_3^-]$ and at pKa_2 $[CO_3^{2-}] = [HCO_3^-]$. Figure adapted from: (Sharifian et al., 2021a).

In an open system, the DIC concentration increases with pH, as more CO_2 (g) dissolves in the solution at base pH. When the systems pH decreases, carbonic acid and dissolved CO_2 are the dominant DIC form (Sharifian, Wagterveld, et al., 2021). Dissolved CO_2 can leave the system as CO_2 (g) (Stumm & Morgan, 1995):

$$HCO_3^- + H^+ \leftrightarrows H_2CO_3 \qquad \textbf{Equation 3}$$

$$H_2CO_3 \leftrightarrows CO_2(aq) + H_2O \qquad \textbf{Equation 4}$$

$$CO_2(aq) \leftrightarrows CO_2(g) \qquad \textbf{Equation 5}$$

2.1.2. Mineralization

When the systems pH increases, carbonate is the dominant DIC form. Carbonate can precipitate and leave the system as a mineral if combined with cations (e.g., Ca^{2+} and Mg^{2+} ions). For minerals precipitation to be thermodynamically possible, the saturation ratio (Ω) needs to be > 1 (La Plante et al., 2021) or the saturation index (SI) > 0:

$$\Omega = \frac{IAP}{K_{sp}} \qquad \textbf{Equation 6}$$

$$SI = \log(\Omega) \qquad \textbf{Equation 7}$$

In which IAP is the ion activity product (IAP = $\{Ca^{2+}\}\cdot\{CO_3^{2-}\}$ for $CaCO_3$) and K_{sp} the solubility product ($K_{sp} = [Ca^{2+}]_{eq}\cdot[CO_3^{2-}]_{eq} = 4.39\cdot10^{-7}$ molality^2 (Zhong & Mucci, 1993) for

$CaCO_3$). The activity product of CO_3^{2-} ions drives the calcite precipitation in seawater. Since the concentration of CO_3^{2-} ions is pH dependent (Figure 2), so is the IAP value. For mineral precipitation to contribute to the decarbonization of seawater, the pH needs to be adjusted to a range in which precipitation of carbonate containing minerals is dominant. The saturation index of all thermodynamically possible minerals in synthetic seawater vs. pH was simulated (using Visual MINTEQ 3.1) by (Sharifian et al., n.d.) Figure 3:

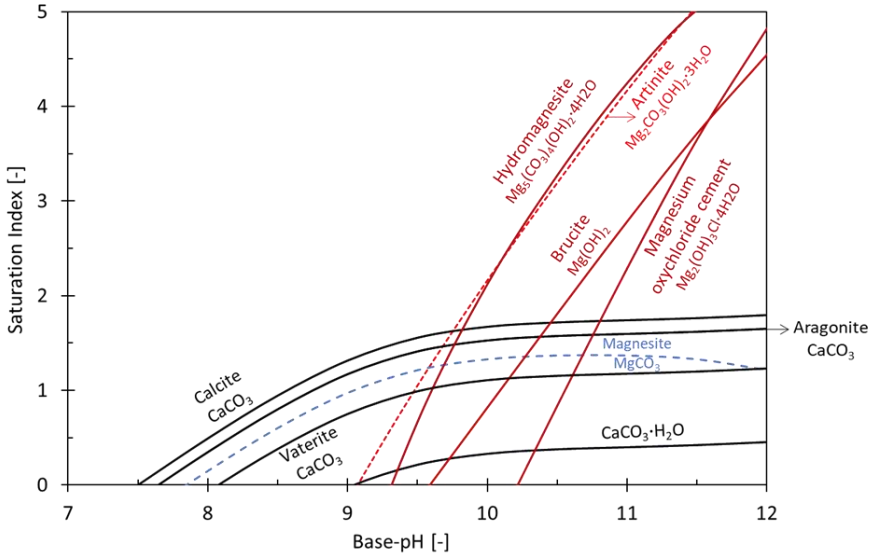

Figure 3, The saturation index (SI) of all thermodynamically possible minerals in synthetic seawater vs. the base-pH, determined by Visual MINTEQ 3.1 at 25°C for a closed system. Red lines show hydroxide containing minerals, black calcium carbonate, and blue magnesium carbonate (the latter is unlikely to precipitate at temperature < 75 ℃, but kinetics at low temperature is not well known enough to exclude it from this figure). Calcium hydroxide $Ca(OH)_2$ is undersaturated at pH < 12. Precipitation of $CaMg(CO_3)_2$, and Huntite $Mg_3Ca(CO_3)_4$ is thermodynamically possible, but the kinetics are slow for these circumstances and therefore exclude from this figure. Figure from: (Sharifian et al., n.d.).

The SI index of Calcite polymorphs does not increase much anymore after pH 9.5, but from pH > 10 the SI index of hydroxide containing minerals e.g., $Mg(OH)_2$ increases rapidly, which is undesirable for this case (as the aim is to remove carbonate). Therefore, the aimed pH window for precipitation of carbonate containing minerals is 9.5-10.

Precipitation of minerals can be divided in two stages of nucleation and precipitation (Mercer et al., 2005). Nucleation is the transition of dissolved ions e.g., Ca^{2+} and CO_3^{2-} ions into solid phase, in oversaturated solutions. The nucleation is the time consuming and energy intensive stage. In the growth stage these ions precipitate onto already existing minerals. So once mineral scaling has precipitated inside the cell, the energy barrier for Ca^{2+} and CO_3^{2-} ions is lower to precipitate onto the existing minerals since they can skip the nucleation phase (Stumm & Morgan, 1995).

If mineral precipitation can happen in a certain environment is decided by thermodynamics, if it happens and how fast by kinetics. When the saturation ratio (Ω) just exceeded 1 (Equation 6), precipitation is thermodynamically possible, but due to kinetics a higher saturation ratio might be needed for precipitation to take place. The zone between Ω = 1 and Ω where precipitation is guaranteed is revered to as the metastable zone. How this affects mineral precipitation is shown in Figure 4.

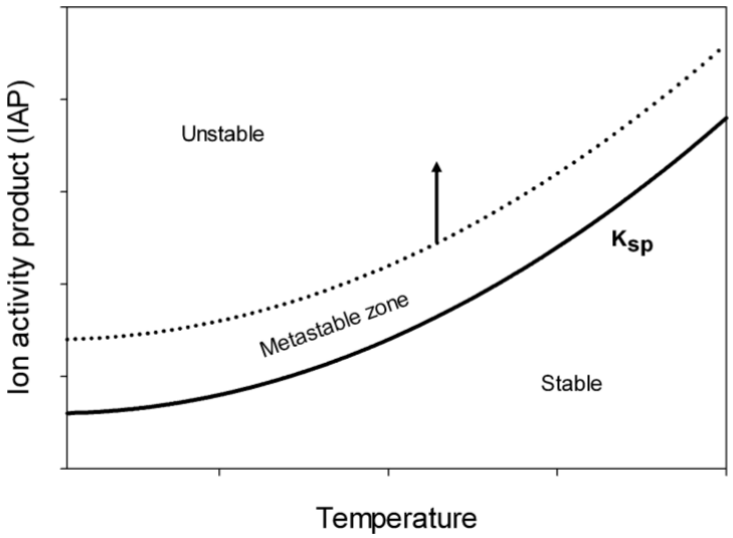

Figure 4, Schematic figure of the metastable zone. Below the K_{sp} line (solubility product) the solution is under saturated, and no mineral precipitation can take place. Above dotted, the solution is supersaturated and both nucleation and crystallization will happen. In the metastable zone, the solution is oversaturated, and mineral precipitation is thermodynamically possible, but is not a guarantee due to kinetics. Figure from: (Wagterveld, 2013).

The presence of other ions in synthetic seawater also influences mineral precipitation. A well-known example is the precipitation of calcite vs. aragonite in seawater. Even though calcite is less soluble than aragonite, precipitation of aragonite is favourable over calcite in the presence of Mg^{2+} ions (and with the Mg:Ca ratio in seawater) (Sun et al., 2015), against expectations based on Figure 3.

The reaction time (in seconds) for $CaCO_3$ to precipitate was determined at 25℃, pH = 6 and under well-mixed conditions (La Plante et al., 2021):

$$HCO_3^- + OH^- \leftrightarrows CO_3^{2-} + H_2O \qquad t = 10^{-2}\ s \qquad \textbf{Equation 8}$$

$$CO_3^{2-} + Ca^{2+} \leftrightarrows CaCO_3\ (s) \qquad t = 10^{3}\ s \qquad \textbf{Equation 9}$$

The time (t) in seconds (s) the time between the moment supersaturated conditions are reached and formation of critical nucleus or detectable crystals (S. Salinas, 2021), showing that the mineral precipitation is the rate limiting step during in-situ mineralization of bicarbonate.

2.1.3. Bipolar membrane electrodialysis (BPMED)

A bipolar membrane (BPM) is a polymeric membrane that consists of two membrane layers: an anion exchange layer (AEL) and a cation exchange layer (CEL), laminated together, with a catalyst layer in between. Under application of an electric field, water molecules dissociate into hydrogen ions (H^+) and hydroxide ions (OH^-) because of the enhanced water dissociation reaction due to the catalyst. Subsequently, H^+ ions can leave the BPM through the CEL and OH^- ions through the AEL, creating acid and base solutions in the compartments (Figure 5).

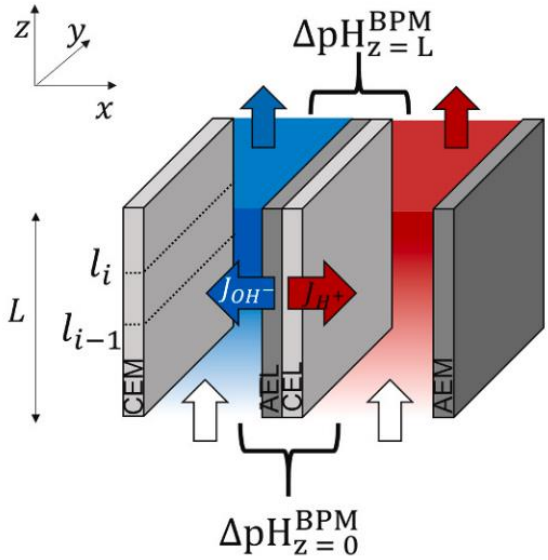

Figure 5, Schematic overview of the principle of water dissociation of a bipolar membrane with Co-current; upon application of a sufficient current, acid (H^+) and base (OH^-) are produced from water molecules. ΔpH is close to zero at z=0 but will increase fast when z increases. Figure adapted from (Sharifian et al., 2021b).

For water dissociation to be initiated, both layers of the BPM first need to be depleted of ions, building up the potential inside of the BPM. In practice, the minimum current required for the water dissociation to be the main charge carrier through the BPM is referred to as the limiting current density (Pärnamäe et al., 2021). The limiting current density depends on the BPM and the electrolyte around it but is measured to be around 2.5 $mA \cdot cm^{-2}$ for the Fumatech membrane used in our work (in 0.5 M NaCl).

To what extent these fluxes of ions occur over the AEL and CEL is described by the Nernst-Planck equation (Pärnamäe et al., 2021):

$$J = -D_{i,m}\left(\frac{dc_{i,m}}{dx} + z_i c_{i,m}\frac{d\varphi}{dx}\right) \quad \textbf{Equation 10}$$

In which J is the molar flux ($mol \cdot m^{-2} \cdot s^{-1}$), $D_{i,m}$ the ion diffusion coefficient in the membrane, $c_{i,m}$ the ion concentration in the membrane compartment, z_i the ion valence, and Φ the (dimensionless) electric potential, x is the position from the membrane surface. When working with a continuous flow and there is sufficient mixing in the compartment, $c_{i,m} \sim 0$.

Assuming an ideal membrane (which is 100 % selective and excludes all co-ions and all applied current does into water dissociation), and assuming a columbic efficiency of 100 % for the BPM, the relation between the applied current density (i) and the flux of H^+ and OH^- ions is describes as (Sharifian et al., 2021b):

$$J_{H^+} = J_{OH^-} = \frac{i}{zF} \quad \textbf{Equation 11}$$

In which i the applied current density ($A \cdot m^{-2}$), z is the ion valence (+1 for H^+ ions and -1 for OH^- ions) , F the faraday constant ($C \cdot mol^{-1}$), and J the molar flux of the produced H^+ or OH^- ions ($mol \cdot m^{-2} \cdot s^{-1}$). When the flux is known, the mass balance of the BPMED system becomes (Sharifian et al., 2021b):

$$C_{out} \cdot q_{out} = C_{in} \cdot q_{in} + JA \quad \textbf{Equation 12}$$

In which C in the contraction of H^+ or OH^- ions in the outlet from the compartment ($mol \cdot L^{-1}$), q the flow rate of the feed ($L \cdot s^{-1}$), J the flux for the produced H^+ or OH^- ($mol \cdot m^{-2} \cdot s^{-1}$) and A the surface area of the membranes (m^2). Considering the definition of pH, the pH in the membranes compartment would be directly controlled by the applied current density and the flow rate. Though, this only applies when all current results in water dissociation, the BPM selectivity has a 100% efficiency, and the solution has no buffering properties.

Equation 12 can be used to estimate the bulk pH but in reality, pH in the compartments next to a BPM is not uniform. Concentration changes in are most pronounced near the membrane surface, in the diffusion boundary layer (Vermaas et al., 2014b). For water dissociation, this means that near the membrane surface the pH could be higher/lower than the measured bulk pH and is revered to as local pH. This is more severe at lower flowrates, as higher flowrates

enhance mixing of this boundary layer more, decreasing its thickness which should be proportional to the flow velocity ($v^{1/3}$) if Reynolds number < 1000 (Vermaas et al., 2018). The use spacers in the compartment also enhances mixing of this layer (Vermaas et al., 2014b). Looking back at Figure 3, local pH can interfere with the thermodynamics of calcium carbonate since the SI index for hydroxide containing minerals increases fast from pH>10.

2.1.4. Energy consumption

Multiple aspects contribute to the energy consumption of a BPMED system. The total cell voltage is a main contributor to the energy consumption can be expressed as (Sharifian et al., 2021a), (Pärnamäe et al., 2021):

$$V_{cell} = V_{redox} + V_{WDR} + \eta_{non-ohmic} + iR_{Ohmic} \quad \textbf{Equation 13}$$

$$V_{WDR} = 0.059 \cdot \Delta pH \quad \textbf{Equation 14}$$

$$R_{Ohmic} = R_{membranes} + R_{compartments} \quad \textbf{Equation 15}$$

The redox voltage (V_{redox}) depends on the choice of electrodes and the electrode rinsing solution. The thermodynamic voltage required for water redox to produce O_2(g) and H_2(g) at pH = 0 , is 1.23 V (Veerman et al., 2010). When using reversible redox couple, such as iron the voltage is 0, decreasing the total cell voltage and thus the final energy consumption (Veerman et al., 2010). V_{WDR} is the thermodynamic energy consumption for the water dissociation dependent on the pH gradient over the BPM. $\eta_{non\text{-}ohmic}$ is the overpotential such as that of the water dissociation at the BPM, concentration polarization and redox-overpotential. i is the applied current density in ($A \cdot m^{-2}$), R_{Ohmic} is the ohmic resistance ($\Omega \cdot m^2$) which can be divided up into membrane resistance and the resistance of the electrolyte between the compartments. The resistance of the electrolyte ($R_{compartments}$) is a function of the conductivity of the liquid:

$$R_{compartments} = \frac{l}{\sigma \cdot A} \quad \textbf{Equation 16}$$

In which $R_{electrolyte}$ is the resistance of the solution in the compartment (Ω), l the compartment thickness (m), A the membrane surface area (m^2), and σ the conductivity of the electrolyte ($S \cdot m^{-1}$). The membrane resistance can be divided up into resistance of the CEM/AEM and BPM membranes, which in this work are ca. 4 $\Omega \cdot cm^2$ and 8 $\Omega \cdot cm^2$, respectively. When ions move

though the membranes and come across these resistances, that results in an energy loss, usually in the form of heat, and is generate from the friction.

The total energy consumption E (kJ· mol^{-1} DIC) required for the in-situ mineralization is described defined as ((Sharifian et al., n.d.) submitted article, (Moreno et al., 2017)):

$$E = \frac{\int_0^t V\ I\ dt}{m_{DIC}} + \frac{\int_0^t (\Delta P_a + \Delta P_b)\ q\ dt}{m_{DIC}} \qquad \textbf{Equation 17}$$

In which V represents the total cell voltage (V) (Equation 13), I the applied current density (A), integrated over the running time of the experiments in seconds. The second part of the equation describes the pumping energy. In which ΔP_a and ΔP_b are respectively the pressure drop over the acid- and base compartments (in Pa) and q the flowrate ($m^3 \cdot s^{-1}$), integrated over time. The sum of these values is divided by amount of moles $CaCO_3$ produced in the chosen time scale (m_{DIC} in moles DIC).

2.1.5. Cell configuration

A BPM electrochemical cell can have many different configurations using BPM, AEM and CEM. In this work, investigations are done on AEM-BPM and CEM-BPM cell-pairs configuration. None of the configuration are optimal with regards to the co-ion transfer as an AEM-BPM cell pair allows migration of OH^- ions to the acid compartment and CEM-BPM allows H^+ ions migration to the base compartment, decreasing the pH in the base compartment. Other cations and anions also transfer over the CEM and AEM, to which extent can be estimated by the Nernst-Planck equation (Equation 10). Alternative configurations that do not allow these transfers (Eisaman et al., 2011), (Iizuka et al., 2012), though more membranes are needed to create the same number of acid and base compartments. Each added membrane adds to the overall costs and energy consumption of the cell.

2.2. Fouling

In this section the types of fouling are discussed, followed by how fouling can be detected, the effect of cell design and finally fouling removal methods.

2.2.1. Types of fouling

Fouling is undesirable attachment of solids to the membrane or spacers surface. Fouling can be classified into four main types (Mikhaylin & Bazinet, 2016). (1) Colloidal fouling originates from non-dissolved suspended solids (e.g., clay minerals, colloidal silica, iron oxide). Colloidal particles have a net change, when this change is opposite from the charge of the IEM, conditions for colloidal scaling are favourable. (2) Organic fouling has similar characteristic from colloidal

fouling, though the organic substances that form the fouling are dissolved, were colloidal fouling is non-dissolved. Organic fouling originates from e.g., carbohydrates, proteins, or humic acid. (3) Biofouling develops by interaction of bacteria with the membrane surface and subsequent bacterial growth. This type of fouling is also known as biofilm. (4) Inorganic fouling also known as scaling occurs when minerals precipitate and settle on the membrane surface or within the membrane channels (e.g., $CaCO_3$ or $Mg(OH)_2$).

Due to the composition of the synthetic seawater used in this work, inorganic fouling (i.e., scaling) is the main fouling type and the type of fouling that we will focus on.

1.2.1 Fouling detection

The pressure drop between the inlet and outlet of the cell (incl. acid and base compartments) over time (Vital et al., 2021), (Vermaas et al., 2014a), (Moreno et al., 2017), (Ngene et al., 2010), the increase of the cell voltage over time, and the increase in Ohmic resistance using interval chrono potentiometric experiments can be used to detect fouling in membrane-based systems (Vermaas et al., 2014c), (Pintossi et al., 2019). Such measurements does not provide information about location of fouling, as it says something about the overall behaviour of the cell (Pintossi et al., 2019). As shown in Equation 13, Ohmic resistance drops to zero as soon as the applied current (i) goes to zero, where non-ohmic resistance decreases more slowly. This can be revealed by a chrono potentiometric curve (Figure *6*).

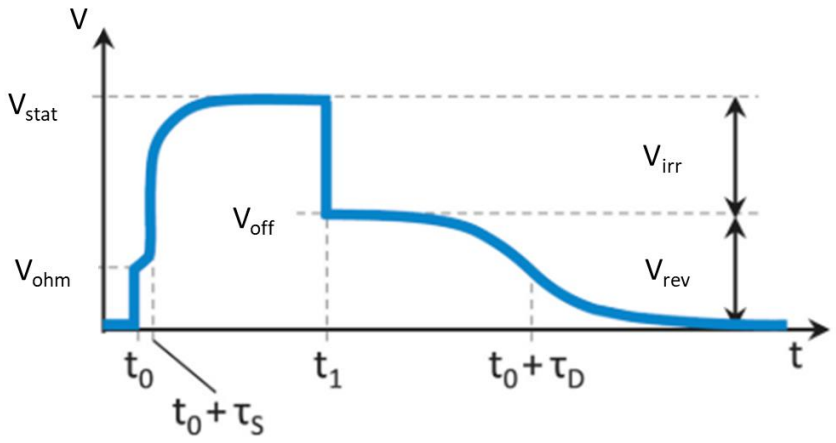

Figure 6, Example of chrono potentiometric series, at over limiting current density. The stack voltage (V) is plotted vs. time, revealing the voltage needed to overcome ohmic (sudden voltage drop) and non-ohmic resistance (slower decrease). Figure adapted from (Pärnamäe et al., 2021).

The value of V_{irr} (irreversible voltage) reveals to the ohmic resistance of the bipolar membrane.

Fouling influences the total energy consumption (Equation 17). Increase in pressure drop increases the needed pumping energy (Moreno et al., 2017) and increases the cell voltage, due

to the higher resistance as a consequence of fouling, increasing the energy consumption subsequently (Pintossi et al., 2019).

1.2.2 Fouling and cell design

The cell design can influence the fouling build-up. The presence of feed spacers in the channels increase the potential of inorganic fouling, since it creates more surface to precipitate on (Ngene et al., 2010). Besides, fouling can accumulated at places in the compartment were the flow velocity is low, such as in spacer knits (Vermaas et al., 2014c), (Vrouwenvelder et al., 2009). An electrochemical cell with membrane spacers reached an pressure drop of 1.5 bar four times faster than an cell with profiled membranes, for the same conditions, due to fouling on the spacers (Vermaas, et al., 2014a).

For cation exchange membranes (CEM), it appeared that permselectivity was affected under basic conditions (when both Ca^{2+} and Mg^{2+} ions were present), allowing OH^- to transfer through. Consequentially, precipitation with OH^- ions and cations could occur, as both pass through the membrane and with cations near the membrane surface (Casademont et al., 2008a). Fouling on AEM was reported also, but this was attributed to operational conditions (Casademont et al., 2008b).

1.2.3 Fouling removal

Physical cleaning is often implemented through application of *wall shear stress* on the membrane and channel surfaces at which fouling is attached. Wall shear stress in measured in applied force per surface area and is for Newtonian fluids generally expressed as (Elger, 2012):

$$\tau_w = \mu \frac{\partial u}{\partial y} \qquad \textbf{Equation 18}$$

In which u is the flow velocity in the membrane compartment and y is the height above the boundary (the membrane surface). (Elger, 2012). Equation 18 shows that higher flowrate leads to a higher velocity gradient which leads to a higher wall shear stresses. In narrow rectangular channels, wall shear stress can also be expressed as function of pressure drop (Son, 2007):

$$\tau_w = \frac{R}{2} \cdot \left(\frac{\Delta P}{l}\right) \qquad \textbf{Equation 19}$$

Where R is the capillary radius, l the length of channel and ΔP the pressure drop (Pa). Increasing wall shear stress to removal fouling can be done by increasing the flowrate, which lead to (partly) fouling removal (Berre & D, 1996), (Goode et al., 2013) or gas sparging (Wibisono, 2014).

Gas sparging to mitigate fouling in membrane processes is reported in various cases in literature. Various factors are important including the sparging regime, pressure and flow type. Conditions for various methods and membrane types are shown in Table 1. Used gasses that were reported are air, CO_2 and N_2 gas. CO_2 sparging also has properties of chemical cleaning, since CO_2 gas lowers the pH and increases DIC concentrations in the feedwater when it dissolves into the feedwater.

Table 1, Gas sparing experiments from literature for different membrane types and different gasses to get inside in different sparging regimes and flow types.

Method	Membrane type	Sparging regime	Pressure	Flow	Results	Source
Air sparging	Ion exchange membrane (RED)	Every 30 min - 30 s	Not reported	Air flow dominated	Pressure drop decrease 91% compared to blank.	(Vermaas et al., 2014a)
Air sparging	Ion exchange membrane (RED)	Every 30 min - 1 x 6s or 3x 2s	Not reported	Not reported	3x 2s : NPD: ~ 0 1 x 6s : NPD*****: - 1.6 $W \cdot m^{-2}$ blank NPD :~ -2 $W \cdot m^{-2}$	(Moreno et al., 2017)
CO_2 nucleation	Ion exchange membrane (RED)	Every 30 min - 1 x 6s or 3x 2s	CO_2 saturated demi-water under 0.5 bar overpressure	Bubble nucleation	3x 2s NPD: > 0 1x 6s NPD: ~ -1 $W \cdot m^{-2}$ Blank NPD: ~ -2 $W \cdot m^{-2}$	(Moreno et al., 2017)
Air sparging	Membrane bioreactor (MBR)	Every 30 min - 15 s	2.45-2.85 bar	$r_{g/l}$****** =0.47 - 0.58	Increased flux up to 200% Higher gas/ air ratio causes higher flux increase, optimum was not found	(Psoch & Schiewer, 2006)
CO_2 nucleation	R.O. + spacer (D_h ~3mm)	15 minutes	CO_2 saturated milli-Q under 1 bar overpressure	Bubble nucleation	Hydraulic pressure recovered 100% compared to the clean membranes	(Ngene et al., 2010)
N_2 sparging	R.O. + spacer (D_h ~3mm)	15 minutes	1 bar overpressure	$r_{g/l}$ = 0.00160	Hydraulic pressure recovered 85%	(Ngene et al., 2010)
N_2 sparging	Variety of spacers	-	Not reported	$r_{g/l}$ =0.067 - 0.5	Gas/liquid ratio 0.11 showed best bubble distribution for spacer D_h 1.36 mm	(Willems et al., 2009)

* NPD: Net power density

** $r_{g/l} = \frac{v_{gas}}{v_{gas}+v_{liquid}}$, v_{gas} in $m \cdot s^{-1}$, v_{Liquid} in $m \cdot s^{-1}$

In the work of (Moreno et al., 2017) it was shown that that introducing pulses of gas during sparging is more effective than introducing the same amount of gas at once, as the 3x 2seconds regime showed better results than 1 x 6 seconds (Table 1). By applying gas in pulses, both air and liquid are brought into the compartments at the same time to general both wall shear stress and drag force (Elger, 2012) (the force in the flow direction to transport fouling removed from the membrane surface out of the cell). It was also found that air bubbles can get stuck inside the compartment (referred to as stagnant bubbles), which was detected by increase of ohmic resistance. Application of backpressure was used to release those bubbles, by temporary closing the cells outlet using a valve (allowing pressure to build-up) and upon opening the valve, the bubbles were released.

Chemical cleaning is reported as a fouling removal method for different kind of membranes (Guo et al., 2015). In the case of inorganic fouling removal, circumstances should be created in which the mineral precipitates go into dissolution. By lowering the pH, CO_3^{2-} is no longer the dominant carbonate form (Figure 2). Lowering the pH in definition means increasing the concentration of H^+ ions. H^+ ions react with CO_3^{2-} ions to form HCO_3^- or H_2CO_3. Acids that were reported in literature as a cleaning agent for the removal of inorganic fouling from ion exchange membranes were Ethylenediaminetetraacetic acid (EDTA), citric acid and hydrochloric acid (Mikhaylin & Bazinet, 2016). Since the BPMED systems also produce an acid stream, this can provide an opportunity for chemical cleaning without addition of extra chemicals. The pH is lowered, but this acid does contain Ca^{2+} and Mg^{2+} ions, which is thermodynamically not favourable if minerals containing these elements need to be dissolute, as it increases the saturation index (Equation 7).

3. Material and methods

A combination of experiments and simulations (using Visual MINTEQ 3.1) were used to answer the research questions and achieve the goals of this research. Visual MINTEQ is a free equilibrium speciation model, which calculates the chemical equilibria in the aqueous systems at a low ionic strength (I < 1).

3.1. Simulations

Visual MINTEQ 3.1 was used to simulate the influence of the applied current density on the pH and $CaCO_3$ production. The feed (synthetic seawater) composition used in the experiments and the simulations is shown in Table 2. At the start of simulations, the feed was equilibrized with air with a partial pressure for CO_2 (g) of 420 ppm. Concentrations of equilibrized synthetic seawater, which has a pH of ~8.1, were used as input values.

Application of current density of i = 5, 10, 12.5 and 15 $mA \cdot cm^{-2}$ for a flowrate of 72 and 24 $mL \cdot min^{-1}$ per compartment (i.e., cell residence time (t_r) of 10 and 3.33 seconds respectively) was simulated. Equation 11 was used to determine the total flux of OH^- and H^+ ions in $mole \cdot L^{-1}$ over the BPM for each set of current density-flow rate, the cell retention time was used to calculate the average OH^- ions concentration in the base compartments. This increased concentration of OH^- ions in the feed was inserted in Visual MINTEQ 3.1 by decreasing the H^+ ions concentration accordingly. The output values of these simulations were the acid- and base pH in the outlet, the base-pH after precipitation takes place, and the theoretical $CaCO_3$ precipitation.

Ion migration between the compartments through the AEM or CEM was not considered in the simulation. Therefore, no distinction was made between the AEM-BPM and CEM-BPM configuration, since in simulations the results would be the same. For the membranes, 100% efficiency and selectivity was assumed.

3.2. Experiments

3.2.1. Reagents and materials

Two separate feed tanks were used to mimic seawater in the experiments. One feed tank was made by adding ~ 47 $g \cdot L^{-1}$ NaCl, 386 $mg \cdot L^{-1}$ $NaHCO_3$, 1.45 $g \cdot L^{-1}$ KCl, and 7.8 $g \cdot L^{-1}$ Na_2SO_4, while the second tank included ~ 3.0 $g \cdot L^{-1}$ $CaCl_2 \cdot 2H_2O$ and 21.2 $g \cdot L^{-1}$ $MgCl_2 \cdot 6H_2O$ (Sharifian et al., n.d.). Synthetic seawater was mixed in two different tanks, to avoid mineral precipitation prior to the experiments, as the feed is already oversaturated for $CaCO_3$. Right before entering the electrochemical cell these solutions were mixed via a T-connections (using

6mm tubing), thereby diluting the salts with a factor of 2, resulting in the concentrations as in Table 2. Both tanks were left open and stirred over night to equilibrize with air and get to the ambient temperature of 23°C ± 2°C. The used reagents were from VWR or Sigma Aldrich. Before experiments, conductivity, and the pH each tank was measured in $mS \cdot cm^{-1}$ (from WTW) (the aimed and measured values are shown in *Appendix VI – Average values synthetic seawater*).

Table 2, Composition of the synthetic seawater

Ion	**$mol \cdot L^{-1}$**
Sodium (Na^+)	0.459
Magnesium (Mg^{2+})	0.0521
Calcium (Ca^{2+})	0.0102
Potassium (K^+)	0.0097
Chloride (Cl^-)	0.536
Sulphate (SO_4^{2-})	0.0275
Carbonate (CO_3^{2-})	0.00215
Proton (H^+)	0.002

All charged membranes were from FuMATech B.V. The FBM-130, FKB-PK-130 and FAB-PK-130 were used as the BPM, CEM and AEM membranes, respectively and had a surface of 100 cm^2 (10 cm x 10 cm). 400 µm compartments were created with integrated gasket-spacers provided by Aqua Battery B.V. (making one compartment 4 cm^3 or 4 mL). Titanium mesh electrodes coated by platinum from MAGNETO Special Anodes B.V. (Schiedam, The Netherlands) were used. The pumps were from Masterflex® , the power supply from Delta Elektronika and a potentiostat from Ivium Technologies B.V. The pressure drop between the in- and outlets of the cell was measured using a pressure difference transmitter (Endress + Hauser, type Deltabar S, Germany). Measured values were logged and saved using data logger (Endress + Hauser, Ecograph T, Germany). CO_2 (g) and air were extracted from gas pipes present in the lab, available at a pressure range of 0.5-7 bar. An automated valve was used for the gas which could be opened and closed according to a pre-set interval and duration. 0.3M

Na_2SO_4 was used as electrode rinsing solution with a conductivity of 38.3 $mS \cdot cm^{-1}$ resulting in a resistance of (R_{Na2SO4} = 0.0004m/3.83 $S \cdot m^{-1}$ = 0.0104 Ω) and a starting pH of 5.9.

3.2.2. Inorganic fouling control

First, the influence of cell residence time and current density on inorganic fouling development, carbonate removal, and energy consumption via the base route was researched for two cell pair configurations (AEM-BPM and CEM-BPM). Four different current densities (5, 10, 12.5 and 15 $mA \cdot cm^{-2}$) in combination with two different flowrates of 24 and 72 $mL \cdot min^{-1}$ per compartment (i.e., cell residence time (t_r) of 10 and 3.33 seconds respectively) were applied. The velocity for the flowrate 24 and 72 $mL \cdot min^{-1}$ per compartment was 1 $cm \cdot s^{-1}$ (24 $mL \cdot min^{-1}$ = 0.4 $cm^3 \cdot s^{-1}$, 0.4 $cm^3 \cdot s^{-1}$ / (10 cm length · 0.04 cm width) = 1 $cm \cdot s^{-1}$) and 3 $cm \cdot s^{-1}$, respectively.

The experiment time was 30 minutes. The applied current density and flowrate were kept constant during the experiments. The inorganic fouling build-up was measured through:

- Development of pressure difference (ΔP in mbar) between the base compartments in- and outlet over time (recorded every second).
- Development of the total stack-voltage over time (recorded every second). The voltage of the water redox in the compartments with electrode rinsing solution was measured with reference electrodes and not included in the total stack-voltage.
- The ohmic resistance of the cell stack, measured via current interruption. This procedure is described in *Appendix I – Determination of Ohmic resistance.*

The current was applied using a potentiostat with. Per experiment, 1 L of the outflow of the base channel was captured and stored in closed bottles for at least 72 hours to allow mineral precipitation. Capture of the outflow was done no earlier than 15 minutes after the current was turned on. Thereafter, the sample was filtered through a 0.22 μm (MF-Millipore™) filter and analysed on Ca^{2+} and Mg^{2+} ion concentrations using inductively couples plasma analysis (ICP). The carbonate concentration in the filtered sample was determined via hydrochloric acid titration, with procedure described in *Appendix II – Titration for DIC Concentration Approximation.*

The cell design for the CEM-BPM configuration is shown schematically in Figure 7. The membrane stack consisted of 3 cell pairs. The cells channels were created using woven spacers with a width of 400 μm. A cation-exchange membrane was used as a shielding membrane on the anode side, to avoid chlorine leakage to the electrode rinsing solution.

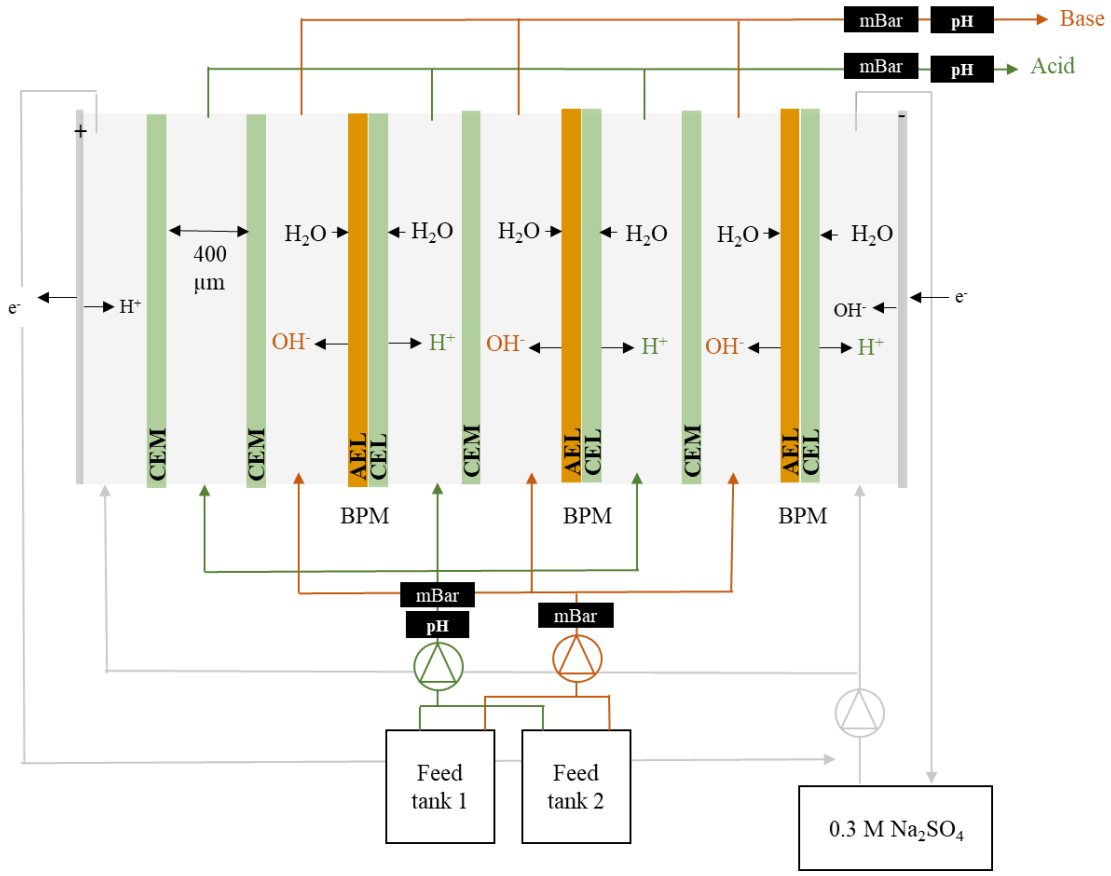

Figure 7, schematic representation of the BPMED CEM-BPM cell configuration. The with of the channels is 400 µm (using Integrated gasket-spacers provided by Aqua Battery B.V), making each compartment 4 cm^3 or 4 mL.

The cell design for the AEM-BPM configuration is similar as in Figure 7, but with 3 BPM-AEM cell pairs and a CEM as shielding membrane on the anode side (a schematic picture is shown in Appendix III – AEM-BPM cell pair configuration).

3.2.3. Inorganic fouling removal

Experiments were done under the *"worst case scenario"* circumstances where the membranes were *"pushed into fouling",* meaning circumstances were created in which a relatively rapid inorganic fouling build-up per time was measured. To do so, the combination of 12.5 $mA \cdot cm^{-2}$ for a flowrate of 72 mL·min-1 per compartment was used and kept constant during the experiment. The experiment time was 1 hour. All inorganic fouling removal experiments were done with a 3 CEM-BPM cell pair configuration (except the acid wash). The schematic cell design is similar to the configuration shown in Figure 7, but had 2 CEM shielding membranes (*Appendix IV – Inorganic fouling removal cell* design).

The efficiency of the methods were determined trough the voltage-time and pressure drop-time curves, which were measured and logged every second.

All outflow of the base (~ 13 L) was captured and stored in closed of containers, samples were left to precipitate for > 72 hours. Measurements of Ca^{2+} and Mg^{2+} ions and DIC removal were done the same as described in section *3.2.2 Inorganic fouling control*.

3.2.4. Gas sparging: air and CO_2(g)

Gas sparging experiments were done with both (atmospheric) air and CO_2 (g). The gas was integrated into the feed using a T-joint (using 6mm tubing). Figure 8 shows the experimental set-up schematically. Gas pressures of 2, 3 and 4-bar were used. The interval of sparging was every 10 minutes, with the first *"sparge"* 5 minutes after the experiment started. This regime was chosen to apply gas sparging before the pressure drop and voltage increase more than 5%, which was determined based on experiments shown in *Appendix V – Interval determination*. Gas sparging was done for the base compartments, acid compartments were not sparged. The applied current density was not turned off during sparging.

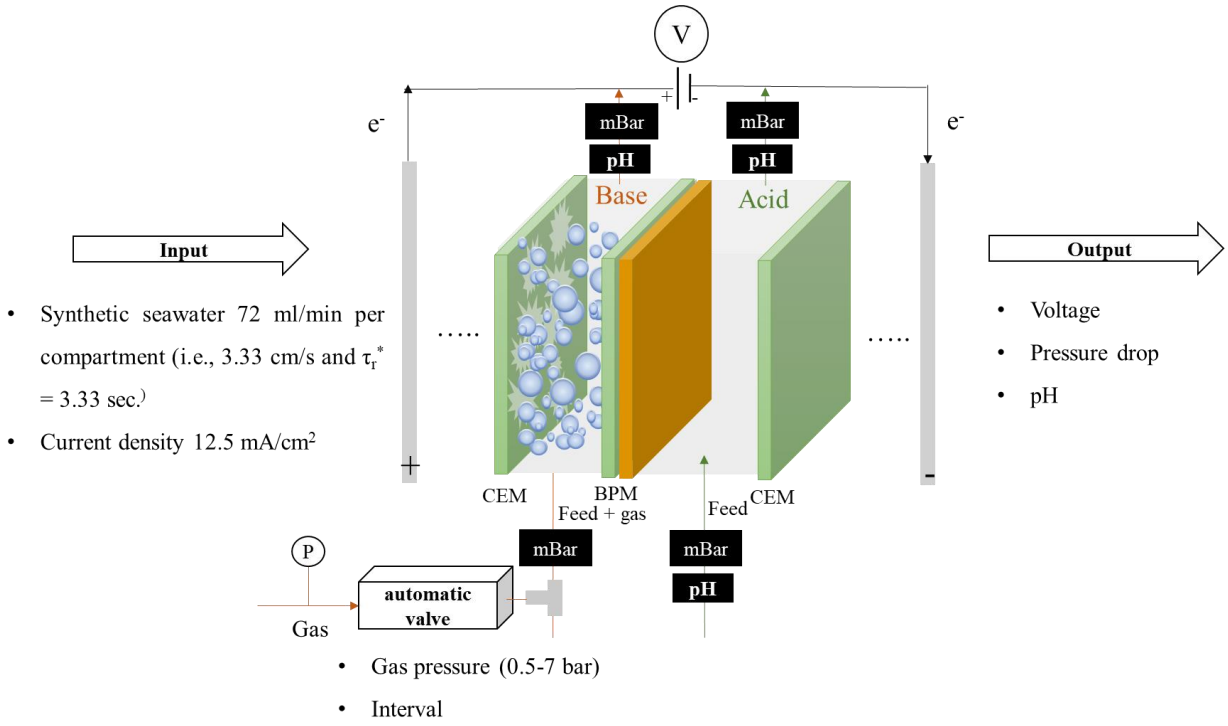

Figure 8, Schematic of the air- and CO_2 sparging in the base compartments (acid compartment were not sparged). The input is feed, which is synthetic seawater, applied current density, gas pressure and sparging interval. The output refers to measured parameters during the experiment which are logged and saved every second.

In addition, a gas sparging experiment for air and CO_2 (g) was done for a membrane stack without spacers, to investigate the influence of spacers on gas sparging performance.

3.2.5. Increasing the flowrate in the base channels

Inorganic fouling removal via flowrate-increase was tested by increasing the flowrate of the base compartments every 10 minute (by using the option pf "prime" for the pumps), which

started 5 minutes after the experiment started. The flowrate was increased by 5 times (i.e., 360 mL·min^{-1} per compartment or 15 cm·s^{-1} or τ_r= 0.67 seconds) and 15 times (i.e., 1080 mL·min^{-1} per compartment or 45 cm·s^{-1} or τ_r = 0.22 seconds) the operating flowrate (72 mL·min^{-1} per compartment).

3.2.6. Back pressure

Backpressure was applied by temporary closing the valve located at the outlet of the base channel while leaving the feed pumps on, causing pressure to build up in the base compartments. The pressure build up was measured at the base outlet using an analog pressure gauge, the build-up pressure was between 2-3 bar. By reopening the valve, this pressure is released suddenly, pushing inorganic fouling out of the cell. This was done for the base compartments every 10 minute, which started 5 minutes after the experiment started.

3.2.7. Acid wash

In addition to the CEM-BPM configuration, acid wash was also done for the AEM-BPM configuration. For the CEM-BPM configuration, acid wash was done at 200 mL·min^{-1} per compartment with hydrochloric acid. Recovery was measured as voltage and pressure drop recovery.

For the acid wash experiments on the AEM-BPM configuration, some adjustments were made to improve the feasibility of acid wash. Acid wash was tested by using pure hydrochloric acid (HCl) with a pH in the range of 1.5-2.0, as well as the produced acid from the BPMED cell with a pH in a higher range of 2.4-2.6. Before cleaning the BPMED cell was ‘scaled’, with a current density of 12.5 mA·cm^{-2}, a flowrate of 72 mL·min^{-1} per compartment for 60 minutes. For both types of acid, the experiments were done using 72 and 144 mL·min^{-1} per compartment (i.e., 3 and 6 cm·s^{-1}). Backpressure on the base channels was applied to ensure the channels were filled with acid and to disrupt possible formed inorganic fouling channels. The current was turned off during the acid wash. The cleaning was done until the pressure drop of the base channel did no longer decrease. The efficiency of the cleaning method was measured by the used H^+ ions in moles, the pressure drop recovery and the cleaning time. Also, an experiment was done where the base compartments of the cell was soaked in HCl for 5 minutes (i.e., flow rate was 0). The base compartments were filled with acid until the base outlet pH was within 0.2 of the acid pH of 1.5. Then, the pumps were turned of and the soaking time started.

4. Results and discussion

The average ion concentrations, conductivity and pH values for the synthetic seawater used in the experiments are shown in *Appendix VI – Average values synthetic seawater*. First, the results for the fouling control experiments are discussed, then the results for the fouling removal experiments. Also, an outlook on what the results mean for the technology. pH, DIC removal, Ca^{2+} and Mg^{2+} ions removal was simulated in Visual MINTEQ 3.1 and compared with measured values throughout the chapter.

4.1. Inorganic fouling control

First, the stack voltage increase-time curves and the increase in the stack-ohmic resistance (Figure 9) were compared.

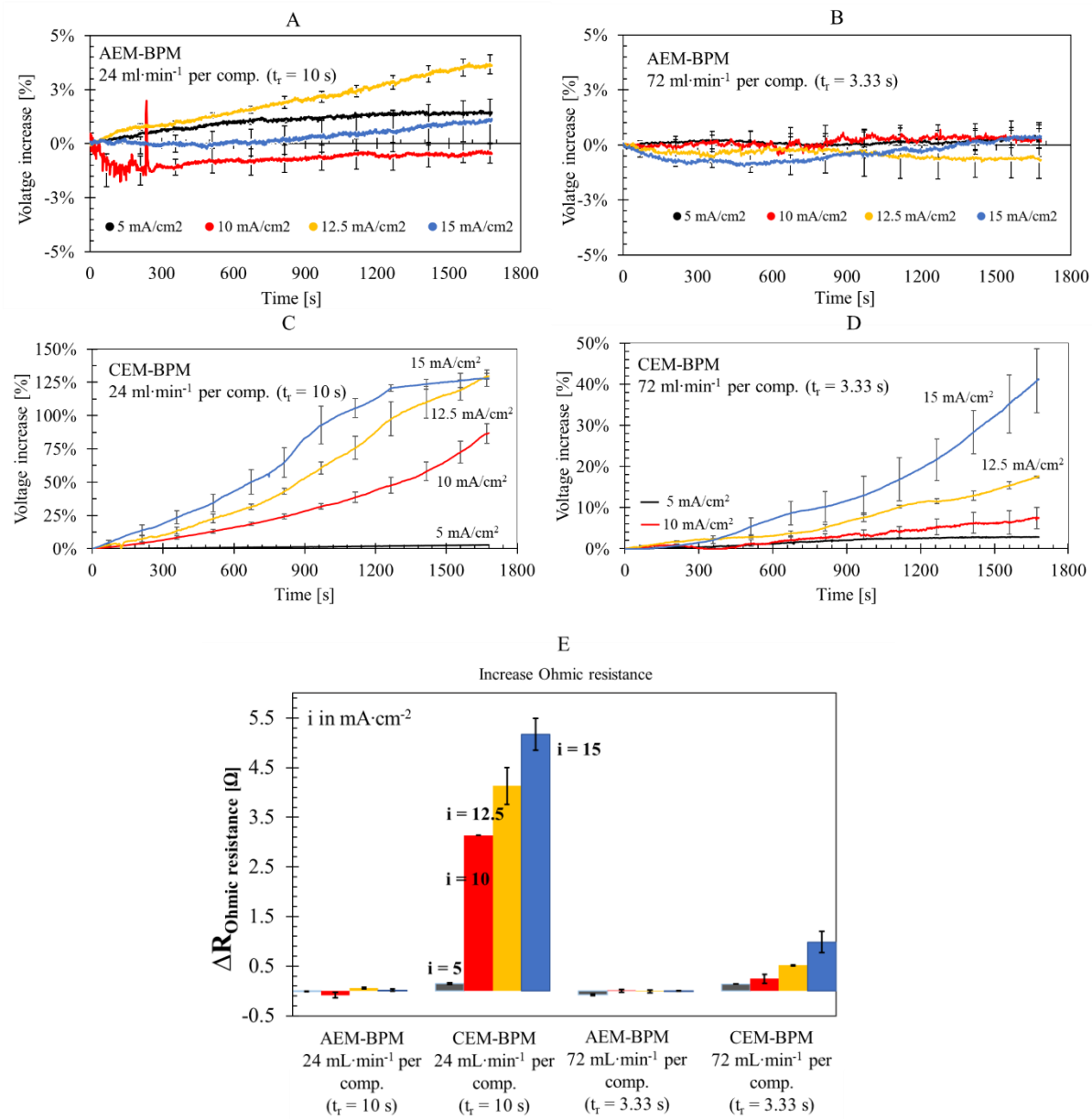

Figure 9, (A) shows the voltage increase [%] for the AEM-BPM configuration for the 24 mL·min^{-1} per compartment and (B) for the 72 mL·min^{-1} per compartment. (C) Shows voltage increase [%] for the CEM-BPM configuration for 24 mL·min^{-1} per compartment and (D) for 72 mL·min^{-1} per compartment. For A-D, the curves show the average of two repetitions with the error bars showing the standard error values between the two repetitions. The flowrate and applied current density were kept constant during the experiments, the voltage increase is relative to the voltage at t=120 seconds. (E) shows the difference in Ohmic resistance before and after the experiments for all 16 experiments as an average of 2 repetitions (standard error included with error bars, when error bars are not visible, they are smaller than the line width).

The voltage-increase for the AEM-BPM cell-pair configuration stays within +/-5% of the starting voltage for each flowrate and applied current density (Figure 9A-B). For the AEM-BPM configuration with 10 seconds cell residence time (τ_r) (i.e., 24 mL·min^{-1} per compartments) (Figure 9A) there is a small increasing trend for 12.5 mA·cm^{-2} (0.002% per second) and 15 mA·cm^{-2} (0.0006% per second) indicating some inorganic fouling build-up (for 15 mA·cm^{-2} the increase is within the standard error range). During one of two experiments applying 10 mA·cm^{-2} the electrolyte rinsing solution was not recirculating for the first 600 seconds, causing noise in the voltage measurement. For τ_r = 3.33 seconds (i.e., 72 mL·min^{-1} per compartment) (Figure 9b) for 15 mA·cm^{-2} a small increases were measured, the voltage curve initially decreases because for one of the two experiments the voltage stabilized only after ~200 seconds, for unknown reasons. For the other 3 applied current density voltage increase does not show an increasing trend. Based on the voltage-time curves for the AEM-BPM configurations, it was concluded that mostly none (and in some cases small) inorganic fouling had build-up.

On the contrary, the CEM-BPM cell-pair configuration does show a steep increase of voltage over time. A higher applied current density resulted in a higher percentual voltage increase (Figure 9C-D). Also, τ_r= 10 seconds results in higher percentual voltage increase than a for τ_r= 3.33 seconds for the CEM-BPM configuration (for 15 mA·cm^{-2} and τ_r= 10 seconds the maximum voltage of the potentiostat was reached at ~1300 seconds). There was an exception for an applied current of 5 mA·cm^{-2}, for which the voltage increases less than 5% for both cell residence times. It appears that under applied current density of 5 mA·cm^{-2}, created circumstances result in little inorganic fouling in the cell. The exact reason is not known, absence of local pH extremes or kinetics are possible causes. However in literature, lower fouling dosage in a reverse electrodialysis (RED) system (with an AEM-CEM configuration) resulted in minor ohmic resistance and only increased significantly after doubling the dose (Pintossi et al., 2019). Since this RED system had a (fairly) constant pH, it indicates that increase in ohmic resistance only becomes significant from a certain lower limit of fouling.

More inorganic fouling build-up for a longer cell residence time and higher applied current density was expected. Considering that the base-pH increases with applied current density (Equation 11 substituted into Equation 12) and the increase of the saturation index with base-pH (Equation 7), this pattern was expected. The relation between applied current density, cell residence time and OH^- ions production is shown in Figure 15E. In addition to the chemical explanation that a longer cell residence time results in more fouling, there also is a physical component. A higher flow velocity enhances mixing is the compartments, which decreases high local pH near the membrane's surfaces (Vermaas et al., 2014b). Higher velocity also increases the wall shear stress in the compartment, reduces the opportunity for mineral precipitates to deposit (Equation 18).

Comparing AEM-CEM vs. CEM-BPM, the voltage-increase curve indicates a more extensive inorganic fouling build-up for the CEM-BPM configuration (Figure 9A-D). The measured increase in Ohmic resistance (Figure 9E) validates this observation. For the AEM-BPM configuration, increase in Ohmic resistance was (within the error margin) around zero, for all the applied current density and cell residence time combinations. For the CEM-BPM configuration, Ohmic resistance increased substantially, with the same pattern as described for the voltage increase. Such pattern was expected as the increase in Ohmic resistance is determined from the voltage-time curve (calculations are shown in *Appendix I – Determination of Ohmic resistance).* As Ohmic resistance is the sum of membrane resistance and electrolyte conductivity between the compartments (Vermaas et al., 2014c), the ohmic resistance increase is likely the result of increased membrane resistance as the electrolyte is similar for the CEM-BPM and AEM-BPM configurations. This indicates that for the CEM-BPM configuration inorganic fouling builds up on membranes surfaces and not on the AEM-BPM configuration. However, it should be remembered the total stack voltage gives information about the overall behaviour of the cell and it can not be known for certain where in the system inorganic fouling occurs (Pintossi et al., 2019).

The reason the CEM-BPM configuration suffers more inorganic fouling than the AEM-BPM configuration can be explained looking at the difference between having an CEM vs. AEM membrane in the cell pair (Figure 10). In the CEM-BPM configuration, in addition to Na^+ that is the main charge carrier, there is Ca^{2+} and Mg^{2+} ions transport through the CEM toward the base compartments due to the migration force (Figure 10B). This causes high concentrations of these cations just near the CEM surface in the base compartment (i.e., concentration polarization), increasing the saturation index (Equation 7) and thus promoting faster mineral

precipitation. OH^- and CO_3^{2-} ions are pulled towards the CEM due to the direction of the electric field. Considering it was reported that the perm selectivity of CEMs is affected under base conditions (especially OH^- ion transfer was reported), circumstances are created at which inorganic fouling can deposit on or even inside the CEM (Casademont et al., 2008a). precipitation between OH^- ions passing though the CEM and divalent cations in the concentration polarization layer of the CEM were reported (Casademont et al., 2008a), (Wang et al., 2011) even found minerals containing OH^- and Mg^{2+}/Ca^{2+} ions inside the CEM as well as the surface. For the AEM-BPM configuration, Mg^{2+} and Ca^{2+} ions are pulled towards the AEM but should not be able to transport through (Figure 10A). Mg^{2+} and Ca^{2+} ions may accumulate near the AEM surface in the acid compartments, but acid-pH is too low for mineral crystallization (pH ~2.5). Furthermore, the $CO_3^{2-}$and OH^- ions can transfer over the AEM, but considering that their concentrations are low compared to the Cl^- ions (0.0023 M HCO_3^-/CO_3^{2-} and 0.000063 M OH^- for pH 9.8 vs. ~ 0.55 M Cl^-), anion transport through the AEM through migration will be predominantly Cl^- ion according to the Nernst-Planck (Equation 10). Therefore, it is considered unlikely than $CO_3^{2-}$and OH^- ions accumulate near the AEM surface in the base compartment.

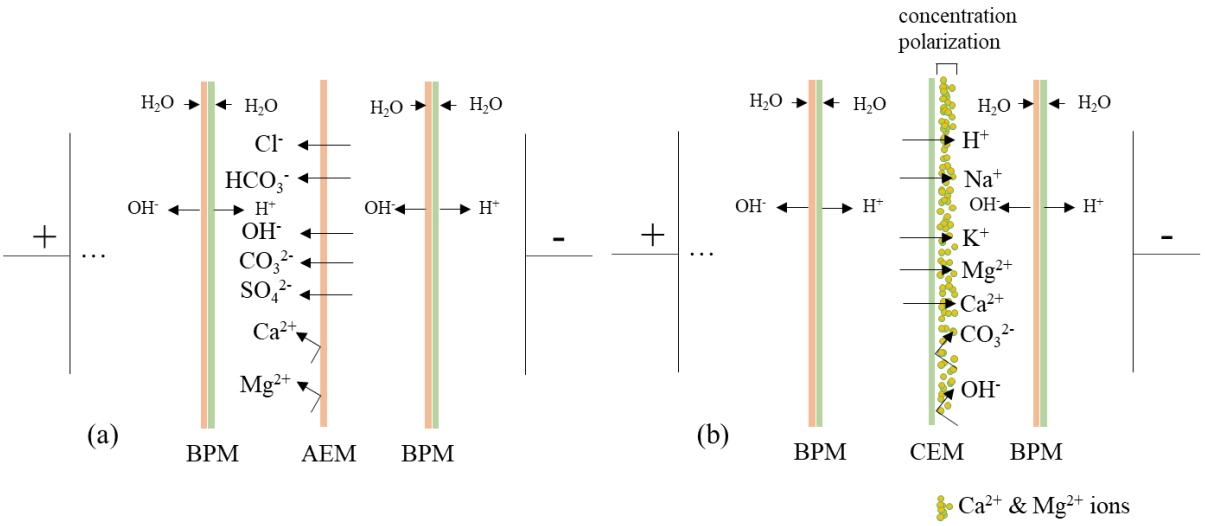

Figure 10, Ion cross over in (a) an AEM-BPM cell pair configuration, and (b) CEM-BPM cell pair configuration, accumulation of Ca^{2+} and Mg^{2+} ions is illustrated.

Theoretically, the total stack voltage is equal for both configurations. However, the CEM-BPM configuration always showed a higher total initial stack voltage (initial means measured before the experiments) than the AEM-BPM configuration, for the same applied current density (Figure 11).

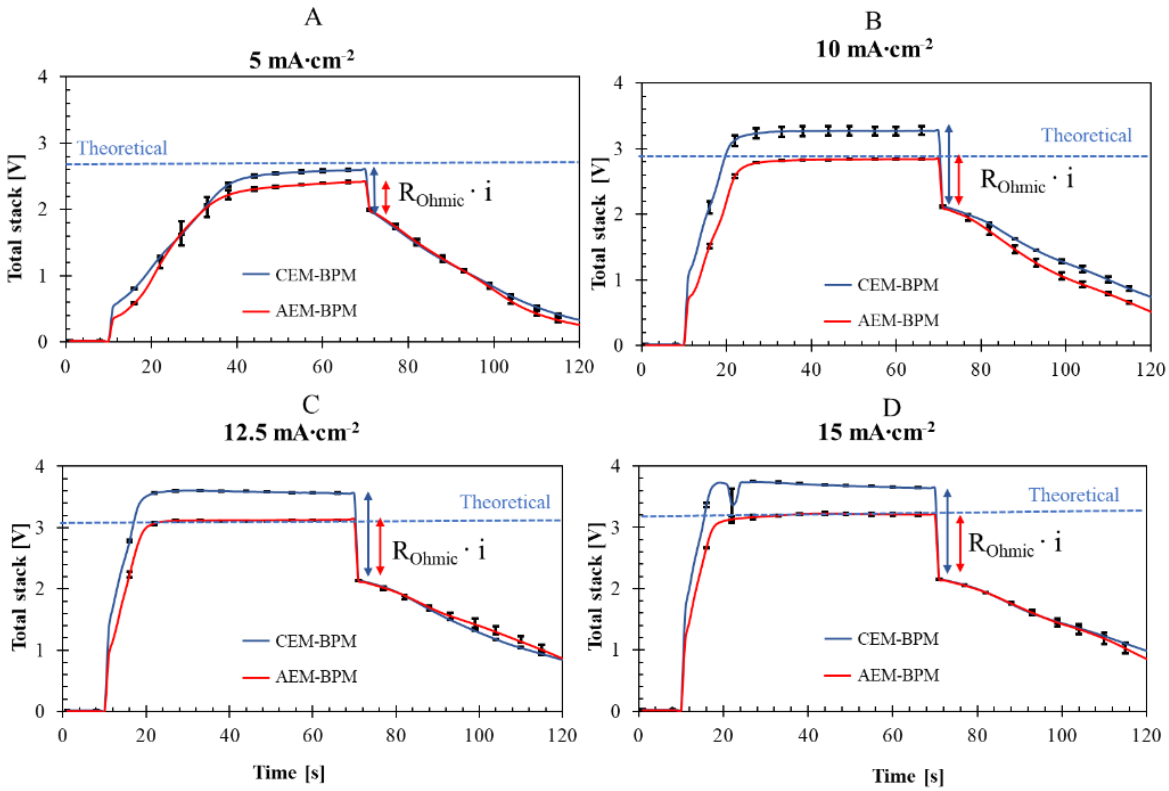

Figure 11, Difference of the initial total cell voltage comparing the AEM-BPM configuration and the CEM-BPM configuration, before the experiments (so cleaned membranes). These V-t graphs are for 72 mA·cm^{-2} per compartment and the average voltage curve of 2 repetitions incl. the standard error between the repetition (when error bars are not visible, they are smaller than the line width). Graphs are shown for current densities of 5 (A), 10 (B), 12.5 (B) and 15 (D) mA·cm^{-2}. Theoretical total cell voltage was calculated based on membrane resistance, electrolyte conductivity, voltage for water dissociation. The calculations are shown in *Appendix X – Energy consumption.*

Before the experiments started, the current was turned on for 60 seconds, then turned of for 60 seconds and than the experiments started (a full cycle is shown in *Appendix I – Determination of Ohmic resistance*), these first 120 seconds are shown in Figure 11. This was done to measure the total stack voltage and reveal the ohmic resistance before the experiments. The voltage fraction defining the Ohmic resistance is larger for the CEM-BPM than for AEM-BPM configuration, were the non-Ohmic fraction is comparable. Considering that Figure 11 shows the total stack voltage before the start of the experiments (so the membranes are not fouled yet) and the conductivity of the electrolyte was similar for all experiments, this must be caused by difference in the membrane resistances. According to the FuMATech B.V. supplier the membrane resistance should be comparable for the AEM and CEM (i.e., 4 Ω·cm^2). However, as the membrane age, their resistance become larger (Ghalloussi et al., 2013). The CEM membranes were in use for several months, were the AEM membranes were new when these experiments were done, justifying the higher initial resistance of the CEM-BPM configuration. Another factor that can contribute to this difference is initial stack voltage is the internal fouling

inside of the CEM, which could not be cleaned by any acid wash. While the CEM membranes were in use, conditions (i.e., current density-flowrate) were used were there was pushed for inorganic fouling. Initially, inorganic fouling on the CEM could be washed of during acid cleanings (Figure 12A). It was noticed after several weeks that inorganic fouling also appeared inside the membrane, which could not be removed by any acid wash. Membranes were put in 1M HCl for >48 hours, yet the inorganic fouling could not be washed out (Figure 12B). Therefore, the CEM membranes already had some inorganic fouling inside, increasing the membrane resistance. However, it is not known to what extent the higher stack voltage was caused by this inorganic fouling or by the membrane's resistance increase due to its ageing.

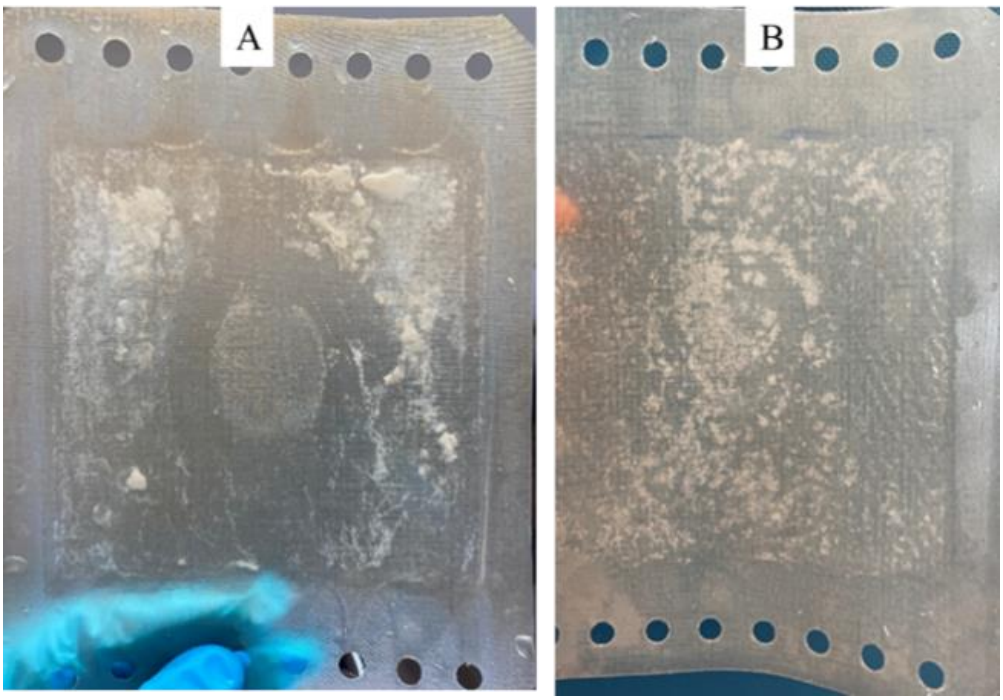

Figure 12, inorganic fouling on cation exchange membranes (CEM). (A) shows mostly reversible inorganic fouling (picture from 19-04-2021) ((B) shows irreversible inorganic fouling. (B) is a picture of the CEM after cleaning with acid showing the irreversible internal fouling inside of the membrane (picture from 2 months later than a on 03-06-2021).

The second parameter measured to detect inorganic fouling was the pressure drops (ΔP in mbar) over the base compartments at constant flowrate and applied current density, which increases by inorganic fouling build-up (Figure 13).

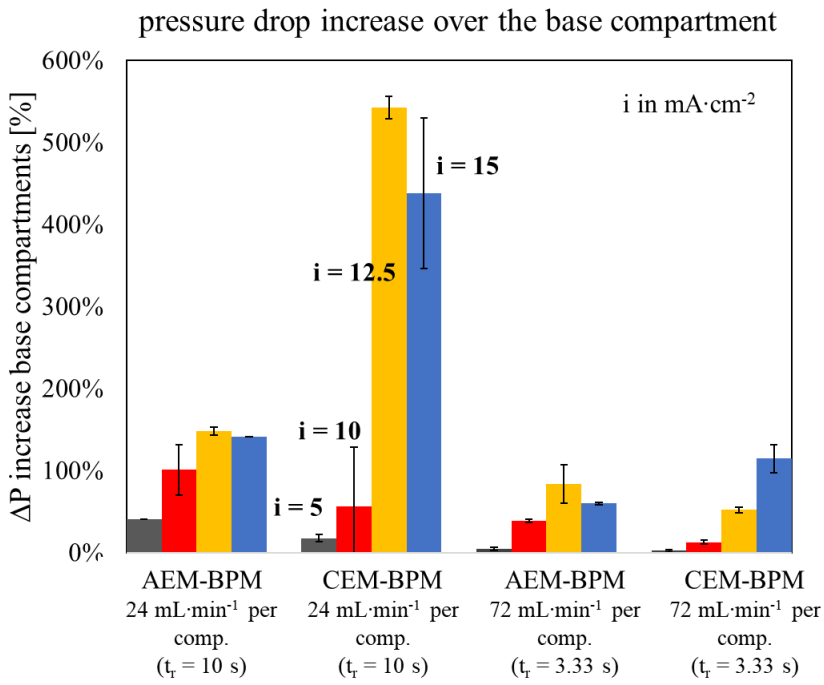

Figure 13, The total increase [%] of pressure drop between the inlet and outlet of the stack on the base-compartments after all 30-minute experiments is shown in as a bar graph as the average of two repetitions including the standard errors as error bars. Percentual pressure drop increase is shown in *Appendix VIII – Pressure drop increase base channel (%)*.

A cell residence time (τ_r) of 10 seconds showed a higher increase of pressure drop than for τ_r = 3.33 seconds, comparing the same applied current density. This was the case for both cell pair configurations. More inorganic fouling build-up for a longer cell residence time was expected, for the same reasons as stated for the voltage increase (higher local pH and less mixing the compartment for τ_r = 10 seconds).

For τ_r= 10 seconds, the AEM-BPM and CEM-BPM configurations are in each others standard error range for 5 and 10 mA·cm^{-2}. For 12.5 and 15 mA·cm^{-2} the CEM-BPM configuration shows a much higher pressure drop increase, indicating severe inorganic fouling (as was already indicate by Figure 9E). For τ_r = 3.33 seconds both configuration show a similar pressure drop increase (also considering the error bars).

When comparing AEM-BPM vs. CEM-BPM, the results for increase in Ohmic resistance and pressure drop tell a different story. Figure 9 indicated no inorganic fouling for the AEM-BPM configuration and (in some case severe) inorganic fouling for the CEM-BPM configuration. However, the pressure drop increase indicated inorganic fouling for both cell pair configurations. As it was hypothesized that Ohmic resistance increases due to increase in membrane resistance, and pressure drop is influenced by multiple factors (e.g., channel formation), inorganic fouling might deposit on different places in the compartments (e.g.,

mostly on the spacers for the AEM-BPM configuration but on the CEM and the spacers for the CEM-BPM configuration). Again, just as for total stack voltage, pressure drop cannot confirm where in the system inorganic fouling occurs.

In general, one can expect a general increasing pattern between the applied current density and increase in pressure drop which is shown in Figure 13. However, for i = 12.5 mA·cm^{-2} the pressure drop increased more than for i = 15 mA·cm^{-2}. That the pressure drop increase does not always follow the pattern of the applied current density, is because the pressure drop is not only influenced by the inorganic fouling but also how it deposits (i.e., channel formation) in the compartment and spacers (Figure 14).

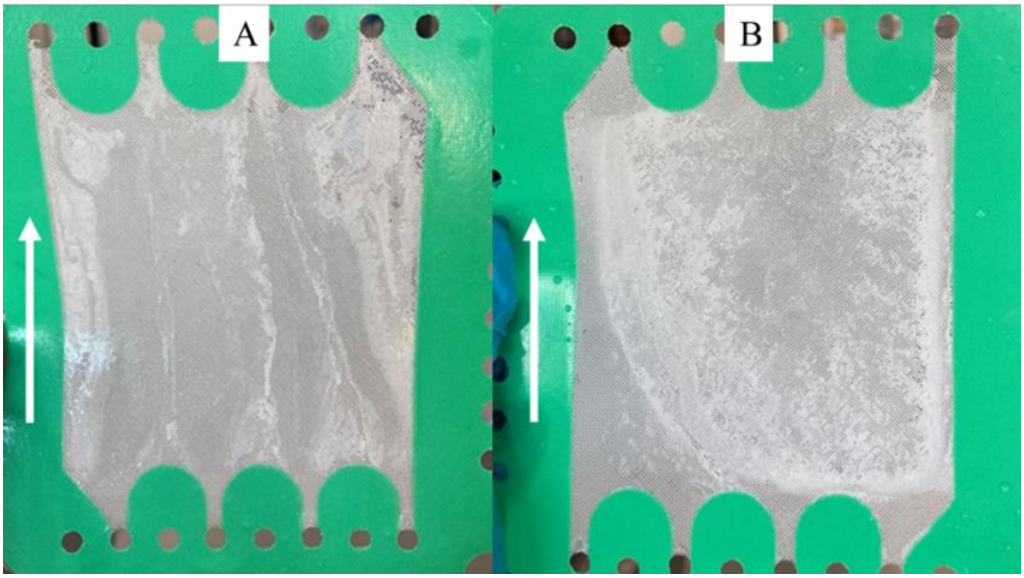

Figure 14, Channel formation in inorganic fouling on spacers. The white arrow shows the flow direction. (A) was taken on 06-10-2021 (B) was taken on 09-07-2021. Both pictures were after an experiment with 3 cm·s^{-1} flow and 12.5 mA·cm^{-2} applied current using a CEM-BPM configuration.

As can be observed from Figure 14 channel formation on spacers decreases the flow area, since the feed will flow primarily through the channels. Since the flowrate is kept at a constant, the flow velocity must increase by the decrease in the flow area. As pressure drop increases with increased flow velocity (substituting Equation 18 in Equation 19), channel formation can increase the pressure drop. Whether or not channels are formed and what flow path they have is highly unpredictable. Figure 14A show channels with 4 spacer inlets and 2 outlets, were Figure 14B show 3 spacer inlets and one outlet, which influence the flow velocity (and therefore pressure drop) differently.

Another consequence of channel formation is that no uniform flow velocity throughout the whole compartment can be guaranteed. For a reverse electrodialysis (RED) system this

nonuniform distribution of feedwater, induced nonohmic resistance increase due to depletion of ions in zones were the velocity was lower (Vermaas et al., 2014c). In this case, the reverse effect could be triggered by channel formation: in zones with low velocity OH^- ions concentrations can increase causing local extreme pH. High pH values enhance hydroxide containing minerals precipitation (Figure 3). Also, when minerals have already precipitated, the energy barrier for Ca^{2+}, Mg^{2+}, CO_3^{2-} or OH^- ions (depending on the already formed nuclei) to precipitate onto those is lower (i.e., growth of the precipitates) (Mercer et al., 2005). Therefore, these channels can speed up inorganic fouling on the spacers.

The pH was measured in the outflow of the acid and the base compartments (outside the cell). Those measurements together with the expected simulated-pH values are shown in Figure 15.

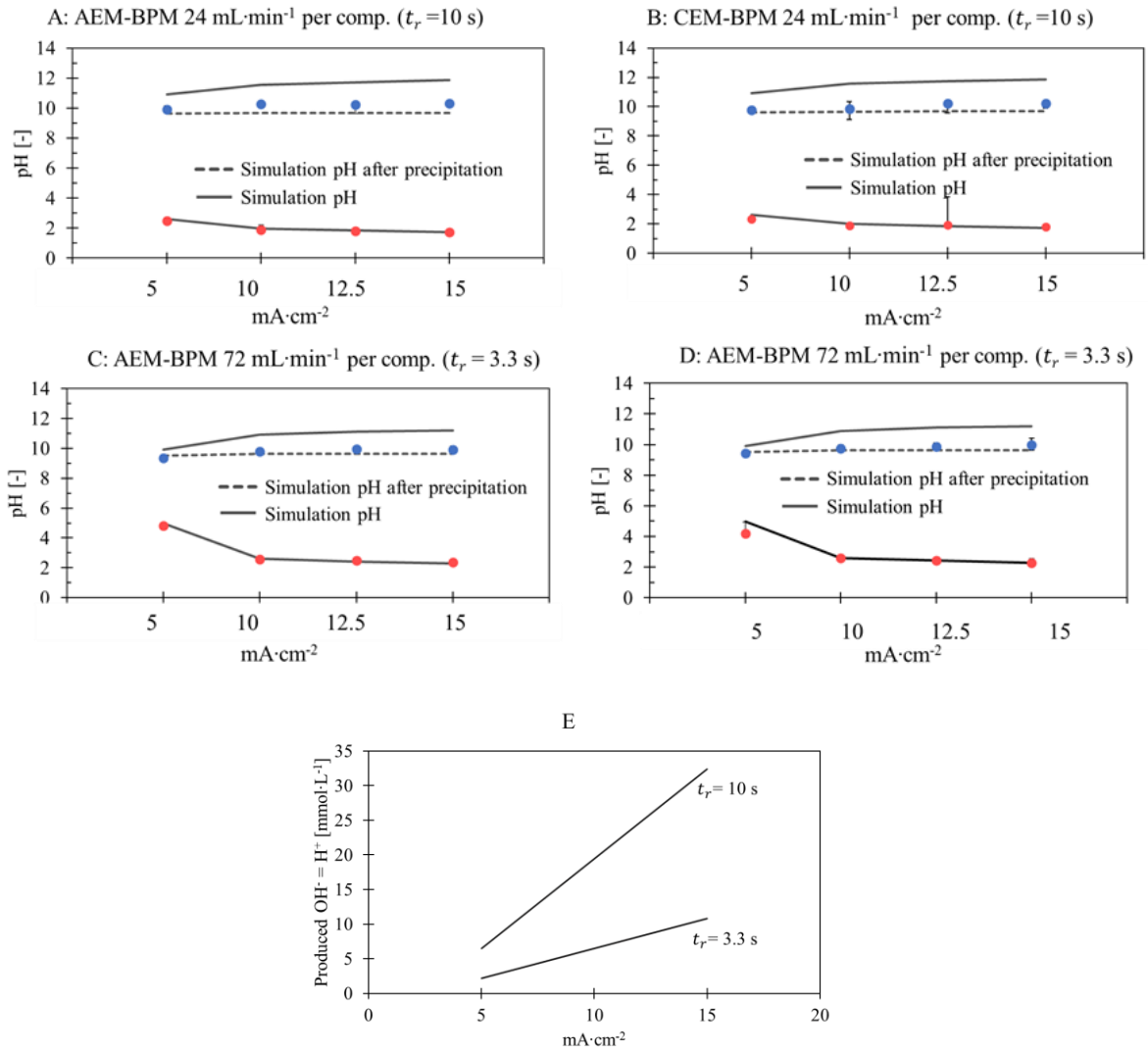

Figure 15, A-D: Bulk pH of the outlet of the acid (red) and base (blue) compartments vs., Cell residence times (t_r) and applied current densities. The pH values according to the Visual MINTEQ 3.1 simulations are shown with the grey line, pH values after precipitation are shown with the dotted grey lines. E: The simulated pH was based on the produced OH^- and H^+ for an applied current density, and the concentration made depended on the cell residence time. The measured pH values are the

average of 2 repetitions, with pH-measurements starting 5 minutes seconds after the current was turned on to ensure full water dissociation. The whole range in which values were measured with the error bars, however most bars are not visible under the markers as the values are small (all values can be found in *Appendix IX – pH and DIC, Ca2+, Mg2+ removal*).

For both cell pair configurations, cell residence times and all applied current densities the measured pH value for acid outlet is about the same as the values from the simulated pH. This indicates that the fluxes over the BPM and its effect on the concentrations in the acid compartment conforms to Equation 11 and Equation 12 from theory. For the base pH, both the outlet pH and the pH after mineral precipitation were simulated, as the base-pH decreases upon mineral precipitation (since an OH^- converts to H_2O when reacting with an H^+ ion of $HCO3^-$ (Stumm & Morgan, 1995)). Because mineral precipitation takes place inside the base compartments, it was expected that the measured pH in the base outlet is between the simulated pH before- and after precipitation. Considering the pH meters error of +/- 0.2 pH-units, the AEM-BPM and CEM-BPM configuration have comparable pH values for the same cell residence time and applied current density.

To compare the two cell-design performances, the $CaCO_3$ precipitation is measured as DIC removal [mM] which is compared to the Ca^{2+} ion removal [mM] (Figure 16).

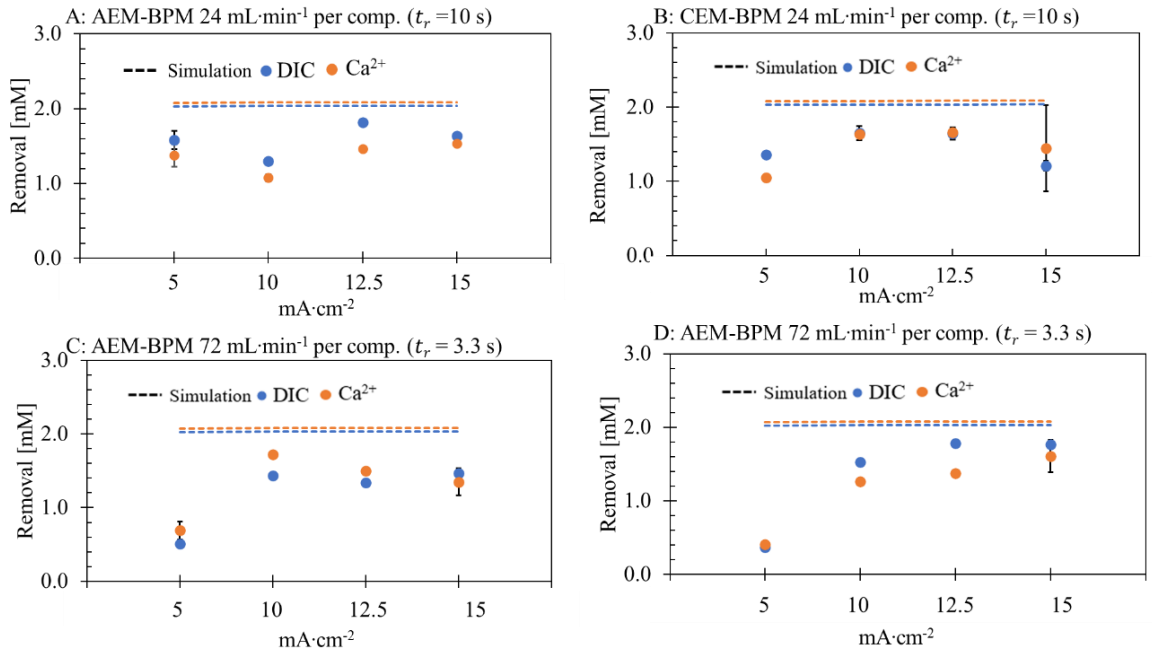

Figure 16, A-D: DIC and Ca^{2+} ion removal for both cell pair configurations, cell residence times (t_r) and applied current densities. The removal according to the Visual MINTEQ 3.1 simulations are shown with the dotted line. The concentrations in the feed were ~2.1-2.4 mM and 10 mM for DIC and Ca^{2+} ion, respectively. The DIC and Ca^{2+} ion removal values are the average of 2 repetitions, and the standard error is included, however most bars are not visible under the markers as the values are small (all values can be found in *Appendix IX – pH and DIC, Ca^{2+}, Mg^{2+} removal*).

According to the simulations, there is no difference in DIC and Ca^{2+} ion removal for the different cell residence times or applied current density, since the pH should be sufficient (> 9.5) for mineral precipitation of $CaCO_3$ for all these circumstances (Figure 15). The DIC removal will never reach 100%, as the solubility of CO_3^{2-} is 0.044 mmol·kg^{-1} seawater (based on [Ca^{2+}] = 9.96 mmol·kg^{-1} sea water and K_{sp} for $CaCO_3$ is $4.39 \cdot 10^{-4}$ mmol·kg^{-1} sea water) (Zhong & Mucci, 1993). When there is sufficient time for precipitation (>72h), DIC removal is not expected to be influenced by cell residence time during the experiments (if pH > 9.5). However, maximum DIC removal was never reached during the experiments. Simulation only considers thermodynamics, explaining why DIC removal during experiments is lower, since in reality kinetics also influences the precipitation. Alternatively, the reason can be that the DIC removal is possibly underestimated due to the inaccuracy of the titration method (*Appendix II – Titration for DIC Concentration Approximation*). During titration the decarbonated base sample is in contact with air, enabling CO_2 (g) from the air to be absorbed into the sample, underestimating the actual DIC removal. For the AEM-BPM configuration CO_3^{2-} ions transfer to the acid compartments is possible (Figure 10A) but transfer will be low as Cl^- is the main charge carrier due to its higher concentration (as explained above Figure 10).

Also, for most experiments the DIC removal is higher than the Ca^{2+} ion removal (except for AEM-BPM 3.33 seconds cell retention time 5-12.5 mA·cm^{-2}). Since the molar ratio of calcium and carbonate is 1:1, also this indicates also other carbonate containing minerals precipitate.

A combination of 5 mA·cm^{-2} and τ_r= 3.33 seconds resulted in the lowest DIC and Ca^{2+} ion removal (Figure 16C-D). Apart from the just mentioned exception, there is no difference in DIC removal when comparing cell residence time.

Comparing the cell pair configurations, the DIC removal τ_r = 3.33 seconds is slightly higher for the CEM-BPM than for AEM-BPM configuration. For experiments of 1 hour, it was found that DIC removal for the AEM-BPM configuration was comparable with the CEM-BPM configuration for τ_r= 3.33 seconds and applied current density of 12.5 mA·cm^{-2}. This could be because the CEM-BPM configuration will have higher concentration of Mg^{2+} and Ca^{2+} ions in the base compartments (due to transfer over the CEM (Figure 10)). Consequentially the SI values for the CEM-BPM configuration will be slightly higher (Equation 7). Considering the kinetics for $CaCO_3$ are the time limiting factor in the conversion of HCO_3^- to $CaCO_3$ (La Plante et al., 2021), an earlier start of precipitation might cause a measurable difference during 30-minute experiments but not 1-hour experiments.

Mg^{2+} ion removal is higher for τ_r=10 than for τ_r = 3.33 *Appendix IX – pH and DIC, Ca2+, Mg2+ removal)*. For a higher residence time the base pH is higher, considering the high SI value for $Mg(OH)_2$ increases fast when pH >10 (Figure *3*) more Mg^{2+} ion removal is expected for a longer cell residence time.

The effect of the applied current density, cell residence time and cell pair configuration on inorganic fouling build-up and DIC removal all comes together when looking at the energy consumption for extraction of $CaCO_3$ (Figure *17*).

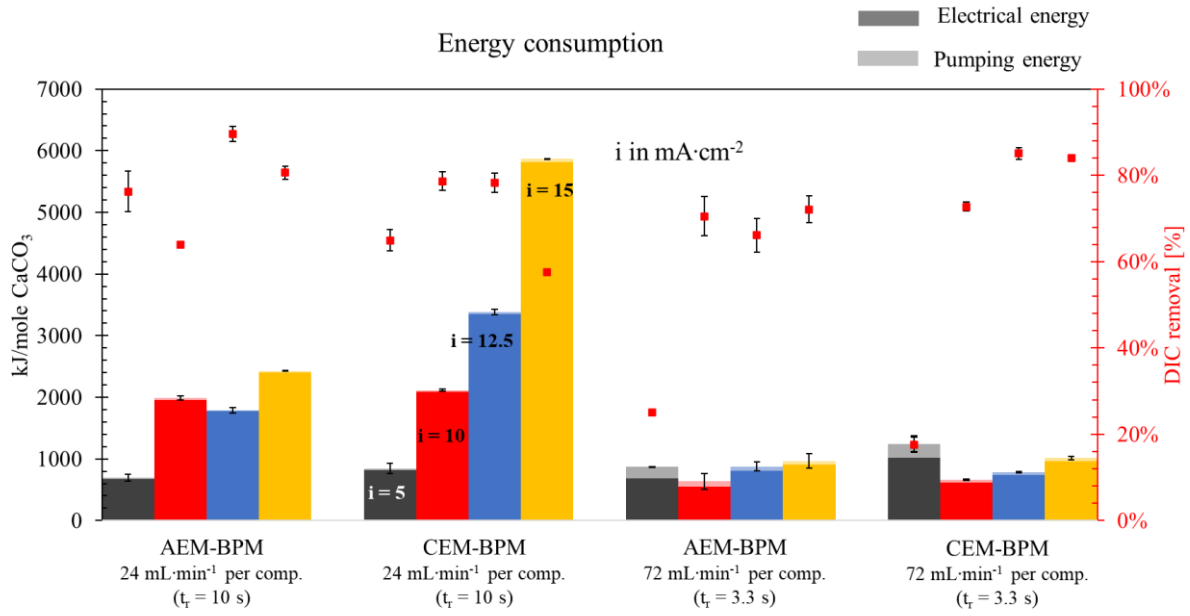

Figure 17, Energy consumption (kJ/mole $CaCO_3$) for the AEM-BPM and CEM-BPM configuration and a cell residence time of 10 seconds and 3.33 seconds for an applied current density of 5, 10, 12.5 and 15 mA·cm^{-2} (from left to right). Distinction was made between electrical energy (dark colour) and pumping energy (light colour). The right y-axis shows the DIC removal (%) The bars are an average of 2 repetitions and the standard error is included via the error bars. Calculations are shown in Appendix X – Energy consumption.

Energy consumption can be divided into electrical- and pumping energy consumption (Equation 17). For the CEM-BPM configuration, the electrical energy consumption increases over time, since the total stack voltage increases (Figure 9C-D). Pumping energy increases for both configurations, due to the increase of the pressure (Figure 13). The pumping energy is a relatively small fraction of the total energy consumption (pumping energy is not even visible for most bars representing an experiment with τ_r= 10 seconds).

For the CEM-BPM configuration the energy consumption increases as the applied current density increases. For AEM-BPM this pattern is disrupted by a low DIC removal (and therefore

high energy consumption) for τ_r= 10 seconds in combination with 10 mA·cm^{-2} and for τ_r = 3.33 seconds in combination with 5 mA·cm^{-2}.

The lowest energy consumption (637 kJ/mole $CaCO_3$) was achieved for the AEM-BPM configuration under an applied current density of 10 mA·cm^{-2} and τ_r= 3.33 seconds (i.e., flowrate of 72 mL·min^{-1} per compartment). This value is lower/comparable with values found in literature 634-1276 kJ/mole $CaCO_3$ (de Lannoy et al., 2018), 1080–2880 kJ/mole $CaCO_3$ (Zhao et al., 2020), 390-640 kJ/mole $CaCO_3$ (Youn et al., 2019). The lowest value in literature (330 kJ/mole $CaCO_3$ (Boer, 2020)) was in the overarching project of this thesis. However, in this research, the aim was not to optimize energy consumption.

The DIC removal was generally found to be between 65-85%, but since a flowrate of 72 mL·min^{-1} per compartment generates a higher $CaCO_3$ production rate ($6.17 \cdot 10^{-6}$ – $8.07 \cdot 10^{-6}$ kg·hr^{-1} per m^2) than 24 mL·min^{-1} per compartment ($2.06 \cdot 10^{-6}$ – $2.69 \cdot 10^{-6}$ kg·hr^{-1} per m^2), the energy consumption is lower for the higher flow rate. For τ_r= 3.33 seconds and applied current density of 12.5 and 15 mA·cm^{-2}, the DIC removal for the CEM-BPM configuration is higher than for the AEM-BPM configuration. Therefore, the energy consumption is comparable even though the CEM-BPM configuration has a higher build up of Ohmic resistance.

Considering the increase of Ohmic resistance for the CEM-BPM configuration, which was not measured for the AEM-BPM configuration (Figure 9E) and the dominant part of electrical energy consumption in the total energy consumption , it is expected that the difference in energy consumption increases as time increase (in favour of the AEM-BPM configuration). Combining this advantage with the observation that DIC removal for longer experiments were comparable for the AEM-BPM and CEM-BPM configuration, the AEM-BPM configuration would have preference over CEM-BPM for the application of oceanic carbon capture.

4.2. Inorganic fouling removal

As explained in the materials and method section (*3.2.3 Inorganic fouling removal*), all experiments in the inorganic fouling removal section were conducted under accelerated inorganic fouling condition to account for the worst-case scenario; experiments with durations of ≥ 1 hour with 12.5 mA·cm^{-2} applied current density and a flowrate of 72 mL·min^{-1} per compartment (i.e., τ_r = 3.33 seconds), that were kept constant. The gas sparging, flow rate increase, back pressure and acid wash methods have been done for the BPM-CEM stack as it demonstrated much higher inorganic fouling build up compared to the AEM-BPM configurations, aligning well with the “worst case scenario”. In general, for both stacks, a lower

current density (i.e., 5 $mA \cdot cm^{-2}$), lowers the fouling rate substantially, but is not chosen in alignment with the thesis goal: inorganic fouling study.

The method with the most promising result from the experiments done on the BPM-CEM stack, was also tested for the AEM-BPM configuration (which was acid wash), to investigate if this would improve the feasibility of the inorganic fouling removal method.

4.2.1. Gas sparging

Gas sparging was done with both air and CO_2 (g) for the BPM-CEM configuration, results for both gasses are shown, including the effect of spacers on the efficiency of inorganic fouling removal via sparging.

4.2.1.1. Air sparging

Air sparging as a physical inorganic fouling removal method was tested for a pressure range of 1-4 bar. Efficiency of the inorganic fouling removal was determined though the voltage and pressure drop curve, results for experiments done with 2 and 4 bar are shown in Figure 18.

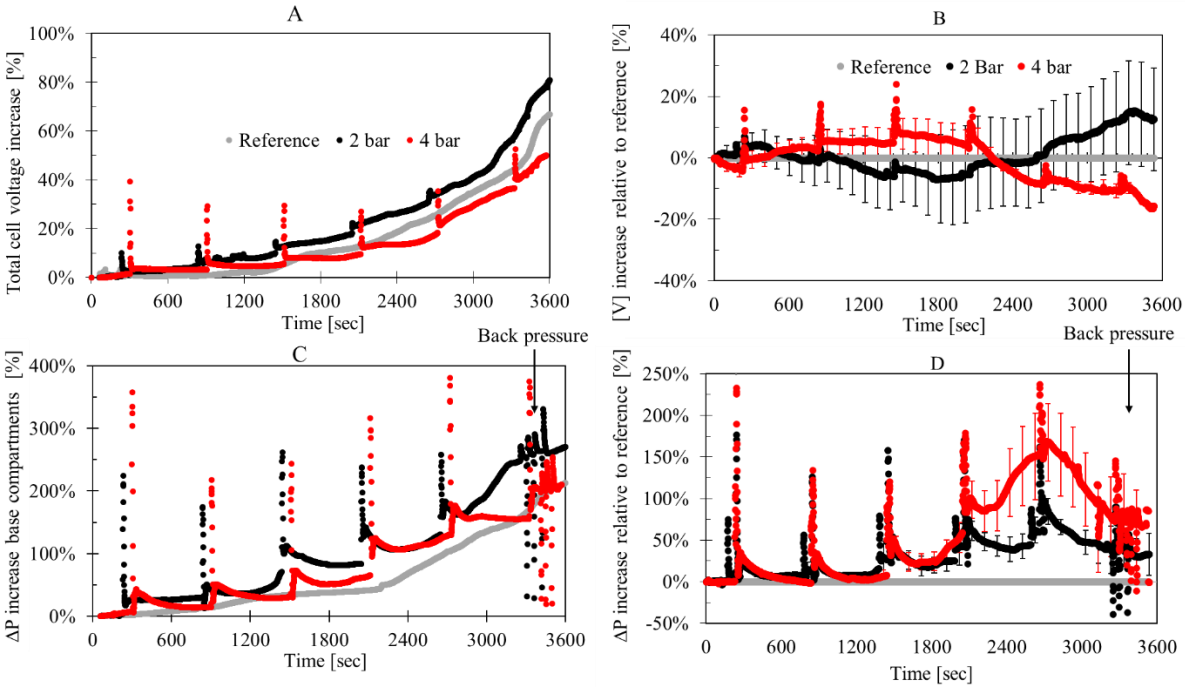

Figure 18, Air sparging under 2 and 4 bar, every 10 minutes for 5 seconds. Comparison of (A) voltage increase (%) and (C) pressure drop increase (%) with a reference experiment (with no sparging or other cleaning methods) are shown (for 1 repetition). Furthermore, the development of (B) the voltage increase (%) and (D) pressure drop increase (%) relative to the reference experiment is shown, the lines are average of 3 repetitions including the standard error as error bars, for 2 of the 3 experiments with 2 bar pressure back pressure was applied to release stagnant bubbles. How the figure was made from raw data is shown in (*Appendix XI - Pressure drop and voltage increase (%) relative to the reference experiment*).

In Figure 18, sparging causes peaks in the graph as the voltage and pressure drop show a temporary peak. The peaks for 4 bar are higher than for 2 bar. When looking at the curves for voltage increase (Figure *18*A) and pressure drop increase (Figure *18*C), the experiments done with air sparging show a similar trend of increase with time as the reference experiment. In other words, the air sparging does not lowers down the inorganic fouling build-up, at all. The voltage and pressure drop curves as shown in Figure *18*A and C were transformed to show the voltage and pressure drop development relative to the reference experiment (by calculations shown in *Appendix XI - Pressure drop and voltage increase (%) relative to the reference experiment)*. In Figure *18*B it shows that for 2 bar, the voltage increase ends higher than the reference experiment (since the curve ends >0%). This is probably due to the trapped gas inside of the stack which is demonstrated to increase pressure drop and voltage in earlier works (Moreno et al., 2017). At the end of the air sparging experiments, an effort was made to remove stagnant bubbles from the stack by applying back pressure (3x ~2-3 bar), but it showed no effect. For the 4 bar experiments, the data from > 2800 seconds is not reliable as the pressure drop reached the pump capacity, so the flowrate could not be guaranteed (Figure *18*, red line). However, still, the effect of the trapped gas in increasing the voltage and pressure drop is visible for time < 2800 s. As electrical energy consumption is dominant over pumping energy consumption (and the voltage increase was similar), the total energy consumption was comparable for 2 bar air sparging, 4 bar air sparging and the reference experiment (*Appendix X – Energy consumption*).

Unfortunately, air sparging seems to even increase the voltage and pressure drop compared to the reference experiments. Zooming in on the first 800 seconds of air sparging experiments for the 2 and 4 bar (Figure 19), it can be observed that after a 'sparge' (around 300 seconds), both the voltage and pressure drop show an increase.

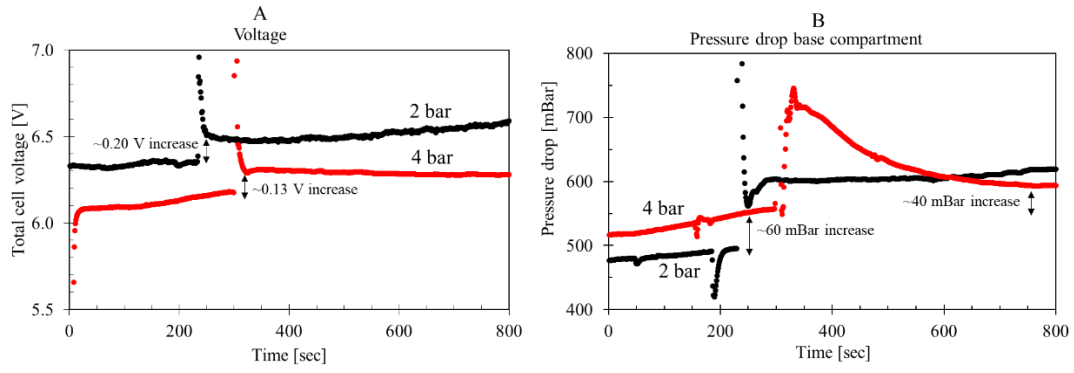

Figure 19, (A) Voltage and (B) pressure drop for the first 600 seconds of an air sparging experiment, for the original data from Figure 18A and C.

Figure 19 zooms in on the start of an experiment, to show that air sparging increases the pressure drop and voltage, even before these values start to increase due to inorganic fouling. In Figure 19B, the increase due to sparging with 4 bar air also decreases again, but not back to the original values. These results indicate that during air sparging, stagnant bubbles stay stuck in the compartments between the membranes. Stagnant bubbles increase the pressure drop due to decreasing the available flow area, so the flow velocity needs to increase to keep a constant flowrate. In addition to the pressure drop, stagnant bubbles also increase the voltage because air has a lower conductivity than synthetic seawater (~10^{-14} S·m^{-1} (Seran et al., 2017) vs. ~ 5 S·m^{-1}), causing resistance in the compartments to increase (Equation 16).

Despite the fact that air sparging was not found to be a sufficient anti-fouling method, it did result in minor inorganic fouling removal from the cell, as the glass compartment positioned at the cell outlet got a milky colour, every time after the air sparge, was observed during air sparging (Figure 20).

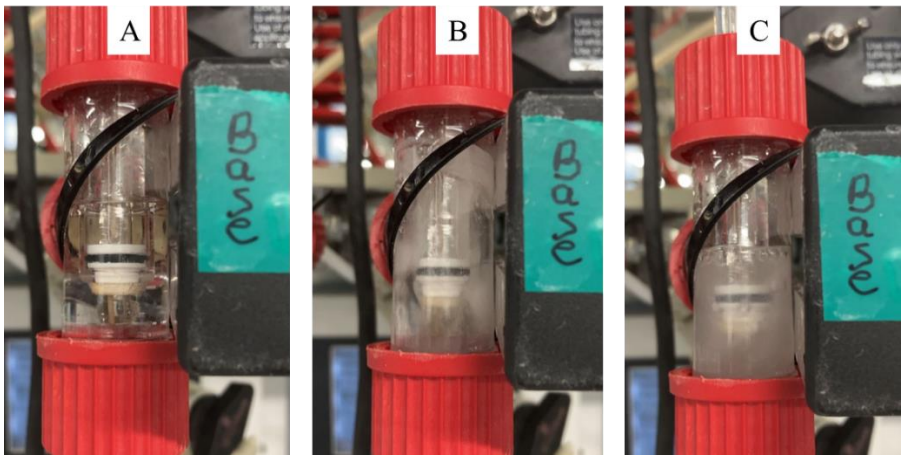

Figure 20, Base outlet (incl. pH meter) (A) before, (B) during, and (C) after air sparging with 4 bar, during an experiment with 72 mL·min^{-1} per compartment and 12.5 mA·cm^{-2} applied current density. The milky colour in C suggests presence of inorganic fouling (that has been washed away from the stack).

That this visible inorganic fouling removal did not result in a decrease of voltage and pressure drop can have multiple reasons; air sparging may removes inorganic fouling, but also causes stagnant bubbles in the stack, which does not result in a net decrease in voltage or pressure drop. If channels are formed in the spacers, then the air choses the ‘way of least resistance’ and only sparges the channels but not the rest of the compartment (Figure *14*).

Air sparging experiments were also done with 3 bar, which showed similar results as for 2 and 4 bar (*Appendix XIII – Air sparging repetition 2, 3 and 4 bar).* Air sparging under 1 bar pressure

was not sufficient as gas bubbles did not come out of the outlet of the base compartments and got fully trapped inside of the stack.

Efforts were made to improve air sparging efficiency. Sparging 3x 2seconds was expected to have higher efficiency than 1x 5 seconds (Moreno et al., 2017). However, no effect of the change in sparging regime was observed *(Appendix XIV – Air sparging regimes)*. Backpressure was applied after sparging to release stagnant bubbles, as it demonstrated to improve adverse effects of stagnant bubbles ((Moreno et al., 2017), supporting information S1), but this did not result in a direct decrease in voltage or pressure drop (*Appendix XV – Air sparging with back pressure*).

All in all, the results for air sparging shows that this not a sufficient method to remove inorganic fouling for this BPMED cell.

4.2.1.2. CO_2 (g) sparging

CO_2 sparging (2 and 3 bar) as a combined physical and chemical inorganic fouling removal; it has the physical aspect of bubble pushing out inorganic fouling and since CO_2 (g) will lower the pH when it goes into dissolution (Equation 3 - Equation 5) this method is also partly a chemical cleaning. Efficiency of the inorganic fouling removal was determined though the voltage, pressure drop, and pH curves (Figure 21 and Figure 22).

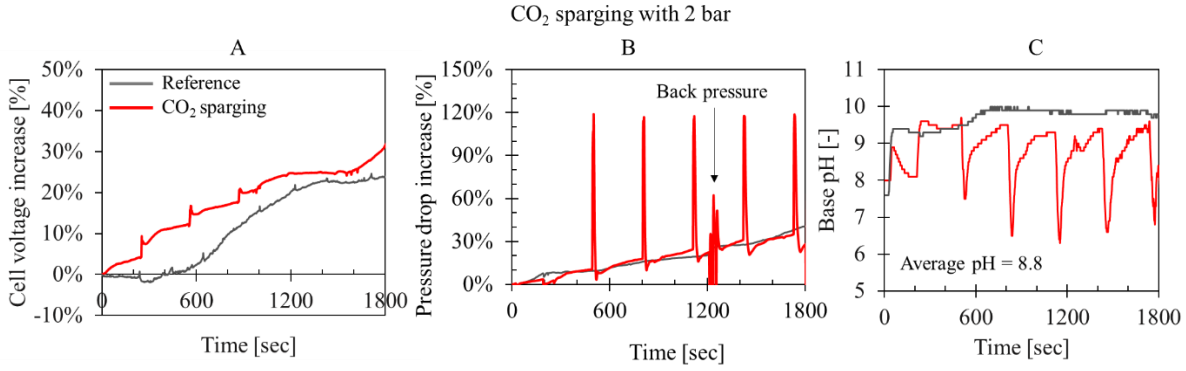

Figure 21, (A) voltage increase, (B) pressure drop increase in the base compartment and (C) bulk pH in the base outlet for experiments were CO_2 sparging under 2 bar pressure is compared to a reference experiment (no cleaning). The flowrate was 72 mL·min^{-1} per compartment with an applied current density of 12.5 mA·cm^{-2}. Sparging was done every 5 minutes 3x 2 seconds.

CO_2 sparging under 2 bar pressure did not suppress the increase of voltage or pressure drop in this experiment (Figure 21A, B). The pH lowers after a 'sparge' (Figure 21C) as CO_2 lowers the pH when it is dissolved into the feed.

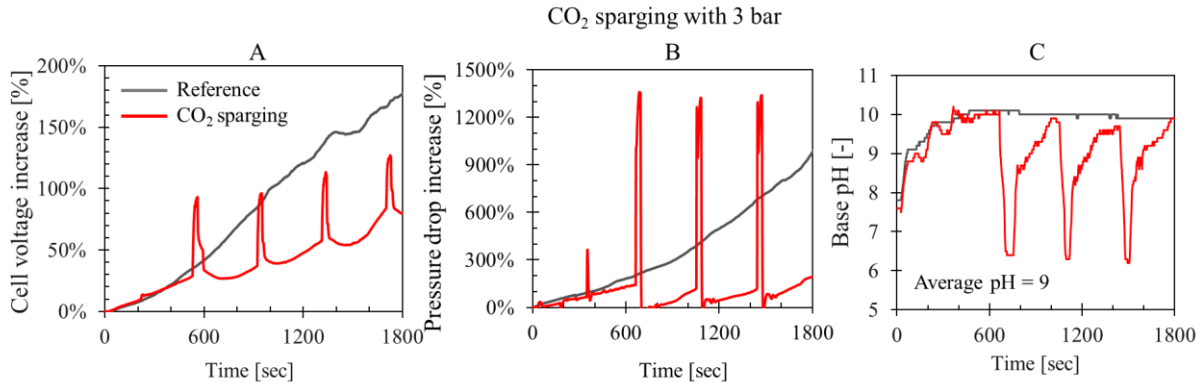

Figure 22,(A) voltage increase, (B) pressure drop increase in the base compartment and (C) bulk pH in the base outlet for experiments were CO_2 sparging under 3 bar pressure is compared to a reference experiment (no cleaning). The flowrate was 24 mL·min^{-1} per compartment with an applied current density of 15 mA·cm^{-2}. Sparging was done every 5 minutes 30 seconds.

For the experiment shown in Figure *22* more extreme conditions were used than for the other experiment (i.e., 24 mA·cm^{-2} per compartment and 15 mA·cm^{-2} vs. 72 mL·min^{-1} per compartment and 12.5 mA·cm^{-2}), which showed severe inorganic fouling for the reference experiment. CO_2 sparging under 3 bar CO_2 did suppress the increase of voltage and pressure drop (Figure *22* A, B). Voltage increased about 50% less and pressure drop about 700% less when CO_2 sparging was used. Sparging was done for 30 seconds, which explains why the 'pH dips' are broader in Figure 22C compared to Figure 21C.

Due to higher solubility of CO_2 (g) compared to air (1.3 ·10^{-3} kg·kg^{-1} (Teng et al., 1996) ~ vs. ~10·10^{-6} kg·kg^{-1} (G.Kuiper, 2012)), stagnant bubbles will eventually dissolved in the feed, as the feed is not saturated for $CO_{2\,(aq)}$ yet (the feed contains 0.0023 mM DIC vs a saturation of 33 mM for $CO_{2(aq)}$ (Teng et al., 1996)).

Results for DIC removal, Ca^{2+} and Mg^{2+} ions removal are shown in Table 3. For one sample calcite seeds (10 g·L^{-1}) were added to the sample bottle to enhance the calcite precipitation. Calcite seeds were added in an effort to avoid negative DIC removal during CO_2 sparging experiments.

Table 3, DIC, Ca^{2+} and Mg^{2+} removal of the base outlet of a 30-minute experiments with CO_2 sparging. One sample was taken the regular way and one sample was filled with calcite seeds for sparging with 2 bar.

	2 bar		**3 bar**
	Base outlet	**Base outlet+ calcite seeding**	**Base outlet**
pH after > 72h	8.3	7.9	7.5
DIC removal [%]	-105%	-78%	-257%
Ca^{2+} removal [%]	6%	10%	1%
Mg^{2+} removal [%]	10%	11%	5%

For all CO_2 sparging experiments, DIC removal was negative. For 2 bar applied pressure, there was removal of Ca^{2+} and Mg^{2+} ions, indicating that some mineral precipitation had taken place. Addition of calcite seeding resulted in a higher DIC removal and a higher Ca^{2+} ion removal, indicating (more) $CaCO_3$ removal when calcite seeds was added to the sampling bottle. As it was not known how much moles of CO_2 (g) was brought into the cell during sparging, it cannot be known for certain if $CaCO_3$ precipitated for 3 bar applied pressure, though the low calcium removal does not indicate precipitation of $CaCO_3$. There was removal of Mg^{2+} ion, indicating precipitation of magnesium containing minerals.

All in all, negative DIC removal goes against the main function of this BPMED system which is removing carbonate. Therefore, CO_2 (g) sparging was found to be unsuitable as inorganic fouling removal method.

Less experiment with CO_2 sparging were done, as the experiments are stopped in an early stage. Therefore, the experimental settings were different than for the other experiments, as they were done in the 'try-out' phase.

4.2.1.3. Influence of spacers in gas sparging

Initial experiments were done with without spacers in the base compartment to study the effect of spacers on fouling build-up and its removal. Compartments were supported by an outer frame only as shown in Figure *23*. It is important to note that this is not a reliable method to build a membrane stack because if the membranes have space to 'bulge', the compartment volume and thus flow velocity through the compartment cannot be controlled. However, For the sake of research, we have conducted tests without spacers.

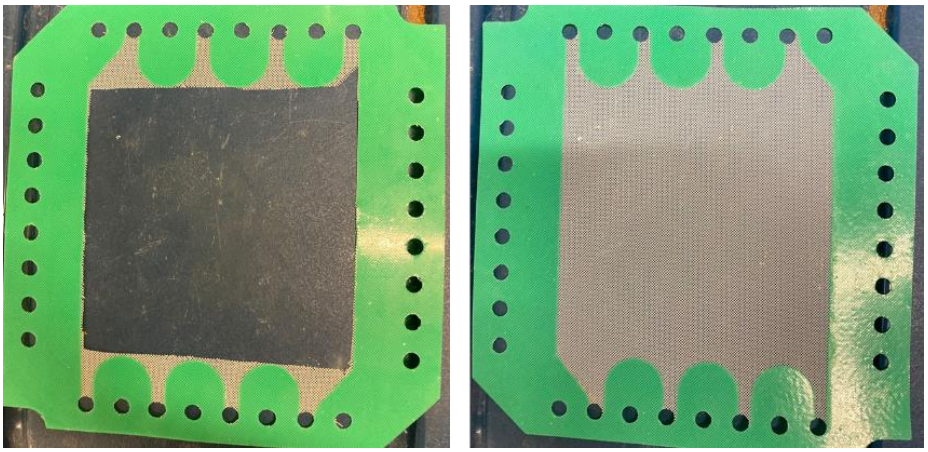

Figure 23, (A) alternative for spacers used for the base compartments. (B) spacers were used for the acid compartments.

30-minute experiments were done for 24 mL·min^{-1} per compartment (i.e., τ_r = 10 seconds) and 15 mA·cm^{-2} applied current density without spacers. Results for the voltage and pressure drop curve are shown in Figure 24.

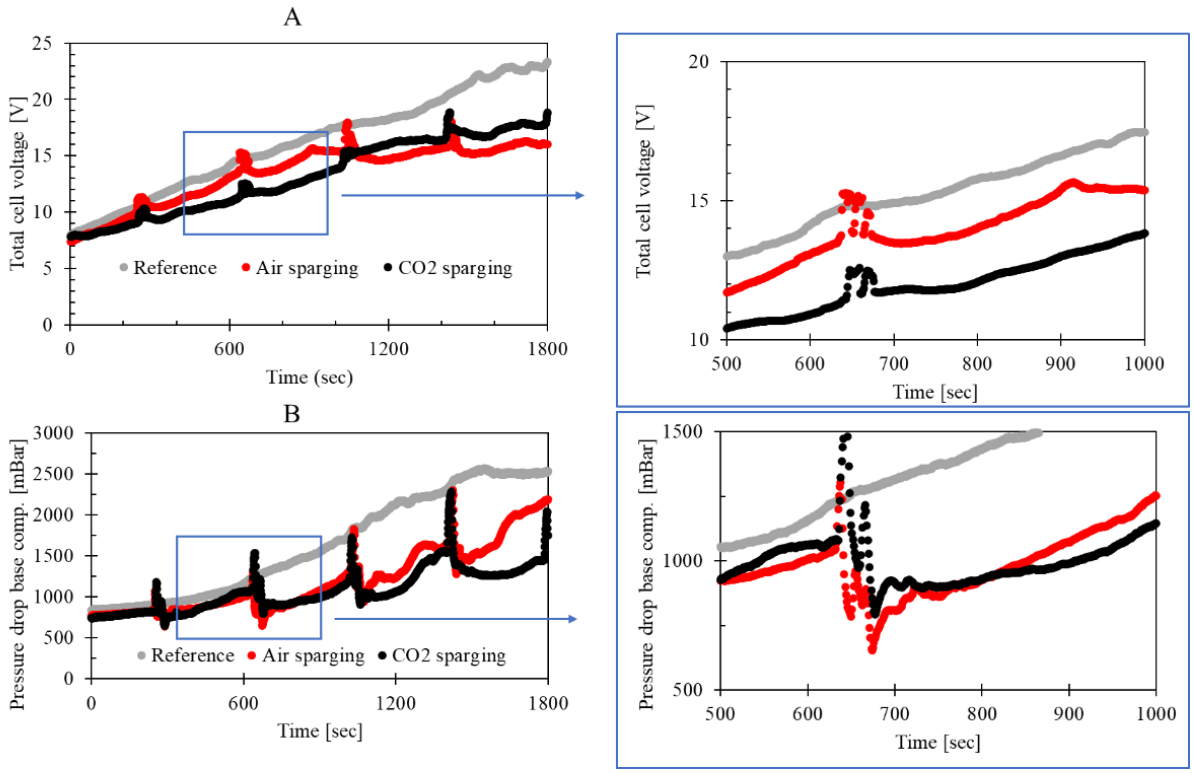

Figure 24 30-minute experiments without spacers. (A) Total cell voltage with a zoom in between t = 500-1000 and (B) pressure drop in the base compartment with a zoom in between t=500-1000. Sparging was done every 5 minutes for 30 seconds under 3 bar pressure. The flowrate was 24 mL·min^{-1} per compartment (i.e., τ_r = 10) and 15 mA·cm^{-2} applied current density.

For experiment without spacers, pressure drop decreases after a 'sparge' (zoom in Figure 24B). Afterwards pressure drop increase fast, because extreme current-flow rates were used resulting in severe and fast inorganic fouling. However, experiments where no spacers were used did not show indications for stagnant bubbles. Sparging does not completely recover the voltage and pressure drop, but it also does not increase their values. Therefore, it is suspected that the fine netting structure of spacers play an important part in trapping stagnant bubbles. Stagnant bubbles for air sparging in electrochemical cells with feed spacers were reported in literature as well (Moreno et al., 2017), as were for electrochemical cells with profiled membranes air sparging decreased pressure drop ~90% (Vermaas et al., 2014a).

4.2.2. Back pressure

Backpressure was applied on the base compartments by closing a valve at the outlet of the base compartments. An analog pressure gauge was used to measure the pressure build-up, which

could reach a maximum of 3 bar. Upon opening the valve, this pressure was released. Efficiency of the inorganic fouling removal was determined though the voltage and pressure drop curve, results are shown in Figure *25*.

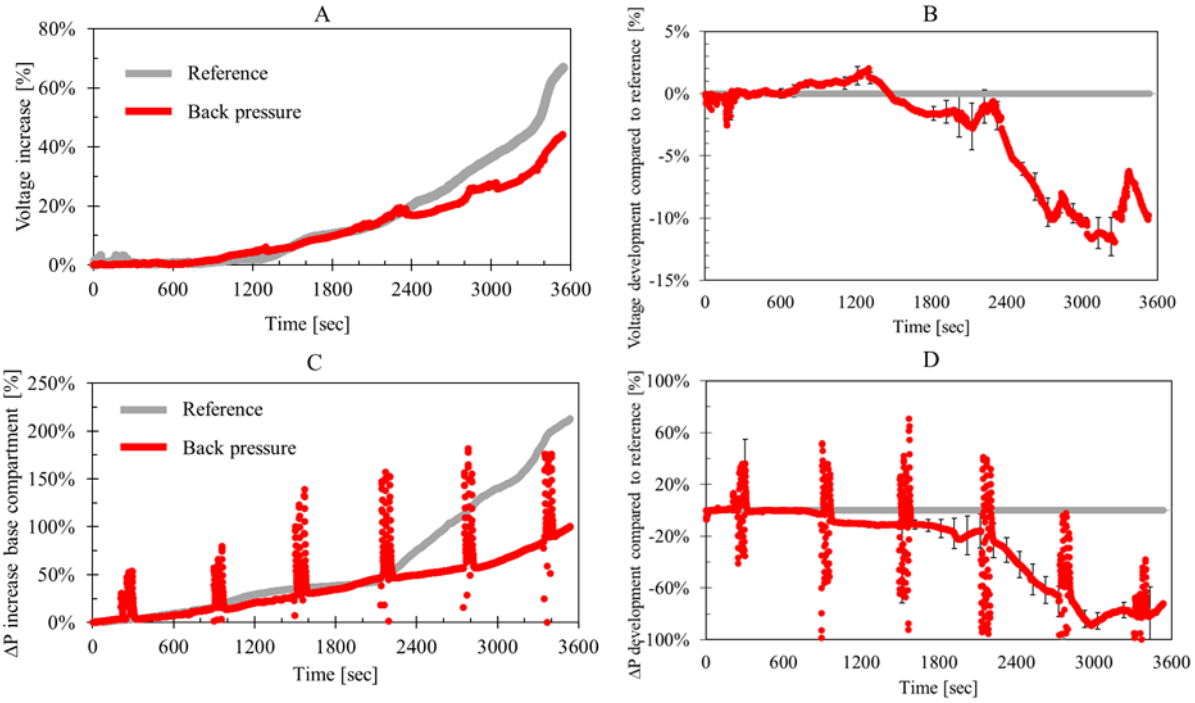

Figure 25, Application of back pressure every 10 minutes until 2-3 bar. Comparison of (A) voltage increase (%) and (C) pressure drop increase (%) with a reference experiment (with no cleaning method) are shown (for 1 repetition). Furthermore, the development of (B) the voltage increase (%) and (D) pressure drop increase (%) relative to the reference experiment is shown, the lines are average of 2 repetitions including the standard error as error bars. How the figure was made from raw data is shown in (*Appendix XI - Pressure drop and voltage increase (%) relative to the reference experiment*).

Application of backpressure reduced the increase of both voltage and pressure drop. The decrease of voltage is small compared to the reference experiment (about 10%) (Figure *25* B) , for both experiments. Application of backpressure does show a suppression of pressure drop increase compared to the reference experiment, for both experiments (Figure *25* C,D). Upon closing the value, Δp goes to zero as the flow is temporarily stopped. After opening the valve, Δp increases substantially due to the temporarily high flow flushing out of the stack (Figure *25* C, D). There are two ways back pressure application is suspected to decrease pressure drop: as the result of inorganic fouling removal and disruption of formed channels. Even though this method shows promising results regarding pressure drop reduction, reducing the voltage is also important since electrical energy consumption is the dominant fraction in energy consumption. That explains the energy consumption for the experiments with backpressure is similar to the energy consumption of the reference experiments (*Appendix XII – Energy consumption*

inorganic fouling removal experiments). Back pressure by itself is not considered sufficient as a method to remove inorganic fouling but can be combined with other inorganic fouling removal methods to increase their effectivity (as was done to for acid wash and tried for air sparging).

4.2.3. Temporary flowrate increase

The flowrate was increased to 5 and 15 times the operating flowrate (360 and 1080 72 mL·min^{-1} per compartment for an operating flowrate of 72 mL·min^{-1} per compartment) for 3 seconds using the pimp "prime" option. The results for the voltage and pressure drop curves are shown in Figure *26*.

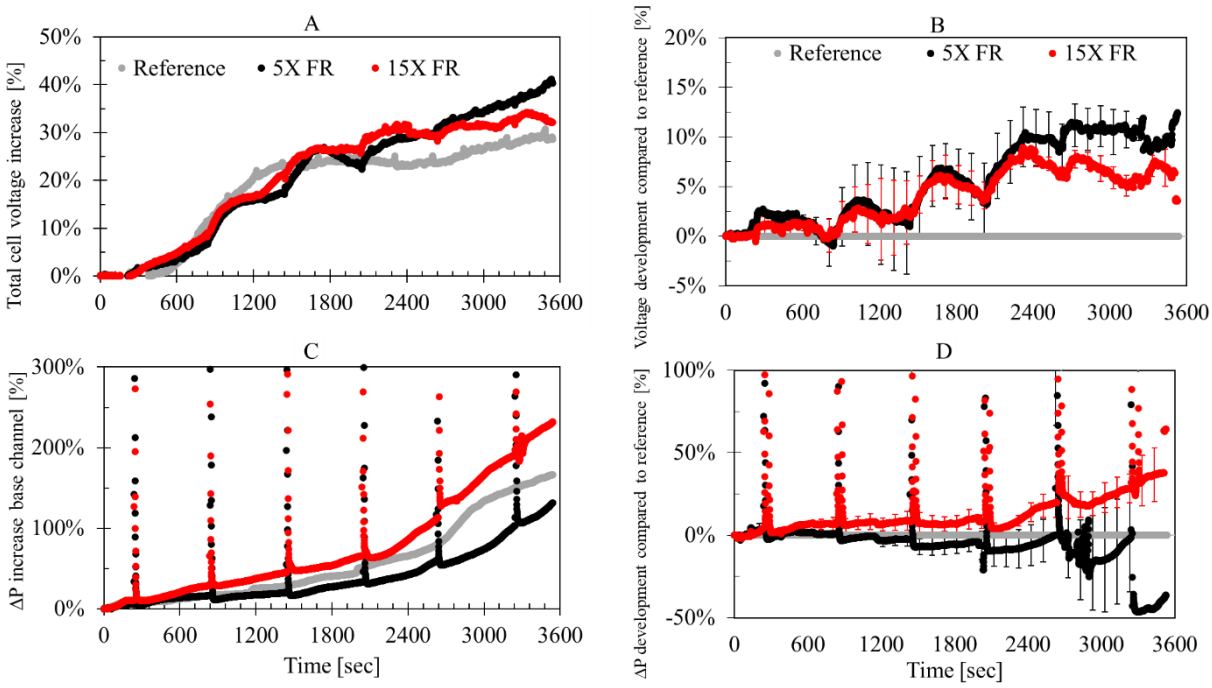

Figure 26, Comparison of (A) voltage increase (%) and (C) pressure drop increase (%) with a reference experiment (with no cleaning method) are shown (for 1 repetition). Furthermore, the development of (B) the voltage increase (%) and (D) pressure drop increase (%) relative to the reference experiment is shown, the lines are average of 2 repetitions including the standard error as error bars. How the figure was made from raw data is shown in (*Appendix XI - Pressure drop and voltage increase (%) relative to the reference experiment*).

When looking at the curves for voltage increase (Figure 26A) and pressure drop increase (Figure 26C), the experiments done with flowrate increase show a similar trend as the reference experiment . The voltage and pressure drop curves as shown in Figure 26A&C were transformed to show the voltage and pressure drop development relative to the reference experiment. For both flowrate increases the voltage increase was about 5-10% higher than the reference experiment (Figure 26B). For the pressure drop increase, both flowrate increases are the mostly in range with the reference experiments, when looking at the stand error bars (Figure

26D). Based on Figure 26, it can be concluded that flowrate increase did not effectively remove inorganic fouling. The energy consumption tells the same story as it was comparable for 5 times flowrate increase, 15 times flowrate increase and the reference experiment (*Appendix X – Energy consumption*).

That flowrate increase was not effective might be due to channel formation. If channels are formed before the flowrate increase, the feed follows these channels during the flowrate increase, cleaning the channels and not the whole compartment. This would also explain why there is little difference in results between 5- and 15-times flowrate increase.

4.2.4. Acid wash

Prior to the acid wash, the membranes were 'scaled' for 1 hour with 72 mL·min^{-1} per compartment (τ_r= 3.33 seconds) and 12.5 mA·cm^{-2} applied current density. For the acid wash experiments on the AEM-BPM configuration, some adjustments were made to improve the feasibility of acid wash. Acid wash was combined with back pressure application to ensure the compartments were filled with acid, to disrupt possible formed inorganic fouling channels and to decrease the cleaning time. Also, investigating acid wash with the acid produced by the bipolar membrane stack to avoid the use of extra chemicals.

When starting the acid wash, the pressure drop starts decreasing towards its initial value as the inorganic fouling inside of the cell is removed. The acid wash was continued until the rate of this decrease in the pressure drop was stabilized. After the acid wash, the pressure drop recovery was measured. To measure the pressure, drop recovery, the compartments were filled with synthetic seawater for a flowrate of 72 mL·min^{-1} per compartment. On example of a cleaning cycle, for the AEM-BPM configuration using hydrochloric acid for a velocity of 3 cm·s^{-1} in shown in Figure *27*. Pressure drop recovery was determined similar for all experiments; the results are shown in Figure *28*.

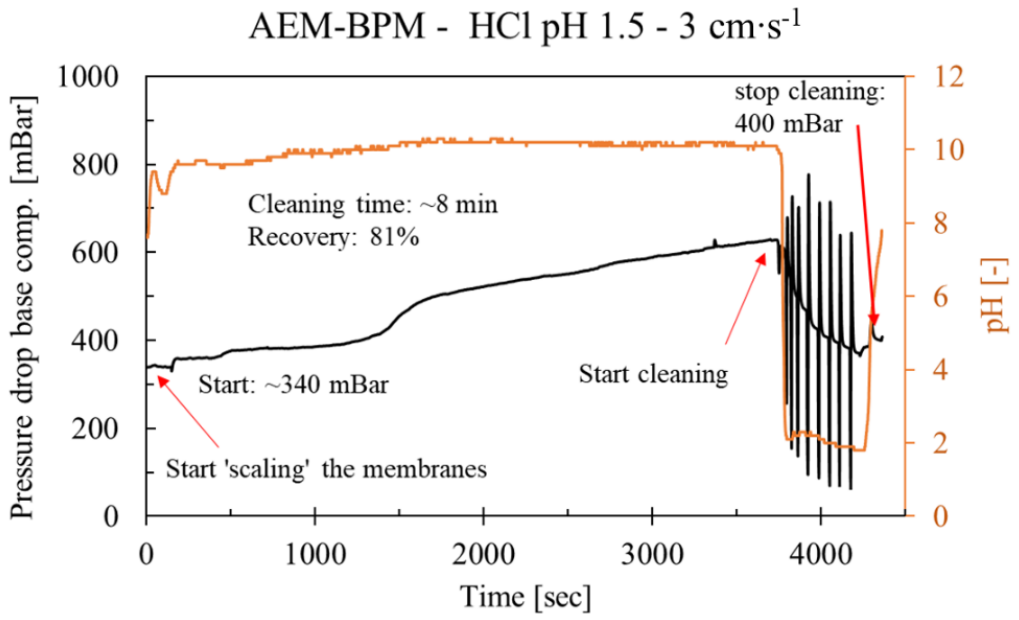

Figure 27, acid wash for AEM-BPM configuration using hydrochloric acid for a velocity of 3 cm·s^{-1}. Membranes were 'scaled' the first hour under 12.5 mA·cm^{-2} applied current density and 72 mL·min^{-1} per compartment. Cleaning time (between start and stop) was ~5 minutes (600 seconds), the peaks show application of backpressure. Once pressure drop decrease stabilized, the compartment was filled with synthetic seawater (explaining the increase at the end of the curve), to determine the pressure drop after cleaning.

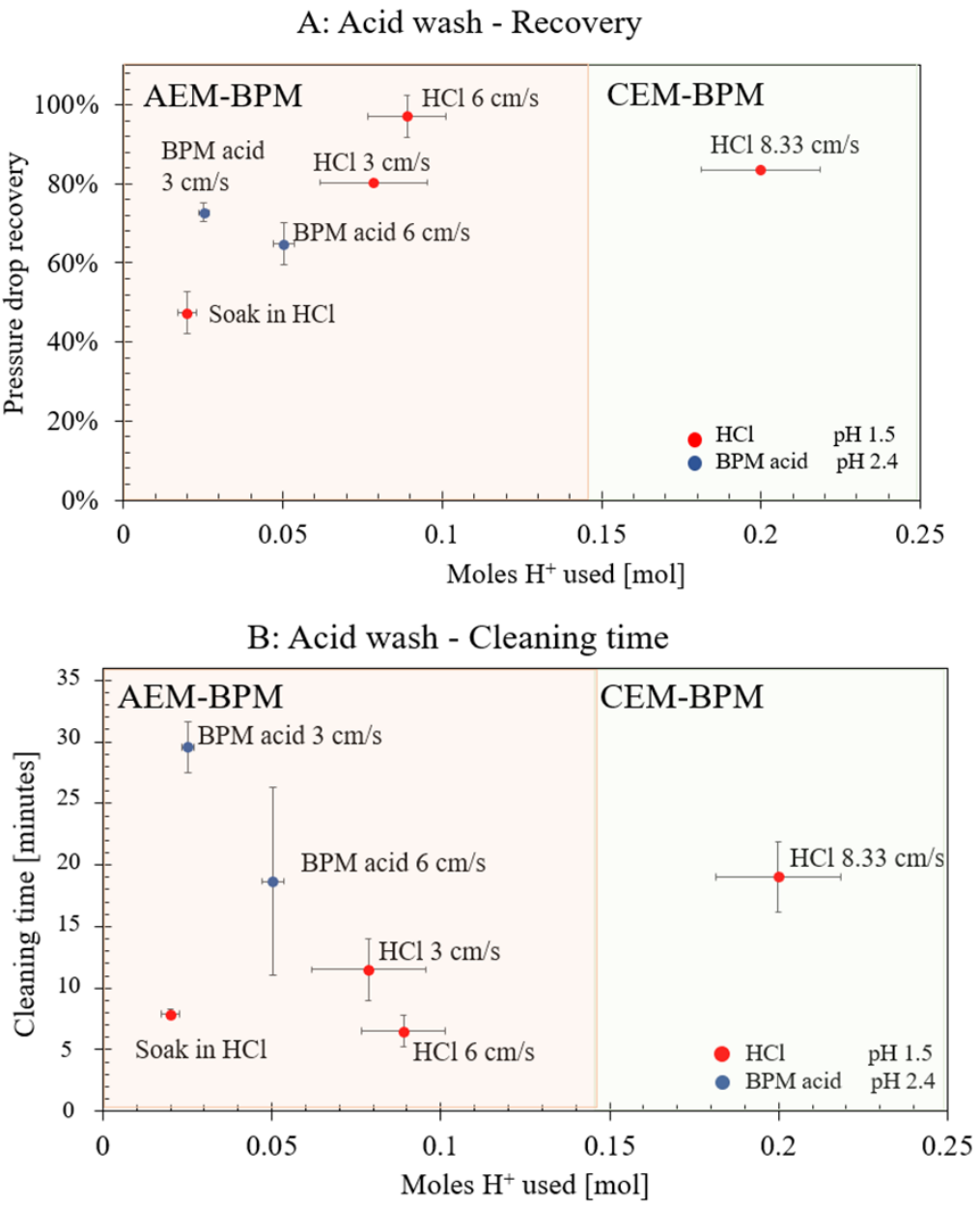

Figure 28, Left, orange are: AEM BPM results. Right, green area: CEM-BPM results. (A) Recovery of pressure drop and (B) cleaning time are plotted against the amount of moles needed during the cleaning. Cleaning time was noted when the pressure drop stabilized, (not decreasing anymore), and recovery was relative to the initial pressure drop. Results are the average of 2 repetitions (4 repetitions for HCl 6 $cm \cdot s^{-1}$) and the standard error is shown, when the error bar is not visible, it is smaller than the marker size. All data from the graphs is shown in *Appendix XV – Acid wash*.

The acid produced by the BPM was stirred for ~1 hour rigorously to allow the carbonic acid and dissolved CO_2 to (partially) leave the solution as CO_2 (g). Acid wash for the CEM-BPM configuration had a comparable pressure drop recovery as for the AEM-BPM configuration (Figure *28*A). However, CEM-BPM need more moles of H^+ ions for the acid wash. Since the cleaning time was longer than the cleaning time with hydrochloric acid for AEM-BPM (Figure *28*B) and the acid wash was done with a higher flowrate. Recovery of voltage was 100% for

both experiments ($V_{initial}$ were 6.43 and 6.22 , $V_{after\ acid\ wash}$ were 6.30 and 6.17 for the two experiment, respectively).

For the AEM-BPM configuration, the highest recovery (close to 100%) was reached using hydrochloric acid at 2 times the operating flow velocity (HCl 6 $cm \cdot s^{-1}$) (Figure *28*A). Doubling the flowrate during acid wash decreases the cleaning time (as a higher flowrate adds a physical aspect to the cleaning method, where the inorganic fouling is pushed out due to the higher shear stress of a higher flow velocity) (Figure *28*B) (Equation 18). As for the effect of the flow velocity, for hydrochloric acid, the method with the increased flowrate shows a slightly higher (pressure drop) recovery (Figure *28*a). However, this is not the case for the BPM acid as a higher recovery is achieved with a lower flow velocity (Figure *28*A, blue marks).

As for the type of the acid, cleaning with hydrochloric acid shows a higher pressure drop recovery than when using the BPM acid. Possible reasons are that firstly, the hydrochloric acid HCl has a lower pH (i.e., a higher concentration H^+ ions of $10^{-1.5}$-$10^{-2.4}$ = 0.0278 M H^+ more compared to the BPM-produced acid). A higher H^+ concentration enhances dissolution of carbonate scaling. Secondly, the acid produced by the bipolar membrane contains ca. ~0.01 M Ca^{2+} and 0.051 M Mg^{2+} ions which decreases the carbonate minerals dissolution compared to hydrochloric acid which does not contain any Ca^{2+} and Mg^{2+} ions (Equation 7).

Backpressure application fastened the decrease of pressure drop and disrupted formed channels (figures showing the pressure drop curves during acid cleaning (on figure per method) are shown in *Appendix XV – Acid wash*).

Soaking the electrochemical cell in acid has the advantage of needing the lowest amount of Moles H^+ but also the lowest recovery(~50%) (Figure *28*A), which not makes it an attractive method. Using acid which is produced by the bipolar membrane showed a maximum pressure drop recovery was 70-80% (Figure *28*A, blue marks). Cleaning with hydrochloric acid shows a recovery time close to 100% and has the shortest cleaning time. Recovery values in literature after chemical cleaning vary, *'top'* recovery's were found between 80-95% (Kim et al., 2021), (Peng et al., 2015), (Wang et al., 2011) (e.g., Wang et al., 2011 found an 80% Mg^{2+} and 97.5% Ca^{2+} removal for CEM using 1% HCl). This means that recovery < 100% is acceptable in application.

The use of BPM produced acid has two main advantages over the use of hydrochloric acid. Firstly, the costs of buying hydrochloric acid can be avoided. The price of producing one mole of H^+ using the BPM with 5-10 $mA \cdot cm^{-2}$ and 72 $mL \cdot min^{-1}$ per compartment is € 0.94 -1.34

(calculation in *Appendix X – Energy consumption*), were the price of buying one mole HCl is € 13.58 (based on the price at Wetsus). Secondly, BPM produced acid can be reused as feed for the acid compartment of the BPMED cell, creating a 'zero waste' method. Through the acid route, carbonate that is dissolved in the acid after cleaning scaling can be removed from the acid as CO_2 gas. To make the recovery of BPM produced acid more compatible with hydrochloric acid, producing the acid could be optimized, as for these experiments the produced acid was not aimed for a certain pH. Recirculating the acid outlet with the aim to create a batch of acid with lower pH for cleaning could improve the cleaning efficiency while avoiding the need for additional chemicals.

Based on these results, it was concluded when time and recovery are considered the most important hydrochloric acid wash with 6 $cm \cdot s^{-1}$ is the most suitable method. When sustainability and cost (no external chemicals) are considered most important, BPM acid with 3 $cm \cdot s^{-1}$ is most suitable.

4.2.5. Inorganic fouling removal methods: comparison of the carbonate removal

Five inorganic fouling removal methods were tested for the oceanic carbon capture via in situ mineralization using BPMED system. When evaluating the DIC removal, methods cleaning efficiency, whether it was an In-process method (e.g., air sparging, the production of $CaCO_3$ did not have to be stopped during air sparging), and requirements for additional chemicals were considered. The DIC removal for the different methods is shown in Figure 29.

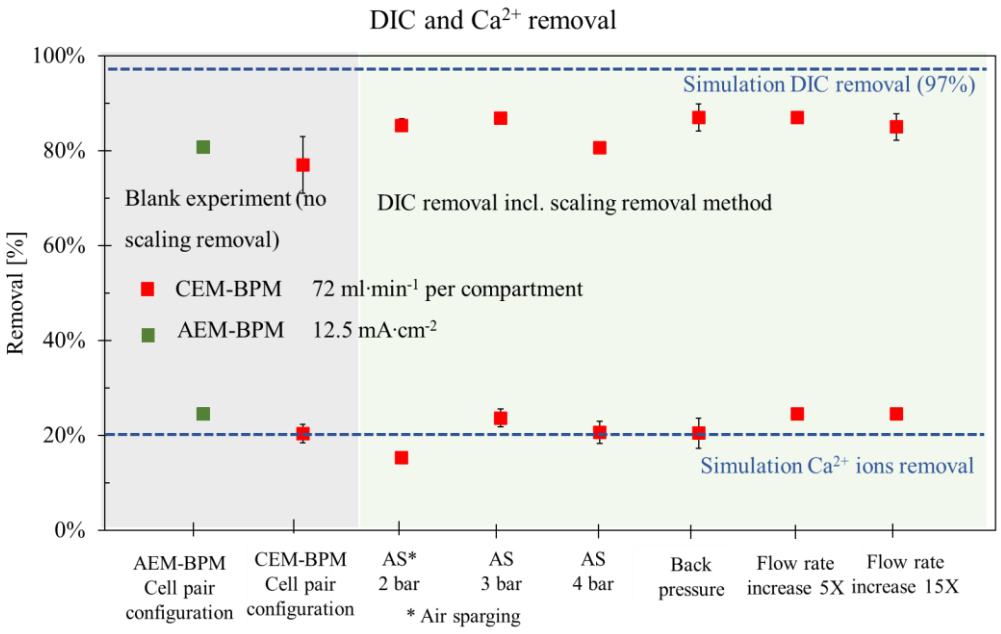

Figure 29, left side Grey area: 1-hour experiments without intermitted inorganic fouling removal for AEM-BPM (12 repetitions) and CEM-BPM (6 repetitions). Right side green area: 1 hour experiments incl. the inorganic fouling removal

method. During the inorganic fouling removal, the outlet was gathered in settling tanks. Air sparging shows the average of 3 repetitions, the other methods 2 repetitions. Error bars show the standard error. The original data is shown in *Appendix XVI – DIC and Ca^{2+} removal per method*.

When an experiment includes the inorganic fouling method (green area in Figure *29*), this means that during for example air sparging or flowrate increase the outflow is collected in the settling tank. Therefore, if the inorganic fouling removal method influences DIC removal this will show in Figure *29*. However, values for DIC removal and Ca^{2+} ion removal are similar for all experiments (~80-90% and ~20%), except for CO_2 (g) which had negative DIC removal (Table *3*). That measured DIC removal is lower than the simulated removal was also observed in (Figure *16*) including possible reasoning in (3.2.2 Inorganic fouling control). During acid wash, the base outlet was not captured in the settling tank but discharged and is therefore not included in the figure.

Insufficient cleaning efficiency and/or negative influence on DIC removal immediately eliminate an inorganic fouling removal method. Therefore, air sparging, flowrate increase and CO_2 sparging were not considered sufficient inorganic fouling removal methods to use for oceanic carbon capture via in situ mineralization using BPMED. All in all, it was found that a combination of acid wash was the most effective inorganic fouling removal methods for the process. Combining this method with increasing the flowrate and applying backpressure reduces the drawback of having to stop the production during cleaning. During these experiments hydrochloric acid resulted in the highest recovery. However, BPM produced acid has several advantages over hydrochloric acid, though optimizations are required to make the cleaning time and recovery compatible with hydrochloric acid.

4.3. Outlook

In this outlook, the influence of choices made during this research on results are discussed and what the results mean for the technology.

The synthetic seawater contained the first seven major ionic components, the remaining ions were replaced by either Na^+ or Cl^- ions, to ensure electron neutrality of the solution (Sharifian et al., n.d.). Figure *3* does not show the saturation index for K^+, Na^+ or SO_4^{2-} ions containing minerals. Especially sulphate containing minerals are important to address, since gypsum ($CaSO_4$) was reported to be the second most common scale found in reverse osmosis during seawater desalination, after calcium carbonate (S. G. Salinas et al., 2021). However, for this synthetic seawater, sulphate containing minerals showed a saturation index < 0 for a pH range

of 8-13.5 (*Appendix XVII – SI values for pH > 12*), the effect of possible concentration polarisation was not considered. Ionic components that were not included in the synthetic seawater were: 13 mg/L Strontium (Sr^{2+}), 65 mg/L Bromide (Br^-), 26 mg/L Borate (BO_3^{3-}), 1 mg/L Fluoride (F^-), 1 mg/L Silicate (SiO_3^{2-}), < 1 mg/L Iodide (I^-) based on the composition of typical seawater by Lenntech B.V.. Not including these could affect the results for fouling control and removal, if these ionic components would play a role in mineral precipitation. This depends on their typical concentrations and influence of pH on their saturation index. Solubility of pure salts were compared with salt concentrations in typical seawater (*Appendix XVIII – solubility of pure salts*). In addition to $CaCO_3$, $SrCO_3$ exceeded the maximum solubility based on pure water. The solubility product of $SrCO_3$ is lower than for $CaCO_3$ ($5.60 \cdot 10^{-10}$ vs $3.36 \cdot 10^{-9}$ (Lide, 2000)), and could consequently be harder to remove using acid wash. Even though solubility for SiO_3^{2-} containing minerals were not found, silicate precipitation is reported as a scaling risk in literature (about R.O. desalination) above neutral pH (Antony et al., 2011). Above pH 8-9 the formation of silicon anions is favourable, and precipitated as Mg-silicate (Tong et al., 2019). This is undesired because silica scaling is reported to be difficult to prevent and remove (Tong et al., 2019), (Li et al., 2011) and was reported especially on AEM (Wei et al., 2021). Therefore, this was a potential obstacle that was not considered in this research.

For the fouling removal experiments an environment was created to *''push for scaling''*, thereby creating conditions more severe as to normally running the process. Consequentially, other minerals may precipitate that are harder (or easier) to clean than minerals that precipitate under milder conditions. The most pronounced difference is that under accelerating scaling conditions more hydroxide containing minerals are expected to precipitated, as a consequence of pH increase (Figure 15E) and the and the accompanying influence on the saturation index (Figure 3). Even though a pH > 12 was not expected (Figure 15), local pH might increase more than expected if local flow velocity decreases due to channelling. For a pH > 12, precipitation of MgO and $Ca(OH)_2$ is thermodynamically possible (*Appendix XVII – SI values for pH > 12*). If hydroxide containing minerals (and MgO) are harder (or easier) to remove than calcium carbonate is valuable to know when interpreting the results. For acid wash the solubility product (K_{sp}), molecule size and effect of pH to the saturation index were considered. $Ca(OH)_2$ has a higher solubility product ($K_{sp} = 5.02 \cdot 10^{-6}$) than $CaCO_3$ ($K_{sp} = 3.30610^{-9}$), but $Mg(OH)_2$ lower ($K_{sp} = 5.61 \cdot 10^{-12}$) (Lide, 2000), for MgO the solubility product was not found. However, for hydroxide containing minerals the saturation index decreases fast when the pH decrease (*Appendix XVII – SI values for pH > 12*) and they are smaller in size than $CaCO_3$ (Cordero et

al., 2008). All in all, $Ca(OH)_2$ should be easier removed by acid wash than $CaCO_3$, for MgO this is unknown and for $Mg(OH)_2$ dependents on which of the factors affecting solubility weights heavier. However, (Wang et al., 2011) reported ~80% Mg^{2+} removal and 97.5% Ca^{2+} removal using 1% HCl to clean CEM fouled with $Ca(OH)_2$, $CaCO_3$ and $Mg(OH)_2$, indicating $Mg(OH)_2$ indeed is 'harder' to clean than $CaCO_3$. For physical fouling removal methods, this would depend on if one type of mineral would 'stuck' stronger to the membranes and spacers than others.

Due to the accelerating scaling conditions, the feasibility of the acid wash method cannot be judged based on the results. First, it is not known how often acid wash would be needed when the process is running under 'normal' conditions. A time frame in which voltage increased for the AEM-BPM configuration was not yet found. The maximum time the system ran with the AEM-BPM configuration was 120 minutes with 12.5 $mA \cdot cm^{-2}$ applied current density and 72 $mL \cdot min^{-1}$ per compartment *(Appendix XIX – AEM-BPM experiment 120 minutes*). To make a comparison of what this means, the running time can be expressed in Coulombs: $\frac{i \cdot A}{q} = \frac{0.0125 \cdot 100}{(\frac{72}{6000})}$ = 1042 Coulombs /L which for a 120-minute experiment is 27000 Coulombs. This means that the process can run for more than 27000 coulombs, without an increase of voltage. For example, when applying 5 $mA \cdot cm^{-2}$ applied current density and 72 $mL \cdot min^{-1}$ per compartment, the process could run for 5 hours.

However, the results can be used to determine if cleaning with BPM produced acid is realistic. With an applied current density of 5-10 $mA \cdot cm^{-2}$ and 72 $mL \cdot min^{-1}$ per compartment 0.028-0.084 moles H^+ ions per hour is produced, assuming it is equal to the OH^- production (Figure 15E). For the AEM-BPM configuration the moles of H^+ used for acid wash was < 0.1 moles per cleaning, meaning the electrochemical cell must run for 1.19 - 3.57 hours to produce enough H^+ ions, which seems realistic based on the voltage increase of the AEM-BPM configuration. In this research, pressure drop could be a limiting factor due to the capacity of the pumps. However, when upscaling the process, basing the cleaning interval on voltage increase is more relevant as the pumping losses are very small compared to the electrical energy consumption (Figure 17).

When looking at the frequency of cleaning in place (CIP) in literature, this shows a large variety. An extensive survey reported that short treatments (e.g., backwash) frequented between 5 and 96 (median 32) times per day and more intensive cleaning (e.g., chemical cleaning) between 0.2 and 50 (median 4) times per year (Porcelli & Judd, 2010). Therefore, feasibility of CIP is

different per case. For this case, a guideline could be that the use of H^+ must be lower than the production of $CaCO_3$. For 72 $mL \cdot min^{-1}$ per compartment and a DIC removal of 80% based on 2.1 mM DIC in the feed, 0.1 M $CaCO_3$ is produced after 4.6 hour, which based on voltage increase seems realistic. Intermitted application of backpressure to avoid/disrupt formed channels can be done as much as deemed necessary.

In this research, a black box approach was used were the overall fouling behaviour of the BPMED cell was measured. Factors as local pH, channelling or where scaling precipitates were not known based on the measurements, though they did provide an indication. Measuring both pressure drop and voltage proved to be valuable. Pressure drop is very sensitive and reacts to scaling immediately but is also sensitive to other factors such as dust and channelling. Voltage seemed to be mostly sensitive to membrane fouling. Voltage is an important parameter because the electrical energy consumption is the larger part of the energy consumption. For a *'proof of concept*' research as this one, the black box approach was considered sufficient, since the goal was discover what works and what doesn't. In depth investigation of fouling formation and were in the compartment it precipitates can be interesting when optimizing this BPMED system, based on the results of this *'proof of concept'*.

5. Conclusions

Oceanic CO_2 capture technology can be used as a negative emission technology, or pre-treatment to reduce inorganic fouling (i.e., scaling) potential when further processing seawater. In this work CO_2 from (synthetic) seawater was captured via an electrochemical created pH-swing. Although previous studies showed promising results regarding energy consumption (330 kJ/mole $CaCO_3$), inorganic fouling in the base compartment of the cell is a drawback. The inorganic fouling control and removal in the base compartments during in the in-situ CO_2 capture from (synthetic) seawater via bipolar membrane electrodialysis (BPMED) was researched.

First, the fouling *control* strategies including the effect of process parameters and cell design was investigated; the effect of applied current density and flowrate (i.e., cell residence time) on inorganic fouling build-up and carbonate removal was tested for two cell configurations of (1)AEM-BPM and (2) CEM-BPM cell pairs. The inorganic fouling build up was measured through increase in cell total voltage, ohmic resistance, and increase in stack pressure drop. We found that the inorganic fouling build-up was lower for a higher flowrate (72 $mL \cdot min^{-1}$ per compartment vs. 24 $mL \cdot min^{-1}$ per compartment) in combination with low current density of 5 $mA \cdot cm^{-2}$). The AEM-BPM configuration was less sensitive to inorganic fouling than the CEM-BPM configuration; while the stack voltage for the CEM-BPM configuration increased to 130% within 30 min experiments, the stack voltage for the AEM-BPM configuration did not increase significantly. The CEMs are probably more prone to inorganic fouling (compared to AEM) because Ca^{2+} and Mg^{2+} ions accumulate near the CEM surface in the base compartment (i.e., concentration polarization that increases the saturation index of carbonate and hydroxide minerals, locally on the surface of the membrane). The pressure drop increased for both cell pair configurations, indicating inorganic fouling build-up. The lowest energy consumption was reached for the AEM-BPM configuration (637 kJ/mole $CaCO_3$), the difference with the lowest energy consumption for CEM-BPM is small (660 kJ/mole $CaCO_3$) but this difference is expected to increase over time since electrical energy consumption is dominant.

Based on simulations done using Visual MINTEQ 3.1, the theoretical dissolved inorganic carbon (DIC) removal for base-pH > 9.5 is ca. 97% regardless of the cell pair configurations. However, in the experiments, a maximum of ~85 % removal was achieved.

Regarding the inorganic fouling *removal*, five methods incl. (1) air sparging (2) CO_2 (g) sparging, (3) flowrate increase (5x and 15x), (4) applying backpressure, and (4) acid wash

(using HCl and BPM-produced acid) were tested. For both cell configurations, the acid wash showed the highest recovery, measured through pressure drop and cell voltage recovery. Based on these results, cleaning with BPM produced acid is cheaper and more sustainable than cleaning with HCl, though cleaning with HCl resulted in a higher recovery and shorter cleaning time. Combining the acid wash with backpressure application was used to reduce cleaning time. The backpressure as solo method suppressed (not fully recovered) the pressure increases and resulted in slightly lower (10%) voltage increase. Air sparging was done at pressures of 2, 3, and 4 bar, with spargin intervals of 10 min for 5 seconds and 3×2 seconds. In all cases, air sparging increased the cell voltage and pressure drop even more because of stagnant bubbles that got trapped within the cell-spacers. The type and area-density of the spacers netting was found to play a role in 'trapping' the stagnant bubbles. CO_2 gas sparging did show suppression of the voltage and pressure drop increase (even though no full recovery was achieved), but also caused negative DIC removal instead of carbonate extraction. Voltage and pressure drop curves for the temporary increase of flowrate were similar as for reference experiments (no cleaning). The DIC removal was comparable for all methods (75-85%), accept the CO_2 sparging where negative removal was seen.

Looking back on this research, the AEM-BPM configuration had the lowest energy consumption for $CaCO_3$ production. Combining this cell design with (optimized) intermitted acid wash would be recommended based on this work, as only acid resulted in sufficient recovery. However, since this research was a *proof of concept* optimization is needed to make the energy consumption compatible with that of previous studies.

6. Recommendations

Main opportunities for improvement for future follow up studies are (1) process optimization (by increasing cell production and optimizing acid wash), (2) alternatives for woven spacers such as use of profiled membranes, and (3) expand research to use real seawater to include other form of fouling incl. bio-fouling, organic fouling, and colloidal fouling.

As this research was a proof of concept, optimizations are needed to make the energy consumption to produce $CaCO_3$ compatible with that of previous studies (330 kJ/mole $CaCO_3$ was found for a CEM-BPM configuration with 10 cell pairs (Boer, 2020)) . Inorganic fouling control studies were done using a cell stack with 3 cell pairs, increasing the numbers of cell pairs makes the $CaCO_3$ production more energy efficient, as was proven in previous studies. In the current work, the experiments were done under conditions that 'pushed' for inorganic fouling to include the "worst case scenarios". When lower applied current density is used (5 – 10 $mA \cdot cm^{-2}$), the interval and duration of fouling removals can be optimized, increasing the methods feasibility. Avoiding the use of external chemicals also provides an opportunity to increase feasibility, when for example, the acid produced by the BPM is used for cleaning rather than pure HCl. To reduce the use of acid, more research can be done on combining acid wash with a chemical free method. A combination with ultrasound treatment was proven effective to remove inorganic fouling from surface and inside a CEM (Wang et al., 2011) and is recommended for a follow up study.

The compartment spacers which had a fine woven structure caused challenges in fouling build-up (as spacers are sensitive to fouling) and removal (as spacers enhance 'trapping' stagnant bubbles). Using an alternative for these spacers provides an opportunity to further investigate gas sparging as a fouling removal method, as it has proven to be an effective method for electrochemical cells in other studies. The use of profiled membranes is a known alternative for the use spacer.

Finally, before upscaling, experiments using real seawater should be done combined with a study of organic fouling and biofouling, as the composition of real seawater expands the types of fouling that pose a risk beyond just inorganic fouling.

References

Agrahari, G. K., Verma, N., & Bhattacharya, P. K. (2011). Application of hollow fiber membrane contactor for the removal of carbon dioxide from water under liquid-liquid extraction mode. *Journal of Membrane Science*, *375*(1–2), 323–333. https://doi.org/10.1016/j.memsci.2011.03.060

Antony, A., How, J., Gray, S., Childress, A. E., Le-clech, P., & Leslie, G. (2011). Scale formation and control in high pressure membrane water treatment systems : A review. *Journal of Membrane Science*, *383*(1–2), 1–16. https://doi.org/10.1016/j.memsci.2011.08.054

Barde, P., & Barde, M. (2012). What to use to express the variability of data: Standard deviation or standard error of mean? *Perspectives in Clinical Research*, *3*(3), 113. https://doi.org/10.4103/2229-3485.100662

Berre, O. Le, & D, G. (1996). Skimmilk crossflow microfiltration performance versus permeation flux to wall shear stress ratio. *Journal of Membrane Science*, *117*, 261–270.

Boer, L. (2020). *Electrochemical Seawater CO 2 Capture through In-Situ Carbonate Mineralization via Bipolar Membrane Electrodialysis (BPMED)* (Issue September 2020). University of Twente.

Casademont, C., Farias, M. A., Pourcelly, G., & Bazinet, L. (2008a). Impact of electrodialytic parameters on cation migration kinetics and fouling nature of ion-exchange membranes during treatment of solutions with different magnesium/calcium ratios. *Journal of Membrane Science*, *325*(2), 570–579. https://doi.org/10.1016/j.memsci.2008.08.023

Casademont, C., Pourcelly, G., & Bazinet, L. (2008b). Effect of magnesium/calcium ratios in solutions treated by electrodialysis: Morphological characterization and identification of anion-exchange membrane fouling. *Journal of Colloid and Interface Science*, *322*(1), 215–223. https://doi.org/10.1016/j.jcis.2008.02.068

Cordero, B., Gómez, V., Platero-Prats, A. E., Revés, M., Echeverría, J., Cremades, E., Barragán, F., & Alvarez, S. (2008). Covalent radii revisited. *Journal of the Chemical Society. Dalton Transactions*, *21*, 2832–2838. https://doi.org/10.1039/b801115j

de Lannoy, C. F., Eisaman, M. D., Jose, A., Karnitz, S. D., DeVaul, R. W., Hannun, K., & Rivest, J. L. B. (2018). Indirect ocean capture of atmospheric CO2: Part I. Prototype of a negative emissions technology. *International Journal of Greenhouse Gas Control*,

70(October 2017), 243–253. https://doi.org/10.1016/j.ijggc.2017.10.007

Digdaya, I. A., Sullivan, I., Lin, M., Han, L., Cheng, W. H., Atwater, H. A., & Xiang, C. (2020). A direct coupled electrochemical system for capture and conversion of CO2 from oceanwater. *Nature Communications*, *11*(1), 1–10. https://doi.org/10.1038/s41467-020-18232-y

Eisaman, M. D., Alvarado, L., Larner, D., Wang, P., Garg, B., & Littau, K. A. (2011). CO2 separation using bipolar membrane electrodialysis. *Energy and Environmental Science*, *4*(4), 1319–1328. https://doi.org/10.1039/c0ee00303d

Eisaman, M. D., Parajuly, K., Tuganov, A., Eldershaw, C., Chang, N., & Littau, K. A. (2012). CO2 extraction from seawater using bipolar membrane electrodialysis. *Energy and Environmental Science*, *5*(6), 7346–7352. https://doi.org/10.1039/c2ee03393c

Elger, D. F. B. C. W. C. T. C. J. A. R. (2012). *ENGINEERING FLUID MECHANICS*.

G.Kuiper. (2012). *Appendix A Air Content of Water*. TU Delft OpenCourseWare. https://ocw.tudelft.nl/wp-content/uploads/Appendices.pdf

Ghalloussi, R., Garcia-Vasquez, W., Chaabane, L., Dammak, L., Larchet, C., Deabate, S. V., Nevakshenova, E., Nikonenko, V., & Grande, D. (2013). Ageing of ion-exchange membranes in electrodialysis: A structural and physicochemical investigation. *Journal of Membrane Science*, *436*, 68–78. https://doi.org/10.1016/j.memsci.2013.02.011

Goode, K. R., Asteriadou, K., Robbins, P. T., & Fryer, P. J. (2013). Fouling and Cleaning Studies in the Food and Beverage Industry Classified by Cleaning Type. *Comprehensive Reviews in FoodScience and Food Safety*, *12*, 121. https://doi.org/10.1111/1541-4337.12000

Guo, H., You, F., Yu, S., Li, L., & Zhao, D. (2015). Mechanisms of chemical cleaning of ion exchange membranes : A case study of plant-scale electrodialysis for oily wastewater treatment. *Journal of Membrane Science*, *496*, 310–317. https://doi.org/10.1016/j.memsci.2015.09.005

Iizuka, A., Hashimoto, K., Nagasawa, H., Kumagai, K., Yanagisawa, Y., & Yamasaki, A. (2012). Carbon dioxide recovery from carbonate solutions using bipolar membrane electrodialysis. *Separation and Purification Technology*, *101*, 49–59. https://doi.org/10.1016/j.seppur.2012.09.016

Kim, H., Shim, I., & Zhan, M. (2021). Chemical Enhanced Backwashing for Controlling Organic Fouling in Drinking Water Treatment Using a Novel Hollow-Fiber Polyacrylonitrile Nanofiltration Membrane. *Applied Sciences*, *11*.

Kram, T., Morita, T., Riahi, K., Roehrl, R. A., Van Rooijen, S., Sankovski, A., & De Vries, B. (2000). Global and regional greenhouse gas emissions scenarios. *Technological Forecasting and Social Change*, *63*(2–3), 335–371. https://doi.org/10.1016/S0040-1625(99)00113-4

La Plante, E. C., Simonetti, D. A., Wang, J., Al-Turki, A., Chen, X., Jassby, D., & Sant, G. N. (2021). Saline Water-Based Mineralization Pathway for Gigatonne-Scale CO2Management. *ACS Sustainable Chemistry and Engineering*, *9*(3), 1073–1089. https://doi.org/10.1021/acssuschemeng.0c08561

Li, Z., Yangali-quintanilla, V., Valladares-linares, R., Li, Q., Zhan, T., & Amy, G. (2011). Flux patterns and membrane fouling propensity during desalination of seawater by forward osmosis. *Water Research*, *46*(1), 195–204. https://doi.org/10.1016/j.watres.2011.10.051

Lide, D. R. (2000). *Handbook of Chemistry and Physics*. CRC Press.

Mercer, K. L., Lin, Y. P., & Singer, P. C. (2005). Enhancing calcium carbonate precipitation by heterogeneous nucleation during chemical softening. *Journal / American Water Works Association*, *97*(12). https://doi.org/10.1002/j.1551-8833.2005.tb07545.x

Mikhaylin, S., & Bazinet, L. (2016). Fouling on ion-exchange membranes: Classification, characterization and strategies of prevention and control. *Advances in Colloid and Interface Science*, *229*, 34–56. https://doi.org/10.1016/j.cis.2015.12.006

Moreno, J., de Hart, N., Saakes, M., & Nijmeijer, K. (2017). CO2 saturated water as two-phase flow for fouling control in reverse electrodialysis. *Water Research*, *125*, 23–31. https://doi.org/10.1016/j.watres.2017.08.015

Ngene, I. S., Lammertink, R. G. H., Kemperman, A. J. B., Ven, W. J. C. Van De, Wessels, L. P., Wessling, M., & Meer, W. G. J. Van Der. (2010). CO 2 Nucleation in Membrane Spacer Channels Remove Biofilms and Fouling Deposits. *Industrial & Engineering Chemistry Research*, *49*, 10034–10039.

Pärnamäe, R., Mareev, S., Nikonenko, V., Melnikov, S., Sheldeshov, N., Zabolotskii, V.,

Hamelers, H. V. M., & Tedesco, M. (2021). Bipolar membranes: A review on principles, latest developments, and applications. *Journal of Membrane Science*, *617*. https://doi.org/10.1016/j.memsci.2020.118538

Peng, Y., Ge, J., Li, Z., & Wang, S. (2015). Effects of anti-scaling and cleaning chemicals on membrane scale in direct contact membrane distillation process for RO brine concentrate. *Separation and Purification Technology*, *154*, 22–26. https://doi.org/10.1016/j.seppur.2015.09.007

Pintossi, D., Saakes, M., Borneman, Z., & Nijmeijer, K. (2019). Electrochemical impedance spectroscopy of a reverse electrodialysis stack: A new approach to monitoring fouling and cleaning. *Journal of Power Sources*, *444*, 227302. https://doi.org/10.1016/j.jpowsour.2019.227302

Porcelli, N., & Judd, S. (2010). *Chemical cleaning of potable water membranes : A review*. *71*, 137–143. https://doi.org/10.1016/j.seppur.2009.12.007

Psoch, C., & Schiewer, S. (2006). Anti-fouling application of air sparging and backflushing for MBR. *Journal of Membrane Science*, *283*(1–2), 273–280. https://doi.org/10.1016/j.memsci.2006.06.042

Rogelj, J., Den Elzen, M., Höhne, N., Fransen, T., Fekete, H., Winkler, H., Schaeffer, R., Sha, F., Riahi, K., & Meinshausen, M. (2016). Paris Agreement climate proposals need a boost to keep warming well below 2 °c. *Nature*, *534*(7609), 631–639. https://doi.org/10.1038/nature18307

Salinas, S. G., Schippers, J. C., Amy, G. L., Kim, I. S., & Kennedy, M. D. (2021). *Seawater Reverse Osmosis Desalination Assessment and Pre-treatment of Fouling and Scaling*. IWA Publishing.

Seran, E., Godefroy, M., Pili, E., Michielsen, N., & Bondiguel, S. (2017). What we can learn from measurements of air electric conductivity in222Rn-rich atmosphere. *Earth and Space Science*, *4*(2), 91–106. https://doi.org/10.1002/2016EA000241

Sharifian, R., Blommaert, M. A., Bremer, M., Wagterveld, R. M., & Vermaas, D. A. (2021b). Intrinsic bipolar membrane characteristics dominate the effects of flow orientation and external pH-profile on the membrane voltage. *Journal of Membrane Science*, *638*(April), 119686. https://doi.org/10.1016/j.memsci.2021.119686

Sharifian, R., Boer, L., Wagterveld, R. M., & Vermaas, D. A. (n.d.). *Oceanic carbon capture through electrochemically induced in situ carbonate mineralization using bipolar membrane*.

Sharifian, R., Wagterveld, R. M., Digdaya, I. A., Xiang, C., & Vermaas, D. A. (2021a). Electrochemical carbon dioxide capture to close the carbon cycle. *Energy & Environmental Science*. https://doi.org/10.1039/d0ee03382k

Son, Y. (2007). Determination of shear viscosity and shear rate from pressure drop and flow rate relationship in a rectangular channel. *Polymer*, *48*(2), 632–637. https://doi.org/10.1016/j.polymer.2006.11.048

Stumm, W., & Morgan, J. J. (1995). *Aquatic chemistry : Chemical equilibria and rates in natural waters* (third). John Wiley & Sons, Incorporated.

Sun, W., Jayaraman, S., Chen, W., Persson, K. A., & Ceder, G. (2015). Correction: Nucleation of metastable aragonite CaCO3in seawater (Proceedings of the National Academy of Sciences of the United States of America (2015), 112:3199-3204 (DOI: 10.1073/pnas.1423898112)). *Proceedings of the National Academy of Sciences of the United States of America*, *112*(20), E2735. https://doi.org/10.1073/pnas.1506100112

Tanzer, S. E., & Ramírez, A. (2019). When are negative emissions negative emissions? *Energy and Environmental Science*, *12*(4), 1210–1218. https://doi.org/10.1039/c8ee03338b

Teng, H., Masutani, S. M., Kinoshita, C. M., & Nihous, G. C. (1996). Solubility of CO2 in the ocean and its effect on CO2 dissolution. *Energy Conversion and Management*, *37*(6–8), 1029–1038. https://doi.org/10.1016/0196-8904(95)00294-4

Tong, T., Wallace, A. F., Zhao, S., & Wang, Z. (2019). Mineral scaling in membrane desalination : Mechanisms , mitigation strategies , and feasibility of scaling-resistant membranes. *Journal of Membrane Science*, *579*(February), 52–69. https://doi.org/10.1016/j.memsci.2019.02.049

United Nations. (2016). *The Paris Agreement*. FCCC/CP/2015/10/Add.1

Veerman, J., Saakes, M., Metz, S. J., & Harmsen, G. J. (2010). Reverse electrodialysis: Evaluation of suitable electrode systems. *Journal of Applied Electrochemistry*, *40*(8), 1461–1474. https://doi.org/10.1007/s10800-010-0124-8

Vermaas, D. A., Kunteng, D., Veerman, J., Saakes, M., & Nijmeijer, K. (2014a). Periodic feedwater reversal and air sparging as antifouling strategies in reverse electrodialysis. *Environmental Science and Technology*, *48*(5), 3065–3073. https://doi.org/10.1021/es4045456

Vermaas, D. A., Saakes, M., & Nijmeijer, K. (2014c). Early detection of preferential channeling in reverse electrodialysis. *Electrochimica Acta*, *117*, 9–17. https://doi.org/10.1016/j.electacta.2013.11.094

Vermaas, D. A., Saakes, M., & Nijmeijer, K. (2014b). Enhanced mixing in the diffusive boundary layer for energy generation in reverse electrodialysis. *Journal of Membrane Science*, *453*, 312–319. https://doi.org/10.1016/j.memsci.2013.11.005

Vermaas, D. A., Wiegman, S., & Smith, W. A. (2018). Ion transport mechanisms in bipolar membranes for (photo)electrochemical water splitting. *Sustainable Energy & Fuels*, *2*, 2006–2015. https://doi.org/10.1039/c8se00118a

Vital, B., Torres, E. V., Sleutels, T., Gagliano, M. C., Saakes, M., & Hamelers, H. V. M. (2021). Fouling fractionation in reverse electrodialysis with natural feed waters demonstrates dual media rapid filtration as an effective pre-treatment for fresh water. *Desalination*, *518*(August), 115277. https://doi.org/10.1016/j.desal.2021.115277

Vrouwenvelder, J. S., Graf von der Schulenburg, D. A., Kruithof, J. C., Johns, M. L., & van Loosdrecht, M. C. M. (2009). Biofouling of spiral-wound nanofiltration and reverse osmosis membranes: A feed spacer problem. *Water Research*, *43*(3), 583–594. https://doi.org/10.1016/j.watres.2008.11.019

Wagterveld, R. M. (2013). *PhD thesis: Effect of ultrasound on calcium carbonate crystallization*. Technische Universiteit Delft.

Wang, Q., Yang, P., & Cong, W. (2011). Cation-exchange membrane fouling and cleaning in bipolar membrane electrodialysis of industrial glutamate production wastewater. *Separation and Purification Technology*, *79*(1), 103–113. https://doi.org/10.1016/j.seppur.2011.03.024

Wei, Y., Nanayakkara, K. G. N., Herath, A. C., & Weerasooriya, R. (2021). Fouling of ion exchange membranes used in the electrodialysis reversal advanced water treatment : A review. *Chemosphere*, *263*, 127951. https://doi.org/10.1016/j.chemosphere.2020.127951

Wibisono, Y. (2014). *PhD thesis: Two-phase flow for fouling control in membranes*. University of Twente.

Willauer, H. D., DiMascio, F., Hardy, D. R., & Williams, F. W. (2017). Development of an Electrolytic Cation Exchange Module for the Simultaneous Extraction of Carbon Dioxide and Hydrogen Gas from Natural Seawater. *Energy and Fuels*, *31*(2), 1723–1730. https://doi.org/10.1021/acs.energyfuels.6b02586

Willems, P., Kemperman, A. J. B., Lammertink, R. G. H., Wessling, M., Annaland, M. V. S., Deen, N. G., Kuipers, J. A. M., & Meer, W. G. J. Van Der. (2009). Bubbles in spacers : Direct observation of bubble behavior in spacer filled membrane channels. *Journal OfMembrane Science*, *333*, 38–44. https://doi.org/10.1016/j.memsci.2009.01.040

Youn, M. H., Park, K. T., Lee, Y. H., Kang, S., Lee, S. M., & Kim, S. S. (2019). Carbon dioxide sequestration process for the cement industry. *Journal of CO2 Utilization*, *34*(April), 325–334. https://doi.org/10.1016/j.jcou.2019.07.023

Zhao, Y., Wang, J., Ji, Z., Liu, J., Guo, X., & Yuan, J. (2020). A novel technology of carbon dioxide adsorption and mineralization via seawater decalcification by bipolar membrane electrodialysis system with a crystallizer. *Chemical Engineering Journal*, *381*(8), 122542. https://doi.org/10.1016/j.cej.2019.122542

Zhong, S., & Mucci, A. (1993). Calcite precipitation in seawatre using a constant addtion technique. *Geochim. Cosmochim. Acta*, *57*, 1409–1417.

Appendix I – Determination of Ohmic resistance

Ohmic resistance is determined via the voltage-time curve. The voltage needed to overcome the Ohmic resistance is revealed when the applied current is interrupted (Figure *30*). By comparing these values before and after the experiment, the Ohmic resistance increase was determined.

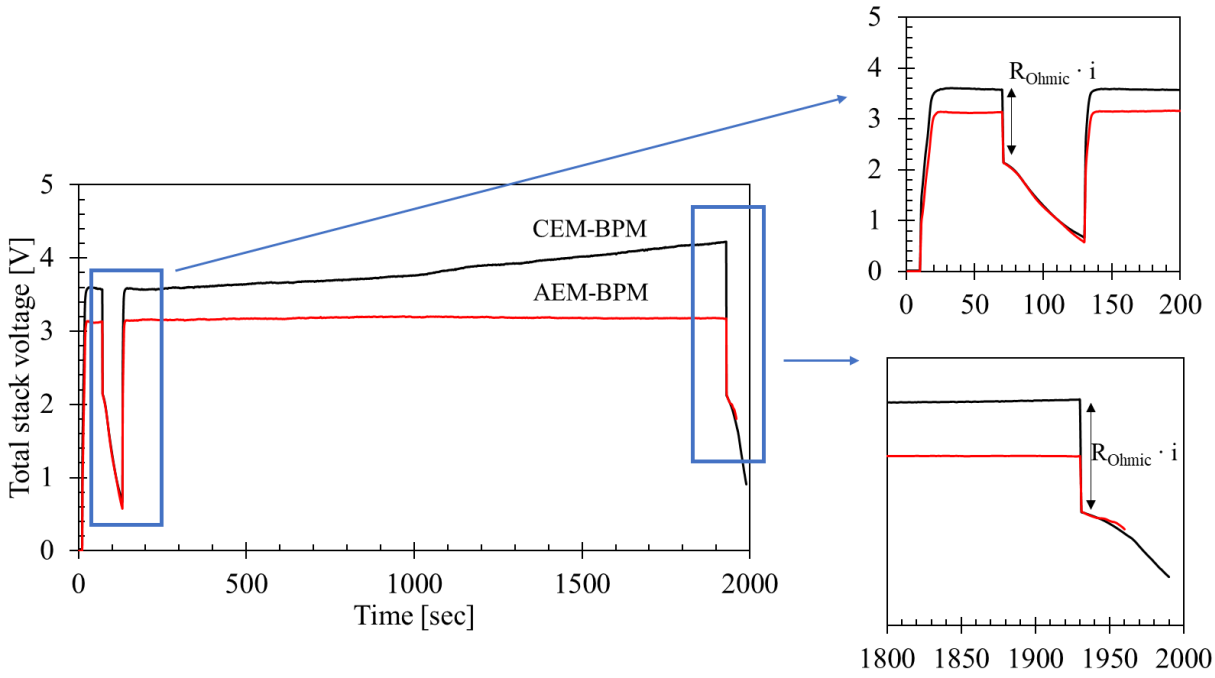

Figure 30, Ohmic resistance before and after a 30-minute experiment revealed via current interruption. These experiments were done for 72 mL·min^{-1} per compartment under 12.5 mA·cm^{-2} applied current density.

Figure 30 shows an example for one CEM-BPM and one AEM-BPM cell pair configuration. The Ohmic resistance was calculated using Ohms law, so R = V/I for the voltage drop marked with the arrow in Figure 30, the results for these two examples are *shown in Table 4.*

Table 4, Increase in Ohmic resistance for two 30 minutes experiment done for 72 mL·min^{-1} per compartment under 12.5 mA·cm^{-2} applied current density.

	AEM-BPM	CEM-BPM
R_{ohmic} before [Ω]	0.793	1.141
R_{ohmic} after [Ω]	0.827	1.675
Δ R_{ohmic} [Ω]	0.0343	0.534

Ohmic resistance for all 32 experiments was determined using this method.

Appendix II – Titration for DIC Concentration Approximation

The method for titration for DIC concentration approximation was taken from the master thesis of Lieneke Boer (Boer, 2020).

With use of titration with HCl, the carbonate concentration in (synthetic) seawater can be determined. The acid addition between the pKa and the equivalence point, which are determined to be respectively 6.1 and 7.7 in Visual MINTEQ 3.1 simulations, is equal to halve of the DIC present in the sample. The following steps were taken to estimate the DIC concentration in feed and outlet samples:

1. Filter 50 mL (synthetic) seawater sample through a filter with a pore size of 0.22 µm

2. Measure the pH

3. Add a set amount of 0.1M HCl (25 µL, 50 µL, 100 µL) to the sample and measure the pH

4. Repeat step 3 until a pH below 6.1 is reached

5. Determine the acid addition between a pH = 7.7 and pH = 6.1

6. Calculate the DIC concentration ($mol \cdot L^{-1}$) based on the determined acid addition, considering that between pH = 7.7 and pH = 6.1 halve of the DIC is converted from HCO_3^- to H_2CO_3, and that converting 1 mol HCO_3^- into 1 mol H_2CO_3 consumes 1 mol of H^+.

Appendix III – AEM-BPM cell pair configuration

The schematic picture of the BPMED AEM-BPM cell pair design for the inorganic fouling control experiments is shown in Figure 31.

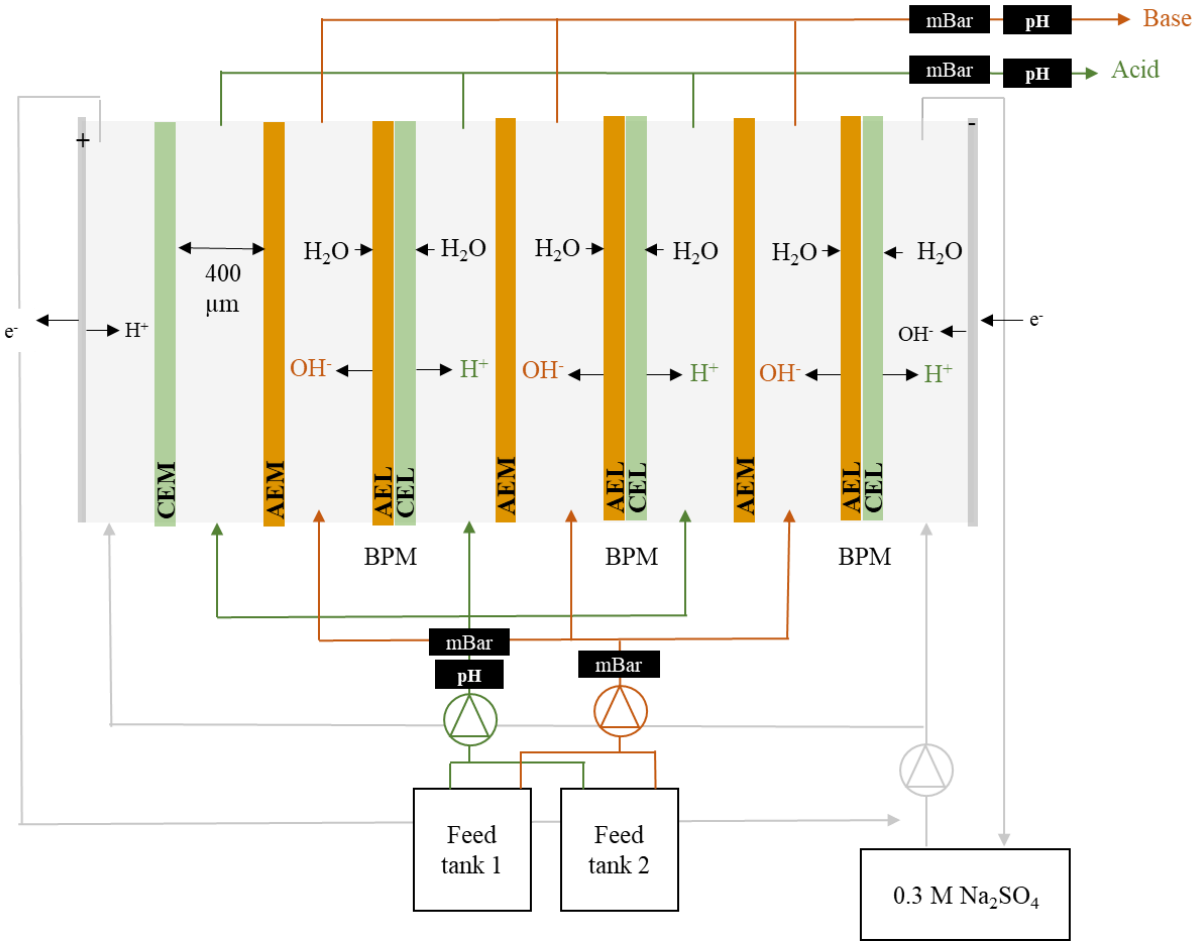

Figure 31, schematic representation of the BPMED AEM-BPM cell configuration with a CEM shielding membrane. The with of the channels is 400 µm, using Integrated gasket-spacers provided by Aqua Battery B.V. .

Appendix IV – Inorganic fouling removal cell design

The cell design used for the inorganic fouling removal.

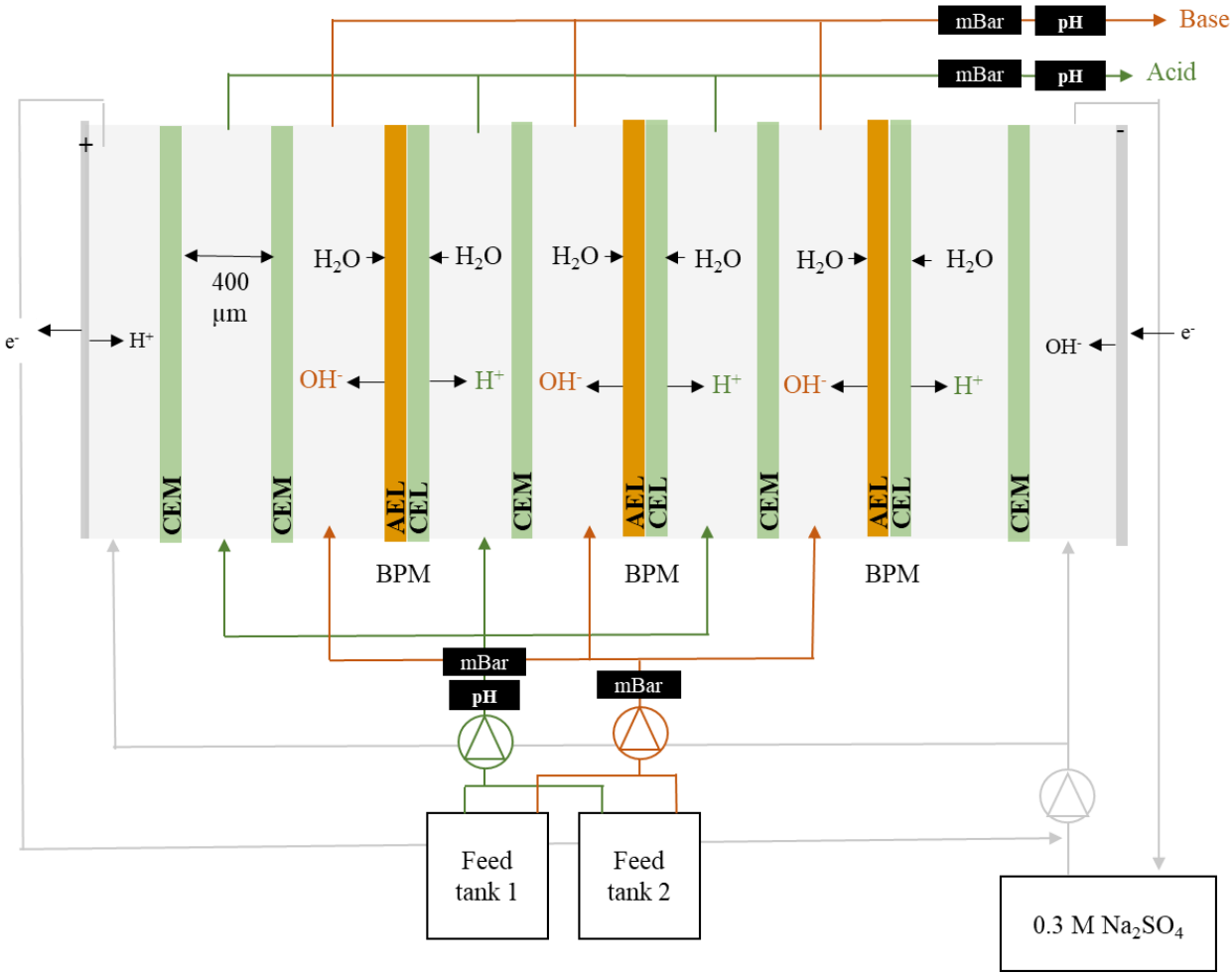

Figure 32, , schematic representation of the BPMED CEM-BPM cell configuration with 2 CEM shielding membranes. The with of the channels is 400 µm, using Integrated gasket-spacers provided by Aqua Battery B.V. .

Appendix V – Interval determination

The BPMED cell run for 30 minutes for 2 flowrates and 4 different current density's for a BPMED cell design as shown in *Appendix IV – Inorganic fouling removal cell* design, Figure 32. A current density of 5, 10, 12.5 and 15 mA·cm^{-2} was applied for a flowrate of 24 and 72 mL·min^{-1}·compartment^{-1}. For the inorganic fouling removal experiment parameter settings were chosen under which there was '*pushed for inorganic fouling*. The aim was to find an inorganic fouling build-up not so severe that inorganic fouling clogged the system, but enough that inorganic fouling removal experiments could be done within a reasonable time frame. When choosing the flowrate, applied current density and inorganic fouling removal interval the chose was made base the interval on ~5% increase of the total stack voltage and pressure drop.

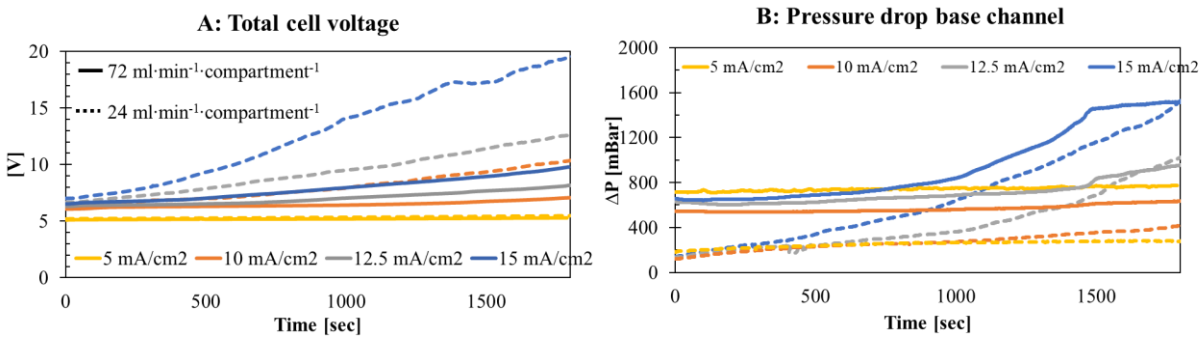

Figure 33, (A) total cell voltage and (B) pressure drop over the base compartments for experiments with an CEM-BPM configuration.

The data from Figure *33* was transformed to percentual increase to determine after how long an 5% increase of voltage or pressure drop was shown. Results are shown in Figure *34*.

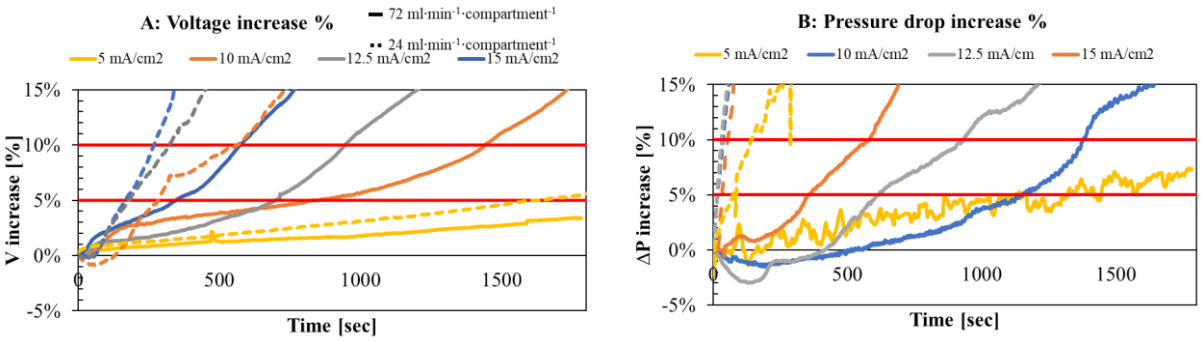

Figure 34, (A) total cell voltage increase in % and (B) pressure drop over the base compartment in %. Red lines were used to determine after how long 5% and 10% increase was reached.

It was determined that for 72 mL·min^{-1} per compartment and 12.5 mA·cm^{-2} , 5% voltage and pressure drop increase was reached after ~600 seconds. Based on these results, the choice was made to apply the inorganic fouling removal methods every 10 minutes.

Appendix VI – Average values synthetic seawater

A total of 7 'batches' of 400 L synthetic seawater were made and used. Average measurement concentrations of cation, DIC, conductivity and pH with the standard error of the mean. The aim conductivity for this synthetic seawater was determined in Visual MINTEQ 3.1 by (Boer, 2020)

Average	Aimed (mM)	Measured (mM)	STD error (mM)
Na^+	459	446	6.21
K^+	9.72	10.1	0.431
Ca^{2+}	10	10.3	0.138
Mg^{2+}	51.9	52.7	0.637
DIC	2.1-2.3	2.24	0.046

	Aimed (mS·cm^{-1})	Measured (mS·cm^{-1})	STD error (mS·cm^{-1})
Tank 1	76	75.7	0.437
Tank 2	22.1	22.1	0.148

	Aimed	Measured	STD error
pH *	7.9	7.8	0.013

***The error of the pH meters was +/- 0.2**

The average and standard error of the mean was calculate using (Barde & Barde, 2012):

$$\sigma_{mean} = \frac{s}{\sqrt{n}} \qquad \text{Equation 20}$$

σ_{mean} = standard error of the mean; s = standard deviation ; n = sample size.

The standard deviation was determined using excel, and has the following equation (Barde & Barde, 2012):

$$s = \sqrt{\frac{\sum(X - \overline{X})^2}{n - 1}} \qquad \text{Equation 21}$$

s = standard deviation; X = individual value; X = sample mean; n = sample size.

Appendix VII – Theoretical total stack voltage

The total stack voltage was calculated. The voltage of the electrode rinsing solution compartments (where water redox was used) was measured with reference electrodes and was therefore not influenced in these calculations. The following equation was used for the voltage to overcome Ohmic resistance:

$$V = I \cdot R \qquad \text{Equation 22}$$

$$R_{electrolyte} = \frac{1}{\sigma} \cdot \frac{l}{A} \qquad \text{Equation 23}$$

Symbol	unit	Description	Value
l	m	length, distance between membranes	0.0004
A	m^2	Membrane surface	0.01
σ	$S \cdot m^{-1}$	Conductivity, Resistivity, and conductivity are reciprocals	-
R	Ω	Resistance	-
V	voltage	power	-
I	A	Current of $C \cdot s^{-1}$	0.5 – 1.5

$R_{membranes}$ was provided by the supplier (Fumatech B.V.). The initial total stack voltage is the same for both configurations and flowrates.

Given membrane values	Value	unit	Per membrane
Resistance AEM/CEM	4	$\Omega \cdot cm^2$	0.04
Resistance BPM	8	$\Omega \cdot cm^2$	0.08
Water dis. BPM	0.83	V per BMP*	

* $0.059 \cdot \Delta pH = 0.83$ for $\Delta pH=14$ but in practice the measured voltage is ~0.83-1 V for all ranges as a consequence of extreme pH near the membranes surface (Vermaas et al., 2018).

Resistance between membranes	value	unit
σ seawater	5**	$S \cdot m^{-1}$
l	0.0004	m
A	0.01	m^2
Resistance seawater	0.008	Ω

** https://www.lenntech.com/composition-seawater.htm

Total V	n	*i* = 0.5 A	*i* = 1.0 A	*i* = 1.25 A	*i* = 1.5 A
Between membranes	6	0.024 V	0.048 V	0.06 V	0.072 V
CEM/AEM	4	0.08 V	0.16 V	0.2 V	0.24 V
BPM	3	2.61 V	2.73 V	2.79 V	2.85 V
Total stack voltage (V)		**2.7**	**2.9**	**3.1**	**3.2**

Example for i = 0.5 A:

$$V_{total\ stack} = V_{compartments} + V_{CEM/AEM} + V_{BPM}$$

$$V_{compartment} = 6 \cdot 0.008 \cdot 0.5 = 0.024\ V$$

$$V_{CEM/AEM} = 4 \cdot 0.04 \cdot 0.5 = 0.08\ V$$

$$V_{BPM} = 3 \cdot (0.08 \cdot 0.5 + 0.83) = 2.61\ V$$

$$V_{total\ stack} = 0.024 + 0.08 + 2.61 = 2.7\ V$$

The results for 24 mL·min^{-1} per compartment:

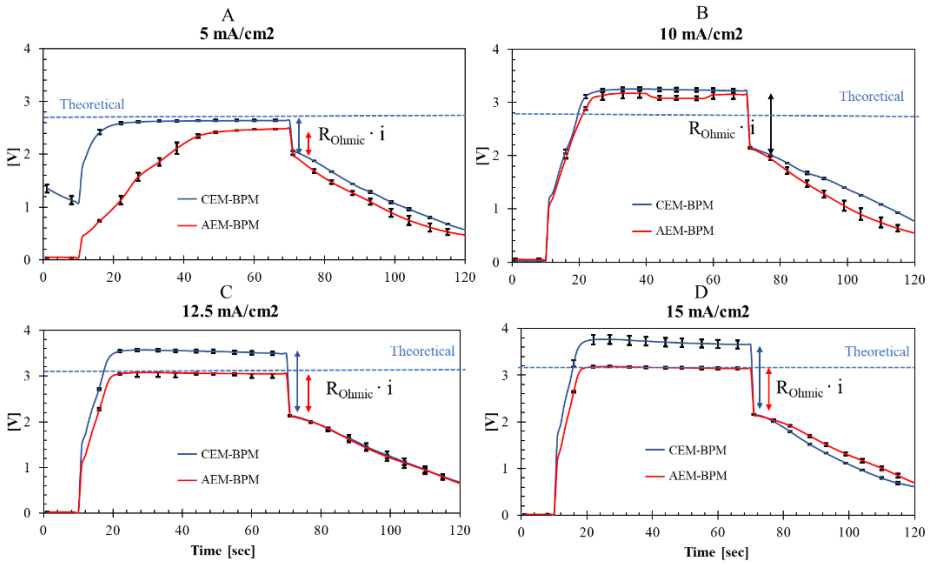

Figure 35, measured vs theoretical total stack voltage before an experiment for 24 mL·min^{-1} per compartment. These V-t graphs are the average voltage curve of 2 repetitions incl. the standard error between the repetition (when error bars are not visible, they are smaller than the line width). Graphs are shown for current densities of 5 (a), 10 (b), 12.5 (c) and 15 (d) mA·cm^{-2}.

The measured total stack voltage before an experiment is similar as for (Figure 11), as was expected. An exception is the total stack voltage for AEM-BPM for 10 mA·cm^{-2} (Figure *35*B), which is similar as for CEM-BPM, but for 72 mL·min^{-1} per compartment close to the theoretical value. For one experiment for AEM-BPM for 10 mA·cm^{-2} and 24 mL·min^{-1} per compartment, demi water recirculated instead of electrode rinsing solution during the first 5 minutes, explaining the higher voltage average (as the resistance of demi water is higher than for the electrode rinsing solution). The standard error of the mean was calculated as shown in *Appendix VI – Average values synthetic seawater*.

Appendix VIII – Pressure drop increase base channel (%)

Pressure drop increase for both cell pair configuration, flowrates and all applied current density values are shown in Figure 36.

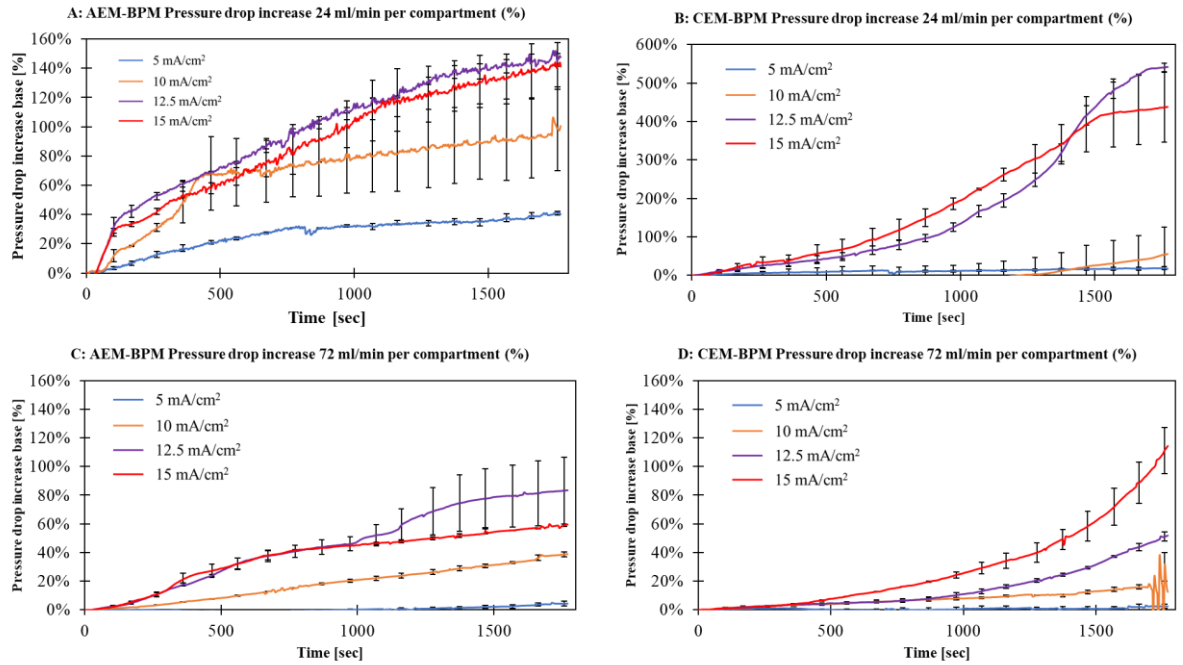

Figure 36 (A) shows the pressure drop increase in the base channel [%] for the AEM-BPM configuration for the 24 mL·min^{-1} per compartment and (C) for the 72 mL·min^{-1} per compartment. (B) Shows the pressure drop increase in the base channel [%} for the CEM-BPM configuration for 24 mL·min^{-1} per compartment and (D) for 72 mL·min^{-1} per compartment. For A-D, the curves show the average of two repetitions with the error bars showing the standard error values between the two repetitions. Pressure drop increase is relative to the pressure drop at t=0 seconds

Figure 36 shows the pressure drop increase for the base compartments. Percentual increase is calculated as followed:

$$Pressure\ drop\ increase\ (\%) = \frac{(\Delta P_{t=t} - \Delta P_{t=0})}{\Delta P_{t=0}} \qquad \text{Equation 24}$$

$\Delta P_{t=0}$ is the pressure drop at the moment that the current is turned on.

The standard error of the mean was calculated as shown in *Appendix VI – Average values synthetic seawater*.

Appendix IX – pH and DIC, Ca^{2+}, Mg^{2+} removal

The measured pH and simulation pH values (with Visual MINTEQ 3.1) are shown below. The input for the simulated for OH^- in $mol \cdot L^{-1}$ was calculated based on Equation 11, but encountered for the limiting current density and cell retention time:

$$[OH^-_{produced}] = \frac{(i - i_{lim})}{F}\left(\frac{t_r}{d}\right) \qquad \text{Equation 25}$$

In which i is the current density in $A \cdot cm^{-2}$, i_{lim} the limiting current density (0.0025 $A \cdot cm^{-2}$), F the Faraday constant 96485 ($C \cdot mol^{-1}$), t_r the cell retention time in seconds and d the compartment thickness (0.04 cm).

pH values AEM-BPM 24 mL·min^{-1} per comp. (t_r =10)

	Average	Lowest value	Highest value	*Simulation value*	*Simulation value after precipitation*
5 mA·cm^{-2}	9.90	9.75	10.15	*10.9*	*9.626*
10 mA·cm^{-2}	10.29	10.15	10.35	*11.6*	*9.656*
12.5 mA·cm^{-2}	10.24	9.65	10.35	*11.7*	*9.672*
15 mA·cm^{-2}	10.31	10.15	10.40	*11.9*	*9.69*

	Average	Lowest value	Highest value	*Simulation value*
5 mA·cm^{-2}	2.48	2.40	2.70	*2.608*
10 mA·cm^{-2}	1.90	1.85	2.20	*1.986*
12.5 mA·cm^{-2}	1.82	1.80	1.90	*1.843*
15 mA·cm^{-2}	1.72	1.70	1.75	*1.734*

pH values AEM-BPM 72 mL·min^{-1}·per comp. (t_r =3.33)

	Average	Lowest value	Highest value	*Simulation value*	*Simulation value after precipitation*
5 mA·cm^{-2}	9.34	9.30	9.40	*9.9*	*9.501*
10 mA·cm^{-2}	9.79	9.60	9.95	*10.9*	*9.626*
12.5 mA·cm^{-2}	9.94	9.65	10.15	*11.1*	*9.631*
15 mA·cm^{-2}	9.91	9.65	10.15	*11.2*	*9.635*

	Average	Lowest value	Highest value	*Simulation value*
5 mA·cm^{-2}	4.80	4.60	4.90	*4.971*
10 mA·cm^{-2}	2.59	2.55	2.60	*2.608*
12.5 mA·cm^{-2}	2.51	2.45	2.55	*2.426*
15 mA·cm^{-2}	2.37	2.35	2.45	*2.297*

CEM-BPM 24 mL·min^{-1} per comp. (t_r =10)

	Average	Lowest value	Highest value	*Simulation value*	*Simulation value after precipitation*
5 mA·cm^{-2}	9.77	0.12	0.13	*10.9*	*9.626*
10 mA·cm^{-2}	9.84	0.74	0.51	*11.6*	*9.656*
12.5 mA·cm^{-2}	10.21	0.66	0.14	*11.7*	*9.672*
15 mA·cm^{-2}	10.23	0.33	0.07	*11.9*	*9.69*

	Average	Lowest value	Highest value	*Simulation value*
5 mA·cm^{-2}	2.32	0.02	0.08	*2.608*
10 mA·cm^{-2}	1.90	0.00	0.00	*1.986*
12.5 mA·cm^{-2}	1.94	0.14	1.91	*1.843*
15 mA·cm^{-2}	1.81	0.11	0.14	*1.734*

CEM-BPM 72 mL·min^{-1} per comp. (t_r =3.33)

	Average	Lowest value	Highest value	*Simulation value*	*Simulation value after precipitation*
5 mA·cm^{-2}	9.45	9.40	9.50	*9.9*	*9.501*
10 mA·cm^{-2}	9.75	9.65	10.00	*10.9*	*9.626*
12.5 mA·cm^{-2}	9.87	9.70	10.10	*11.1*	*9.631*
15 mA·cm^{-2}	10.00	9.65	10.40	*11.2*	*9.635*

	Average	Lowest value	Highest value	*Simulation value*
5 mA·cm^{-2}	4.21	3.95	4.95	*4.971*
10 mA·cm^{-2}	2.60	2.60	2.70	*2.608*
12.5 mA·cm^{-2}	2.44	2.40	2.45	*2.426*
15 mA·cm^{-2}	2.30	2.30	2.55	*2.297*

	5 mA/cm2			10 mA/cm2			12.5 mA/cm2			15 mA/cm2		
	DIC removal	Ca^{2+} removal	Mg^{2+} removal	DIC removal	Ca^{2+} removal	Mg^{2+} removal	DIC removal	Ca^{2+} removal	Mg^{2+} removal	DIC removal	Ca^{2+} removal	Mg^{2+} removal
AEM-BPM 24 ml/min/comp.												
Average	1.58	1.37	1.66	1.30	1.08	7.11	1.82	1.46	8.06	1.64	1.54	11.74
std error	0.12	0.15	0.19	0.01	0.04	0.23	0.04	0.02	0.32	0.03	0.02	0.71
Simulation	2.03	2.08	2.13	2.03	2.08	8.61	2.03	2.08	11.85	2.03	2.08	15.09
AEM-BPM 72 ml/min/comp.												
Average	0.51	0.69	0.79	1.43	1.72	3.22	1.34	1.50	2.62	1.46	1.35	2.30
std error	0.05	0.12	0.45	0.04	0.01	0.25	0.05	0.04	0.35	0.00	0.19	0.35
Simulation	2.03	2.08	0.00	2.03	2.08	2.13	2.03	2.08	3.21	2.03	2.08	4.29
CEM-BPM 24 ml/min/comp.												
Average	1.36	1.05	2.51	1.65	1.63	8.06	1.64	1.66	10.80	1.21	1.45	11.91
std error	0.00	0.02	0.12	0.09	0.04	0.52	0.08	0.03	0.89	0.07	0.58	2.34
Simulation	2.03	2.08	0.00	2.03	2.08	0.00	2.03	2.08	0.00	2.03	2.08	0.00
CEM-BPM 72 ml/min/comp.												
Average	0.37	0.41	1.28	1.53	1.26	1.42	1.79	1.37	1.03	1.76	1.61	3.02
std error	0.04	0.01	0.03	0.02	0.04	0.25	0.03	0.02	0.06	0.01	0.22	1.03
Simulation	2.03	2.08	0.00	2.03	2.08	0.00	2.03	2.08	0.00	2.03	2.08	0.00

Figure 37, all values for DIC, Ca^{2+} and Mg^{2+} removal in mM, both the measured and the simulated values.

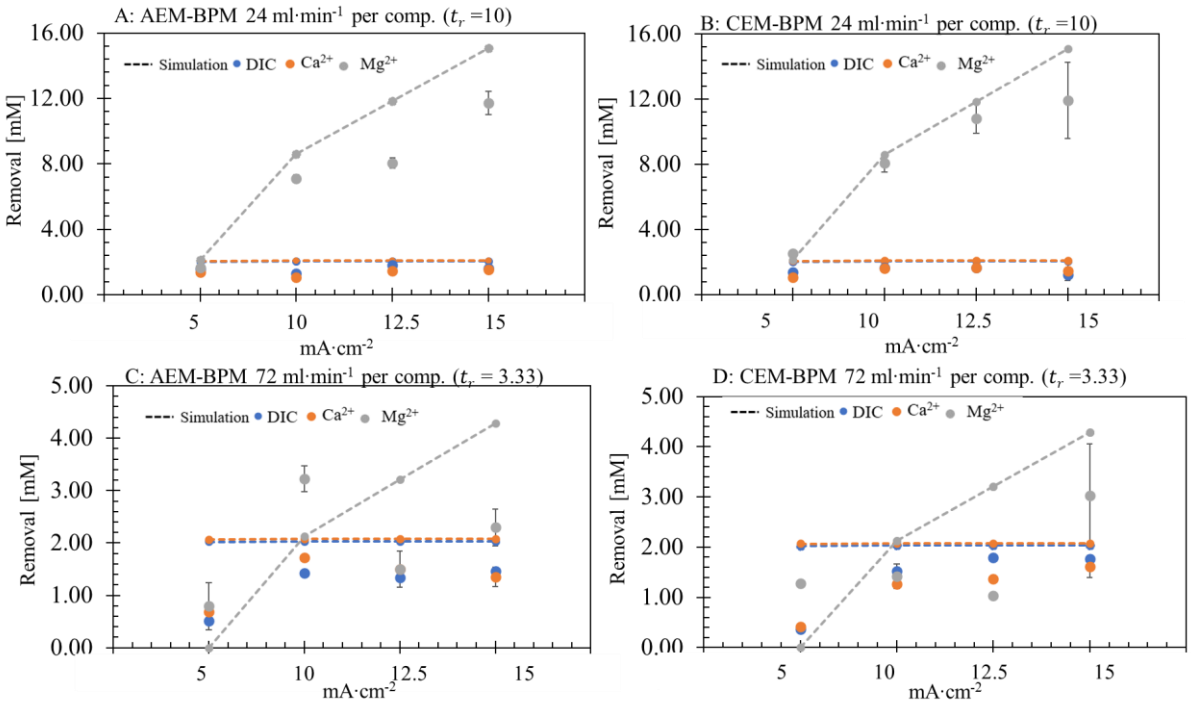

Figure 38, A-D: DIC and Mg^{2+} and Ca^{2+} removal for both cell pair configurations, cell residence times (t_r) and applied current densities. The removal according to the Visual MINTEQ 3.1 simulations are shown with the dotted line. The concentrations in the feed were ~2.1-2.4 mM, 10 mM., 50 mM for DIC, Ca^{2+} and Mg^{2+}, respectively. The DIC and Ca^{2+} and Mg^{2+} removal values are the average of 2 repetitions, and the standard error is included, however most bars are not visible under the markers as the values are small.

The standard error of the mean was calculated as shown in *Appendix VI – Average values synthetic seawater*.

Appendix X – Energy consumption

In this appendix, one example is shown of how energy consumption was calculated for each experiment. The equation from theory was used (Equation 17):

$$E = \frac{\int_0^t V\, I\, dt}{m_{DIC}} + \frac{\int_0^t (\Delta P_a + \Delta P_b)\, q\, dt}{m_{DIC}} \qquad \text{Equation 17}$$

In which V represents the total cell voltage (V), I the applied current density (A), integrated over the running time of the experiments in seconds. The second part of the equation describes the pumping energy. In which ΔP_a and ΔP_b are respectively the pressure drop over the acid- and base compartments (in Pa) and q the flowrate ($m^3 \cdot s^{-1}$), integrated over time. The values are divided by amount of moles $CaCO_3$ in the chosen time scale (m_{DIC} in moles DIC).

The example is for reference experiment (no cleaning), with 12.5 $mA \cdot cm^{-2}$ applied current density and 72 $mL \cdot min^{-1}$ per compartment and a duration of 60 minutes. To get the *electrical energy* the current is multiplied with the voltage. This must be integrated over time, but since the voltage in different each second, $i \cdot V$ is done for every second and then summed up at the end. Data from the first and last seconds incl. the value for $i \cdot V$ are shown below:

Date	time	A	V	I·V [Joule]
03.06.2021	09:52:18	1.25	4.0	5.0
03.06.2021	09:52:19	1.25	4.4	5.5
03.06.2021	09:52:20	1.25	4.8	6.0
03.06.2021	09:52:21	1.25	5.2	6.5
03.06.2021	09:52:22	1.25	5.5	6.9
03.06.2021	09:52:23	1.25	5.8	7.2
03.06.2021	09:52:24	1.25	6.1	7.7
03.06.2021	09:52:25	1.25	6.3	7.9
03.06.2021	09:52:26	1.25	6.4	8.0
03.06.2021	09:52:27	1.25	6.4	8.1
03.06.2021	09:52:28	1.25	6.5	8.1

Last seconds, about an hour later as this experiment lasted 60 minutes, including the sum for $i \cdot V$:

03.06.2021	10:51:52	1.25	12.4	15.6
03.06.2021	10:51:53	1.25	12.5	15.6
03.06.2021	10:51:54	1.25	12.5	15.6
03.06.2021	10:51:55	1.25	12.5	15.6
03.06.2021	10:51:56	1.25	12.5	15.6
03.06.2021	10:51:57	1.25	12.5	15.6

03.06.2021	10:51:58	1.25	12.5	15.6
03.06.2021	10:51:59	1.25	12.5	15.6
03.06.2021	10:52:00	1.25	12.5	15.6
03.06.2021	10:52:01	1.25	12.5	15.6
03.06.2021	10:52:02	1.25	12.5	15.6
03.06.2021	10:52:03	1.25	12.5	15.6
03.06.2021	10:52:04	1.25	12.5	15.6
03.06.2021	10:52:05	1.25	12.5	15.6
03.06.2021	10:52:06	1.25	12.5	15.6
03.06.2021	10:52:07	1.25	12.5	15.6
03.06.2021	10:52:08	1.25	12.5	15.6
03.06.2021	10:52:09	1.25	12.5	15.6
03.06.2021	10:52:10	1.25	12.5	15.7
03.06.2021	10:52:11	1.25	12.5	15.7
03.06.2021	10:52:12	1.25	12.5	15.7
03.06.2021	10:52:13	1.25	12.5	15.7
03.06.2021	10:52:14	1.25	12.5	15.7
03.06.2021	10:52:15	1.25	12.5	15.7
03.06.2021	10:52:16	1.25	12.5	15.7
				41428
			sum	**Joule**

To get the *pump energy* the pressure drop is multiplied with the flowrate. 72 $mL \cdot min^{-1}$ per compartment is $(72/60) \cdot 10^{-6} = 1.2 \cdot 10^{-6}\ m^3 \cdot s^{-1}$ which for 3 compartment is $3.6 \cdot 10^{-6}\ m^3 \cdot s^{-1}$. The value of the pressure drop in mbar is multiplied by 100 to get to pascal. The pressure drop in pascal is multiplies by $3.6 \cdot 10^{-6}\ m^3 \cdot s^{-1}$ for the acid and the base. Again, this is calculated for each second (as $\Delta P \cdot q$ is in $joule \cdot s^{-1}$, imagine each value is multiplied by 1 second to get to joule), and summed up at the end.

Date	time	mbar Base	$\Delta P_{base} \cdot q_{base}$ [Watt] = $joule \cdot s^{-1}$	mbar Acid	$\Delta P_{base} \cdot q_{base}$ [Watt] = $joule \cdot s^{-1}$
03.06.2021	09:52:18	619	0.223	422.8	0.152
03.06.2021	09:52:19	619	0.223	422.7	0.152
03.06.2021	09:52:20	619	0.223	422.6	0.152
03.06.2021	09:52:21	619	0.223	422.6	0.152
03.06.2021	09:52:22	620	0.223	422.6	0.152
03.06.2021	09:52:23	620	0.223	422.7	0.152
03.06.2021	09:52:24	620	0.223	422.7	0.152
03.06.2021	09:52:25	620	0.223	422.6	0.152
03.06.2021	09:52:26	620	0.223	422.6	0.152
03.06.2021	09:52:27	621	0.223	422.7	0.152
03.06.2021	09:52:28	621	0.224	422.7	0.152
03.06.2021	09:52:29	621	0.224	422.8	0.152
03.06.2021	09:52:30	622	0.224	422.8	0.152
03.06.2021	09:52:31	622	0.224	422.8	0.152

03.06.2021	09:52:32	622	0.224	422.8	0.152
03.06.2021	09:52:33	622	0.224	422.8	0.152
03.06.2021	09:52:34	622	0.224	422.8	0.152
03.06.2021	09:52:35	623	0.224	422.8	0.152
03.06.2021	09:52:36	623	0.224	422.8	0.152
03.06.2021	09:52:37	623	0.224	422.8	0.152
03.06.2021	09:52:38	623	0.224	422.8	0.152
03.06.2021	09:52:39	624	0.225	422.9	0.152

Last seconds, about an hour later as this experiment lasted 60 minutes, including the sum for pressure drop:

03.06.2021	10:51:52	3082	1.109	484.1	0.174
03.06.2021	10:51:53	3082	1.110	484.1	0.174
03.06.2021	10:51:54	3081	1.109	484	0.174
03.06.2021	10:51:55	3089	1.112	484	0.174
03.06.2021	10:51:56	3090	1.112	484	0.174
03.06.2021	10:51:57	3084	1.110	484	0.174
03.06.2021	10:51:58	3087	1.111	484	0.174
03.06.2021	10:51:59	3089	1.112	484.1	0.174
03.06.2021	10:52:00	3082	1.109	484.1	0.174
03.06.2021	10:52:01	3079	1.109	484.2	0.174
03.06.2021	10:52:02	3086	1.111	484.4	0.174
03.06.2021	10:52:03	3085	1.110	484.5	0.174
03.06.2021	10:52:04	3082	1.109	484.6	0.174
03.06.2021	10:52:05	3086	1.111	484.8	0.175
03.06.2021	10:52:06	3087	1.111	485	0.175
03.06.2021	10:52:07	3083	1.110	485	0.175
03.06.2021	10:52:08	3084	1.110	485	0.175
03.06.2021	10:52:09	3086	1.111	485	0.175
03.06.2021	10:52:10	3081	1.109	484.8	0.175
03.06.2021	10:52:11	3080	1.109	484.8	0.175
03.06.2021	10:52:12	3086	1.111	484.8	0.175
03.06.2021	10:52:13	3087	1.111	484.7	0.174
03.06.2021	10:52:14	3087	1.111	484.7	0.174
03.06.2021	10:52:15	3090	1.113	484.8	0.175
03.06.2021	10:52:16	3091	1.113	484.9	0.175
			1762	Joule	540 Joule

The pumping energy for the base compartment ended higher than for the acid compartment, as expected since no inorganic fouling was assumed in the acid compartments. The electrical energy consumption is now 41.31 kJ and for pumping energy 2.33 kJ so 43.76 kJ in total for 1 hour. This needs to be divided by the amount of mole carbonate (DIC) removed in this hour,

which for this experiment was 0.0223 mole Table 5,. The energy consumption of this experiment was 43.76 kJ/0.0223 mole = 1963 kJ/mole $CaCO_3$

Table 5, DIC removal per hour, electrical and pumping energy consumed in 1 hour, and the energy consumption.

DIC removal	1.72	**mM**	**Electrical**	41.43	**kJ**
Base outlet per hour	12.96	**L per hour**	**Pumping**	2.33	**kJ**
	0.0223	**Mole per hour**	**Total**	**1963**	**kJ/mole $CaCO_3$**

If the energy consumption is an average of 2 repetitions, the standard error was calculated as shown in Appendix VI – Average values synthetic seawater, for the value of total energy consumption.

To calculate the price per mole H^+ the total energy consumption per hour (43.76 kJ/hour) was divided by the amounts of mole H^+ produced in one hour, which was calculated using Equation 25 and was 0.0086 mole/L · 12.96 L = 0.11 mole H^+/hour. This gives an energy consumption of 394 kJ/mole H+ or 394·0.00027777 = 0.11 kWh/mole H+. Assuming a price of 24 cents/kWh (https://www.consumentenbond.nl/energie-vergelijken/kwh-prijs), this results in 2.66 cent/ mole H^+ for this example. For an applied current density of 5-10 mA·cm^{-2} and 72 mL·min^{-1} per compartment, the values are given in Table 6.

Table 6, Price per mole H+ produced by the BPMED system for 5-10 mA·cm^{-2} and 72 mL·min^{-1} per compartment.

Applied current density	**Average energy consumption (kJ/h)**	**H+ produced (moles/ hour)**	**Average energy consumption (kJ/mole)**	**Average energy consumption (kWh/ mole)**	**Price (cents /mole)**
5 mA·cm^{-2}	5.62	0.028	201	0.056	1.34
10 mA·cm^{-2}	11.8	0.084	141	0.039	0.94

Appendix XI - Pressure drop and voltage increase (%) relative to the reference experiment

In this appendix, one example is shown of how raw data is transformed to percentual increase, and percentual increase curves are transformed to curves for increase (%) relative to the reference experiment. Figure *39* shows pressure drop over the base compartments for 2 bar, 4 bar and a reference experiment for 72 mL·min^{-1} per compartment, 12.5 mA·cm^{-2} and an CEM-BPM configuration. Pressure drop increase was calculated using Equation 24:

$$Pressure\ drop\ increase\ (\%) = \frac{(\Delta P_{t=t} - \Delta P_{t=0})}{\Delta P_{t=0}} \qquad \text{Equation 24:}$$

$\Delta P_{t=0}$ is the pressure drop at the moment that the current is turned on. Doing this for each value of t , and for the reference, 2 bar and 3 bar, this will result in Figure *40*.

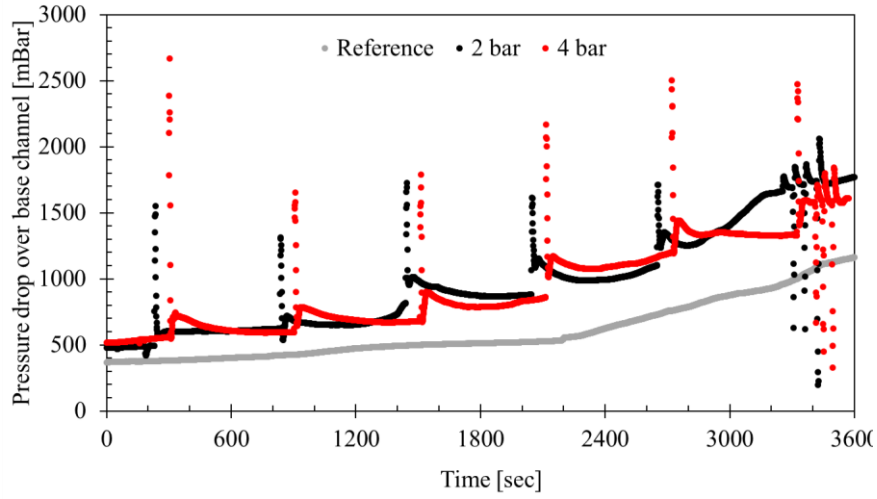

Figure 39, pressure drop over the base compartment vs time.

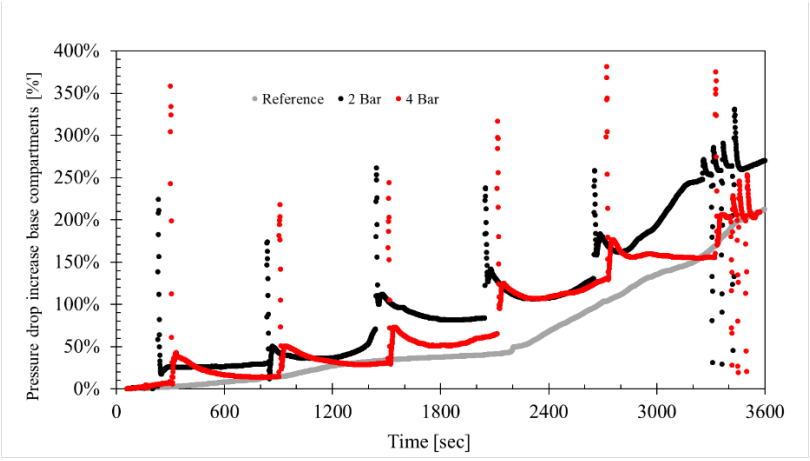

Figure 40, Pressure drop increase in the base compartments (%) for 2 and 4 bar. The grey line represents a reference experiment (no inorganic fouling removal method).

Figure 41 was made as followed: at t = 600, the reference experiment showed an increase of 9.32%. The 2 bar experiment at t = 600 increased 27.2% and the 4 bar experiment at t = 600 increased 15.2 %.

2 bar increased: 27.2% - 9.32% =17.9% more than the reference, or 17.9% increase relative to the reference. So, at x = 600, y = 17.9% for 2 bar in Figure 41.

4 bar increased: 15.2% - 9.31% = 5.89 % more than the reference, or 5.89% increase relative to the reference. So, at x = 600, y = 5.89 % for 4 bar in Figure 41.

This methods were used for every value of t, resulting in Figure *41*.

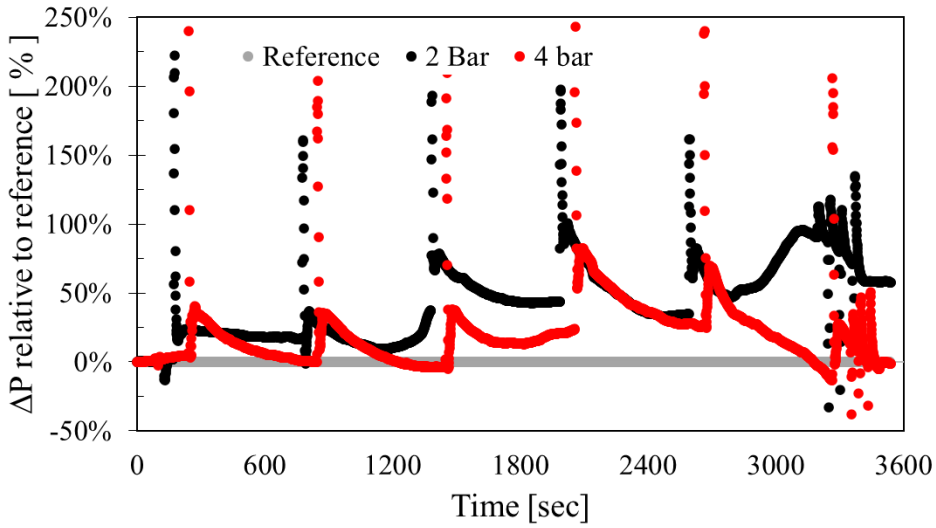

Figure 41, Pressure drop increase (%) relative to the reference experiment for the experiment shown in Figure 40.

The figures shown in sections*: 4.2.1.1 Air sparging, 4.2.242Back pressure and 4.2.3 Temporary flowrate increase* are an average of 2 or 3 figures as Figure *41*. The standard error of the mean was calculated as shown in *Appendix VI – Average values synthetic seawater*.

The curves for voltage increase relative to the reference was made similar, with one modification:

$$Voltage\ increase\ (\%) = \frac{(V_{t=t} - V_{t=120})}{V_{t=120}} \qquad \textbf{Equation 26}$$

The percentual increase is relative to the voltage at t = 120 (120 seconds after the current was turned on), because the voltage takes some time to stabilize once the current is turned on.

Appendix XII – Energy consumption inorganic fouling removal experiments

The energy consumption for experiment using air sparging, flowrate increase, and backpressure compared to the reference experiment (no cleaning) are shown in this appendix. Energy consumption was determined as shown in Appendix X – Energy consumption. Figure 42 shows the energy consumption for the experiments with air sparging (2 and 4 bar), compared to the reference.

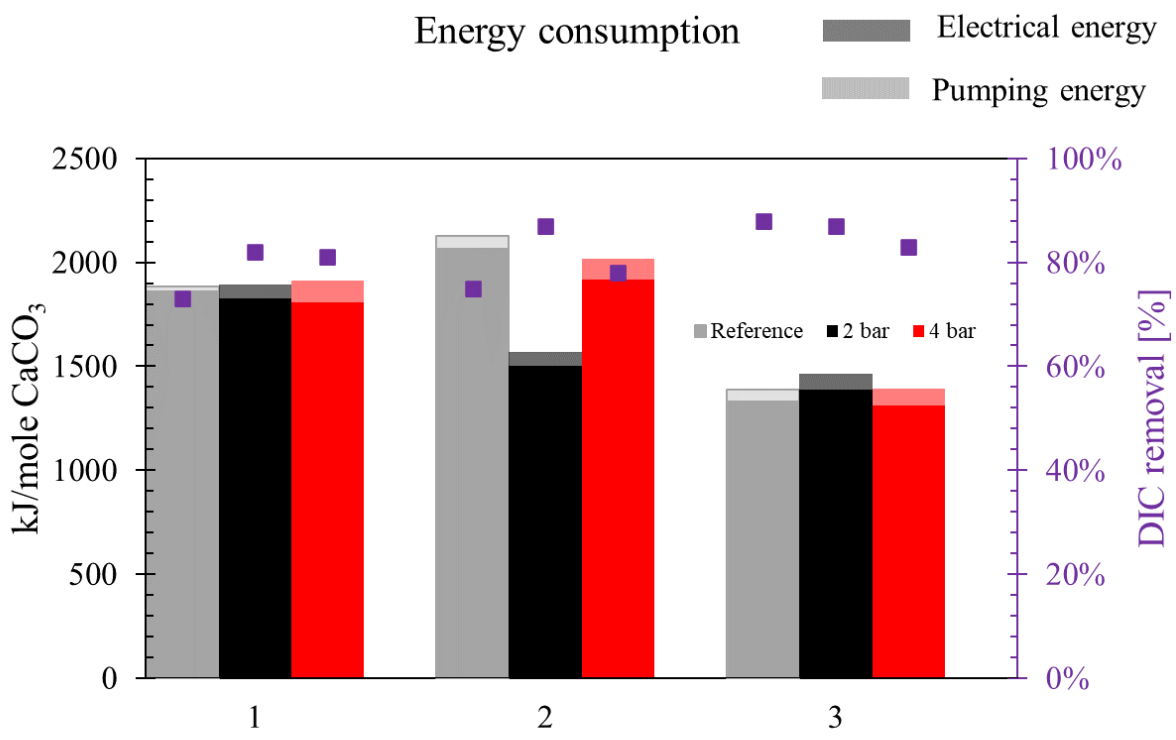

Figure 42, Energy consumption for the reference experiments, 2 bar and 4 bar, displayed separately for 3 experiments.

Only during experiment 2 the experiment with 2 bar showed a lower energy consumption, but this is attributed to the higher DIC removal for that experiment compared to the reference a 4 bar experiment.

Energy consumption for 2 experiments using back pressure application is shown in Figure 43.

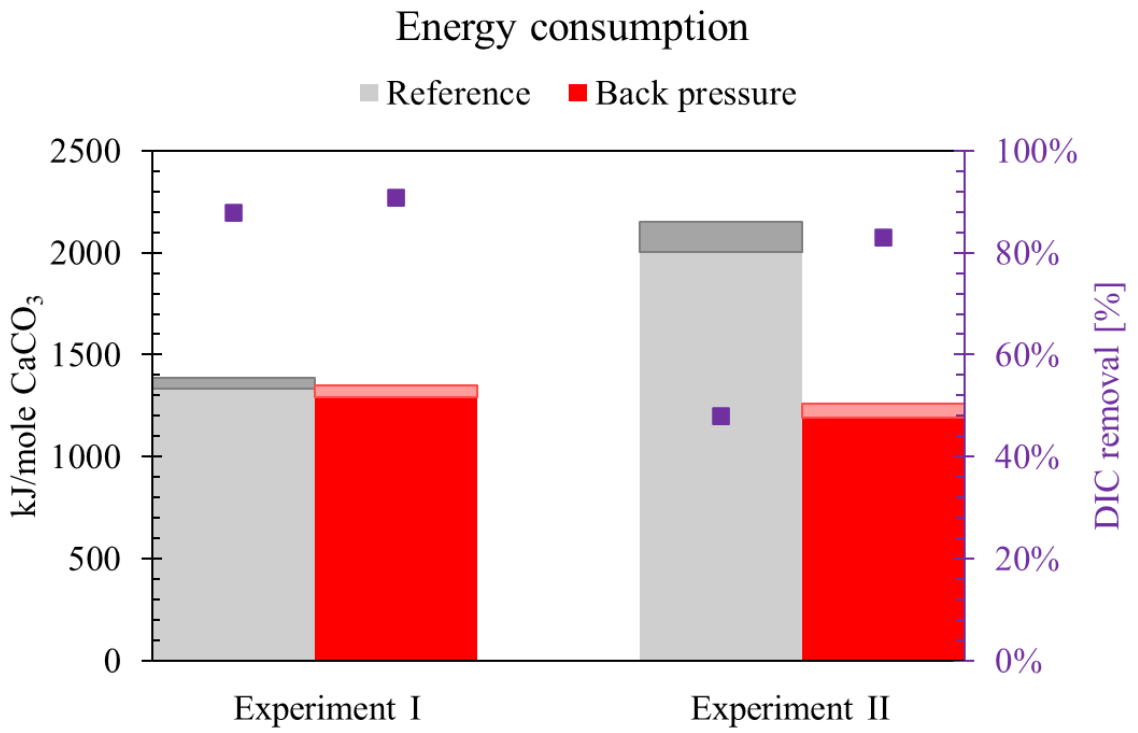

Figure 43 Energy consumption for the reference experiments compared to back pressure, displayed separately for 2 experiments.

Only during experiment II back pressure showed a lower energy consumption, but this is attributed to the low DIC removal for the reference experiment.

Energy consumption for 2 experiments using 5X and 15X flowrate increase is shown in Figure 44.

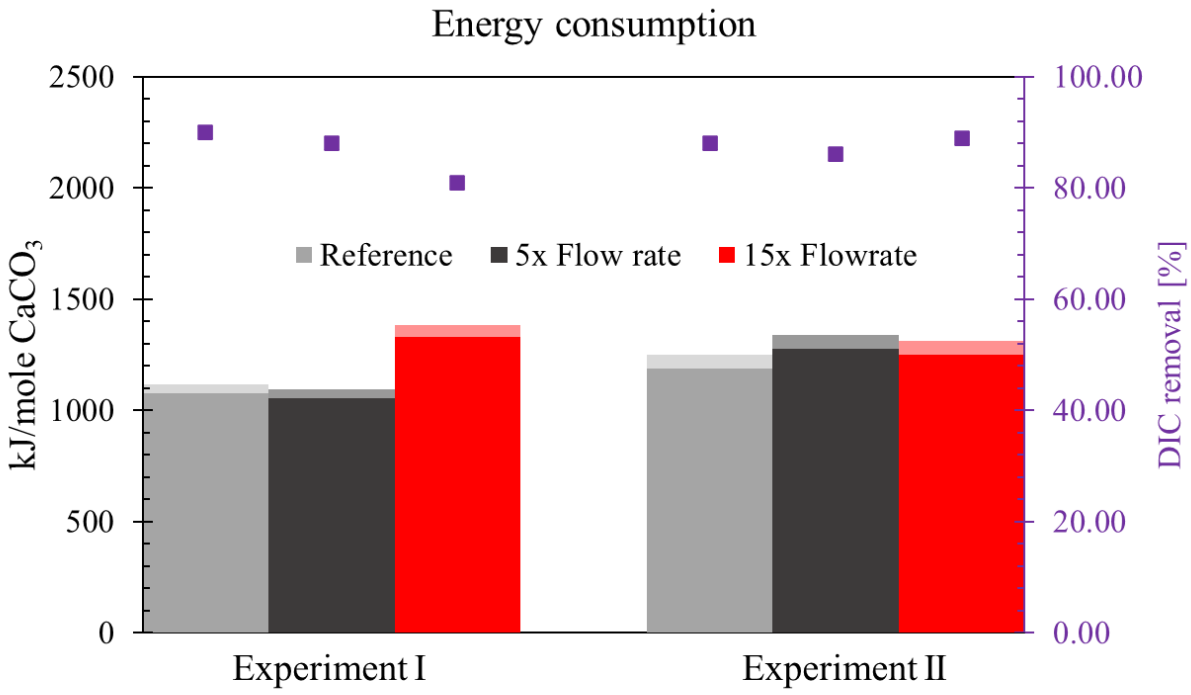

Figure 44, Energy consumption for the reference experiments compared to 5X and 15X flowrate increase, displayed separately for 2 experiments.

Only during experiment 1 the experiment with 15X flowrate increased showed higher energy consumption, but this is attributed to the lower DIC removal for that experiment compared to the reference and 4 5X flowrate increase.

Appendix XIII – Air sparging repetition 2, 3 and 4 bar

Figure 45 shows an air sparging repetition using 2, 3 and 4 bar and a reference experiment (no cleaning).

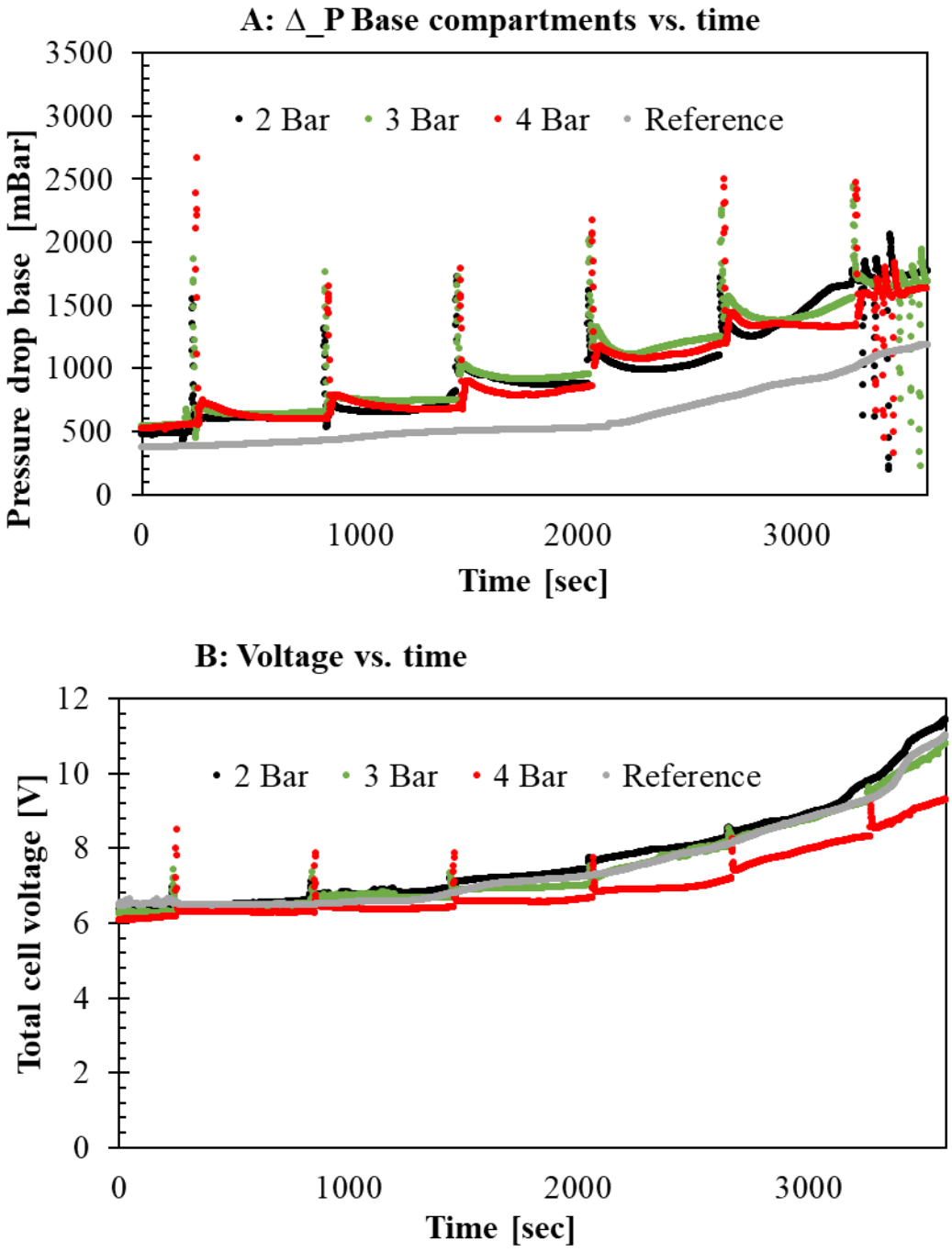

Figure 45, 1 A: pressure drop increase and B: total cell voltage increase for one repetition for air sparging experiments using 2 bar, 3 bar and 4 bar and a reference experiment (no cleaning).

Air sparging using 3 bar showed similar trends for voltage and pressure increase compared to 2 and 4 bar. Therefore, also sparging with 3 bar did not result in inorganic fouling removal.

Appendix XIV – Air sparging regimes

Based on literature, sparging 3x 2 seconds was expected to be more efficient than 1x 5 seconds. However, sparging with a 3x 2 seconds regime showed similar results as for 1x 5seconds, for 3 and 4 bar Figure 46.

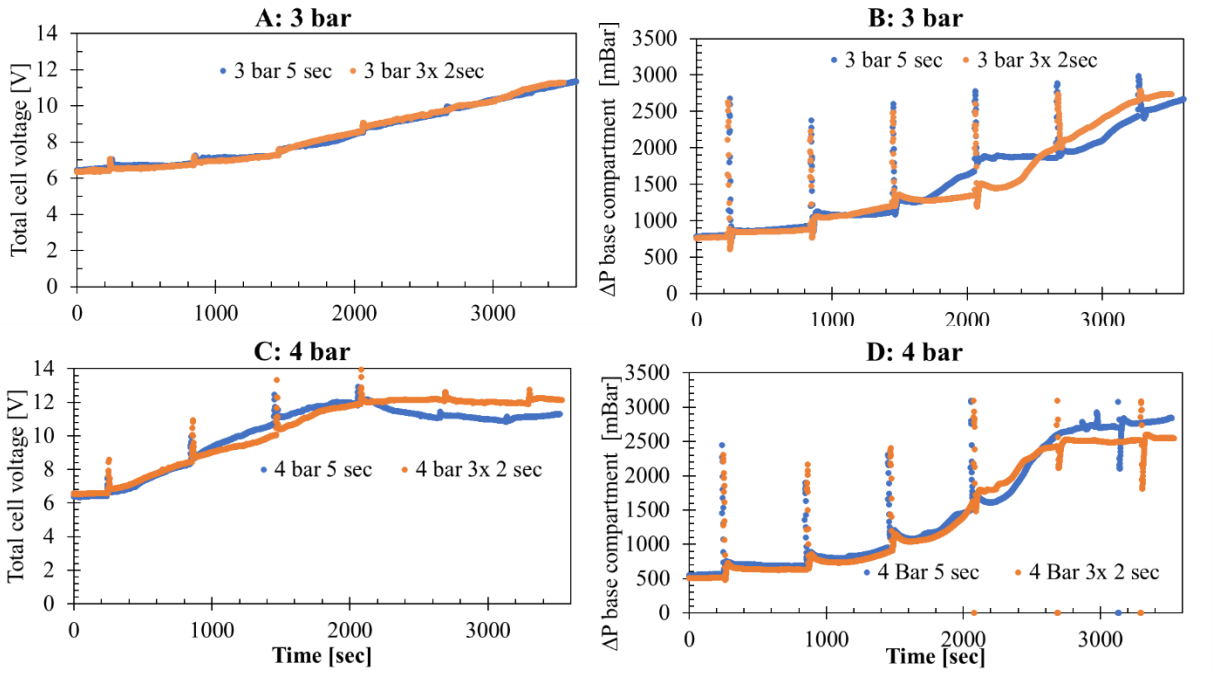

Figure 46, AB: comparing a 3x 2 seconds regime with a 1x 5seconds regime for 3 bar, for (A) voltage and (B) pressure drop. CD: comparing a 3x 2 seconds regime with a 1x 5seconds regime for 4 bar, for (C) voltage and (D) pressure drop.

Appendix XV – Air sparging with back pressure

Back pressure after air sparging was applied to remove stagnant bubbles from the cell stack. A comparison was made for air sparging experiments with 2 bar: sparging every 10 minutes 5 seconds with and without application of back after sparging. The results are shown in Figure 47.

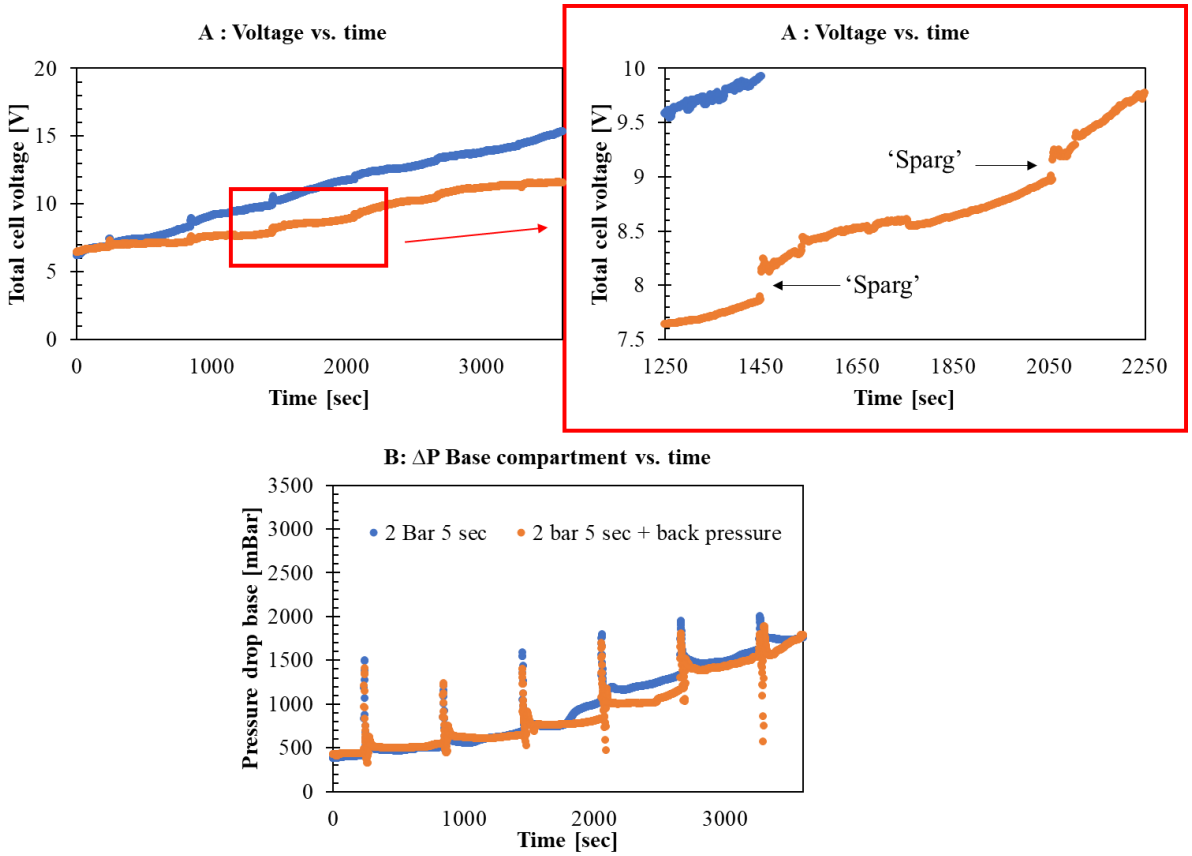

Figure 47 Comparing (A) voltage increase and (B) pressure drop increase for air sparging experiments with 2 bar: sparging every 10 minutes 5 seconds with and without application of back after sparging.

The pressure drop curves were similar with and without application of backpressure. The voltage increases for the repetition with backpressure increased less. However, observing the data of 3x 2seconds more close-up, it was observed that total cell voltage still increases after each 'sparg'. Therefore, it was not assumed that the lower voltage build-up was (entirely) a consequence of application of backpressure (also considering there was no effect on pressure drop).

Appendix XV – Acid wash

For each acid wash method (so 6 in total), 1 figure for pressure drop decrease during acid wash was shown. The acid wash with hydrochloric acid is shown in Figure 48.

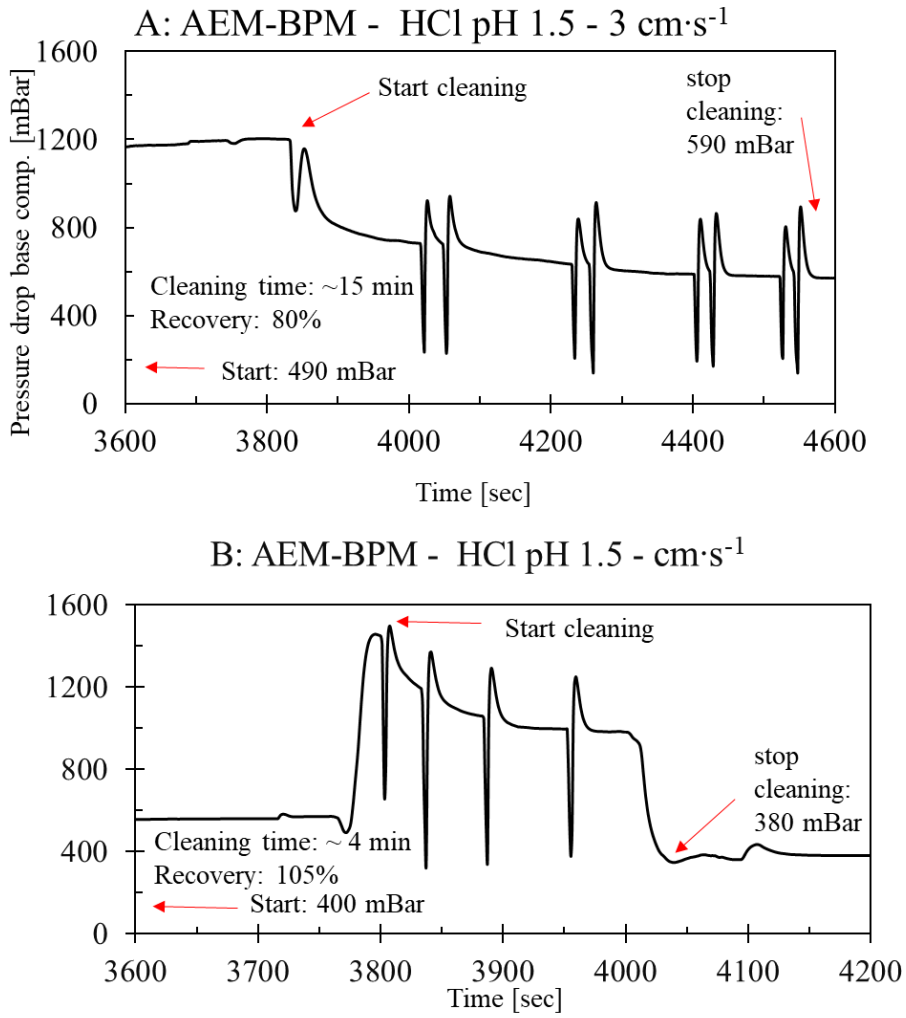

Figure 48, A: acid wash with HC1 (A) 1X operating flowrate and (B) 2X operating flowrate. The x-axis starts at 3600 seconds, because the first hour was used to 'scale' the membrane. The peak in the graph shows when the valve is opened again releasing build-up pressure.

After applying back pressure (a peak in the graph shows when the valve is opened again releasing build-up pressure), the decrease of pressure drop goes temporary faster. The cleaning was stopped (''stop cleaning time'), when pressure drop no longer decreased. The cleaning time is between start and stop.

Pressure drop curves during acid wash using acid produced by the bipolar membranes are shown in Figure 49.

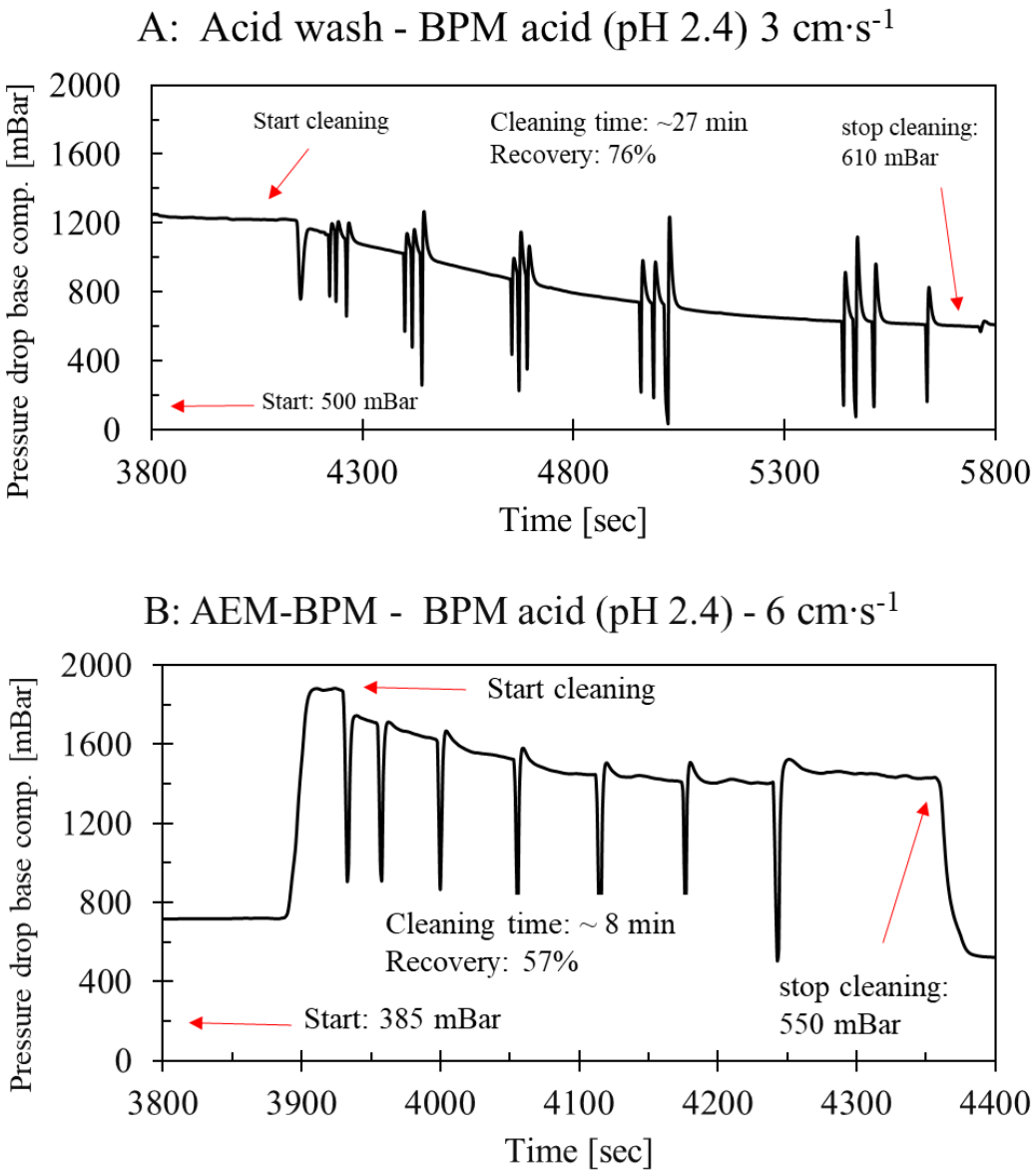

Figure 49, acid wash with BPM acid (A) 1X operating flowrate and (B) 2X operating flowrate. The x-axis starts at 3800 seconds, because the first hour was used to 'scale' the membrane. The peaks in the graph are the result of backpressure application. The x-axis starts at 3800 seconds, because the first hour was used to 'scale' the membrane.

A pressure drop curves during for the method where the based compartments were soaked in hydrochloric acid is shown in Figure 50.

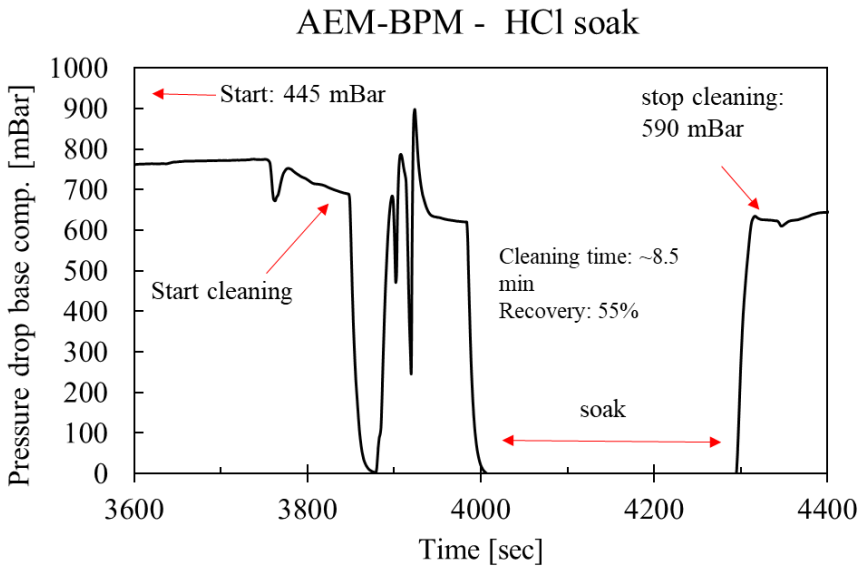

Figure 50, Soaking the base compartments in hydrochloric acid, during soaking the flow velocity and therefor the pressure drop is also . The peaks in the graph are the result of backpressure application. The x-axis starts at 3600 seconds, because the first hour was used to 'scale' the membrane.

A pressure drop curve during acid cleaning for a CEM-BPM configuration

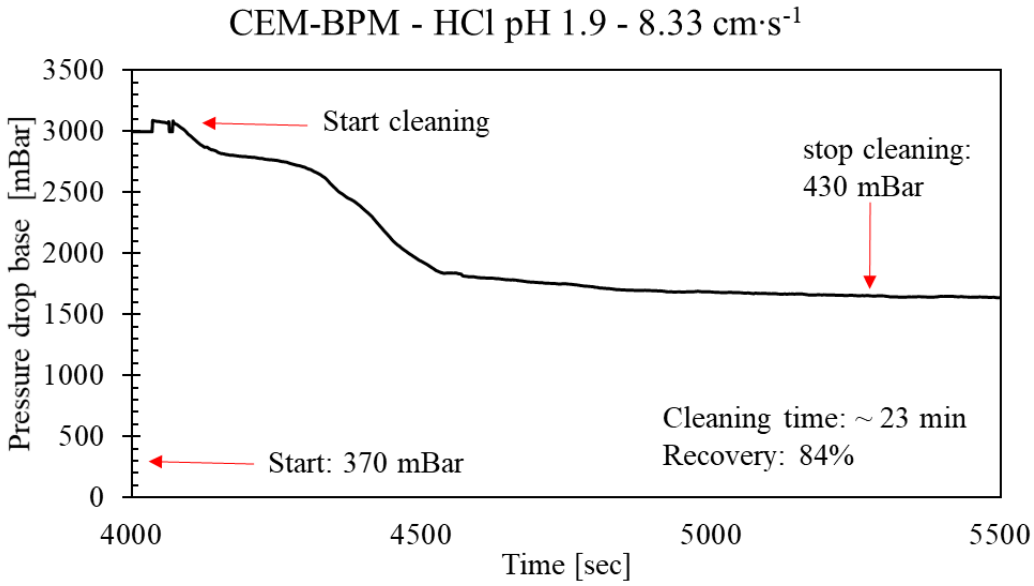

Figure 51, pressure drop curve during acid wash for CEM-BPM configuration. The x-axis starts at 4000 seconds, because the first hour was used to 'scale' the membrane.

Figure *48* - Figure *51* show how recovery of pressure drop (%) and cleaning time (in seconds) were determined based on the pressure drop. All values for recovery, cleaning time and chemical use are shown in below. The standard error of the mean was calculated as shown in Appendix VI – Average values synthetic seawater.

The amount of H^+ was calculated as followed:

$$Moles\ H^+used = \frac{Acid\ used\ (ml)}{1000} \cdot 10^{-pH} \qquad \text{Equation 27}$$

Acid used (mL) = cleaning time (min) ·flowrate (mL·min^{-1} per compartment) · $n_{compartments}$

HCl (pH 1.5) 6 cm·s^{-1}

Repetition	start ΔP	cleaning time	Acid used (mL)	Moles H^+ used	ΔP after cleaning	recovery (%)
1	558	00:08:01	3463	0.110	558	100%
2	539	00:05:49	2513	0.0795	652	79%
3	651	00:08:20	3600	0.114	623	105%
4	401	00:03:53	1678	0.0531	381	105%

	Moles H+	recovery	cleaning time
Average	0.0890	97%	00:06:31
STD error	0.0123	5%	00:01:16

HCl (pH 1.5) 3 cm·s^{-1}

Repetition	start ΔP	cleaning time	Acid used (mL)	Moles H^+ used	ΔP after cleaning	recovery (%)
1	491	00:15:00	3240	0.102	592	80%
2	339	00:08:00	1728	0.0546	403	81%

	Moles H^+	recovery	cleaning time
Average	0.0786	80%	00:11:30
STD error	0.0169	1%	00:02:28

BPM acid (pH 2.4) $cm \cdot s^{-1}$

Repetition	start ΔP	cleaning time	Acid used (mL)	Moles H^+ used	ΔP after cleaning	recovery (%)
1	592	00:29:32	11448	0.0456	754	72%
2	385	00:07:50	13824	0.0550	550	57%

	Moles H^+	Recovery (%)	Cleaning time
Average	0.0503	65%	00:18:41
STD error	0.0033	5%	00:07:40

BPM acid (pH 2.4) 3 $cm \cdot s^{-1}$

Repetition	start ΔP	cleaning time	Acid used (mL)	Moles H^+ used	ΔP after cleaning	recovery (%)
1	494	00:26:40	5724	0.0228	611	76%
2	611	00:32:30	6912	0.0275	798	69%

	Moles H^+	Recovery (%)	Cleaning time
Average	0.0252	73%	00:29:35
STD error	0.0017	2%	00:02:04

CEM-BPM HCl (pH 1.6 – 1.9) 8.33 $cm \cdot s^{-1}$

Repetition	start ΔP	cleaning time	Acid used (mL)	Mole H^+ used	ΔP after cleaning	recovery (%)
1	369	00:23:05	13800	0.174	429	84%
2	576	00:15:00	9000	0.226	673	83%

	Moles H^+	Recovery (%)	cleaning time
Average	0.200	84%	00:19:03
STD error	0.019	0%	00:02:51

Soak in HCl (pH 1.5)

Repetition	start ΔP	Cleaning time	Acid used (mL)	Mol H^+ used	ΔP after cleaning	recovery (%)
1	445	00:08:28	756	0.0239	647	55%
2	387	00:07:20	504	0.0159	620	40%

	Moles H^+	recovery	Cleaning time
Average	0.0199	47%	00:07:54
STD error	0.0028	5%	00:00:24

Appendix XVI – DIC and Ca^{2+} removal per method

The DIC removal and Ca^{2+} ions removal for each inorganic fouling removal method and AEM-BPM and CEM-BPM configurations is shown in Table *7*. The standard error of the mean was calculated as shown in Appendix VI – Average values synthetic seawater.

Table 7, DIC and Ca^{2+} removal for each inorganic fouling removal method and AEM-BPM and CEM-BPM

	DIC removal Average	**σ_{mean} DIC**	**Ca^{2+} removal Average**	**σ_{mean} Ca^{2+}**	**number of repetitions**
AEM-BPM	81%	1.2%	24%	0.7%	12
CEM-BPM	77%	5.9%	20%	1.9%	6
Air sparging 2 bar	85%	1.4%	15%	0.3%	3
Air sparging 3 bar	87%	0.7%	24%	1.9%	3
Air sparging 4 bar	81%	1.2%	21%	2.3%	3
Back pressure	87%	2.8%	21%	3.2%	2
5X Flowrate increase	87%	0.7%	25%	0.4%	2
15X Flowrate increase	85%	2.8%	25%	1.1%	2

Appendix XVII – SI values for pH > 12

The figures were made using Visual MINTEQ 3.1. As an input, the synthetic seawater as shown in Table 2 was used. By removing H^+ ions the pH was adjusted, this was done 14 times to make Figure 52 and Figure 53. The SI value per mineral was given in de output of the simulations. This Figure *52* is an extension on Figure *3*.

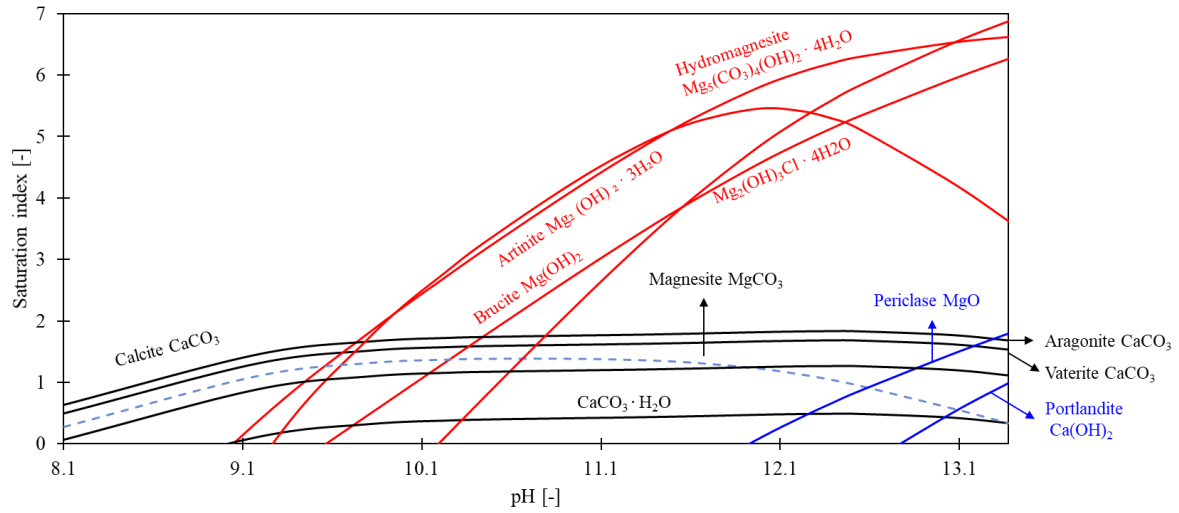

Figure 52, Saturation index (SI) for minerals for a pH >12. This figure is an extension of Figure 3. The lines were based on 14 simulations.

Figure 53 shows the saturation index < 0, for sulphate containing minerals.

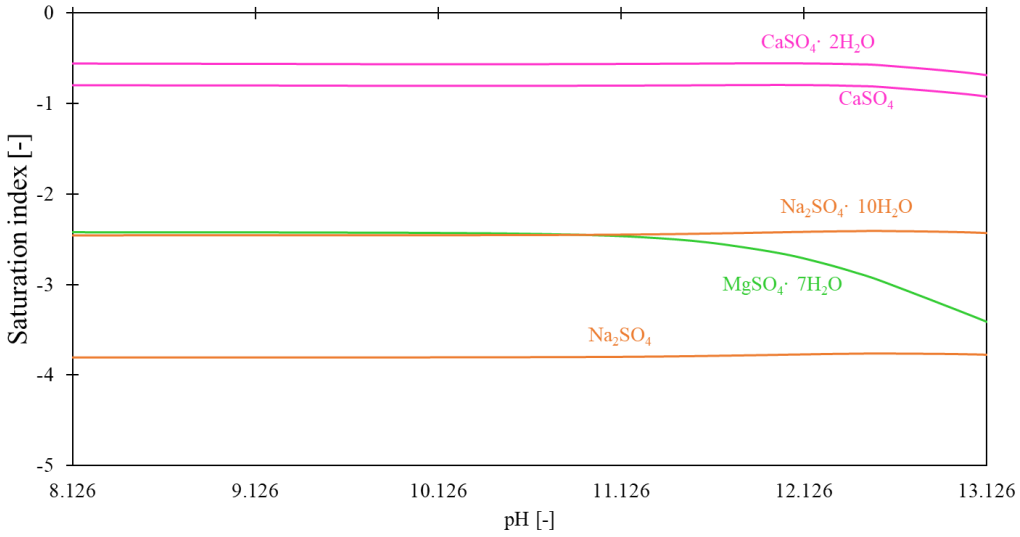

Figure 53, Saturation index (SI) for sulphate containing minerals for a pH >12 and an SI < 0. The lines were based on 14 simulations.

Appendix XVIII – solubility of pure salts

Solubility of pure salts are shown in the table below.

Table 8, Solubilities of salts in pure water (18-25 °C) g/L. Black values from (Salinas et al., 2021), Green values from (Lide, 2000) (the – mean that the salts was reported in the source, but no solubility value was given), orange value from: https://www.chemicalbook.com/ChemicalProductProperty_EN_CB2780364.htm. The grey box means a salt in that combination was not found.

g/L

	Na^+	Ca^{2+}	Mg^{2+}	K^+	Sr^{2+}
Cl^-	360	730	560	330	510
SO_4^{2-}	170	2.0	350	310	0.110
CO_3^{2-}	190	0.013	1.0	1080	0.011
Br^-	946	1560	1020	678	1070
BO_3^{3-}	-	27			
F^-	45	0.016	0.076	930	0.010
SiO_3^{2-}	-	-	-		

Table *8* was 'remade' salts in 'typical seawater' according to Lenntech B.V. which is shown in Table *9*. The concentrations were based on the ionic compound with the lowest concentration (e.g., when looking at the concentration Cl and Ca^{2+} in seawater in mole/L, the value of 1.11 g/L was based on the Ca^{2+} concentration). Red marked values exceed the concentrations in Table *8*.

Table 9, the maximum concentration of a salt in seawater (g/L), based on the ionic compound of a salt with the lowest concentration. Red marked values exceed the concentrations in Table 8. Concentrations were based on typical sweater values according to Lenntech B.V.. The green – mean that the salts were reported in the source, but no solubility value was given. The grey box means a salt in that combination was not found.

g/L

	Na^+	Ca^{2+}	Mg^{2+}	K^+	Sr^{2+}
Cl^-	27	1.1	4.9	0.73	0.023
SO_4^{2-}	3.9	1.4	3.3	4.8	0.027
CO_3^{2-}	0.25	0.23	0.20	0.32	0.022
Br^-	0.08	0.16	0.15	0.10	0.04
BO_3^{3-}	-	0.10			
F^-	0.0022	0.0041	0.0033	0.0031	0.0066
SiO_3^{2-}	-	-	-		

Appendix XIX – AEM-BPM experiment 120 minutes

The experiment ran with the following configuration: + AEM-AEM-BPM-AEM-BPM-AEM-BPM -. As electrode rinsing solution, 0.25 M FeCl2 + 0.25 M FeCl3 was used. The applied current density was 12.5 mA·cm^2 and 72 mL·min^{-1} per compartment. This experiment was not used in the results but was an experiment that was done in the *'try-out phase'* for the AEM-BPM configuration. However, it was the longest experiment done with an AEM-BPM configuration. The results for voltage- and pressure drop increase are shown in Figure 54 and Figure 55.

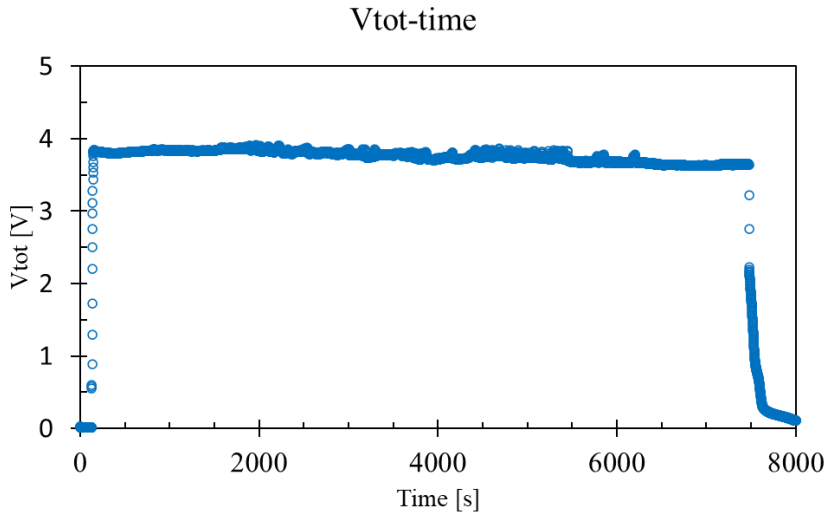

Figure 54, Total cell voltage increase for a 120 minute experiment with 12.5 mA·cm^2 and 72 mL·min^{-1} per compartment for an AEM-BPM cell pair configuration.

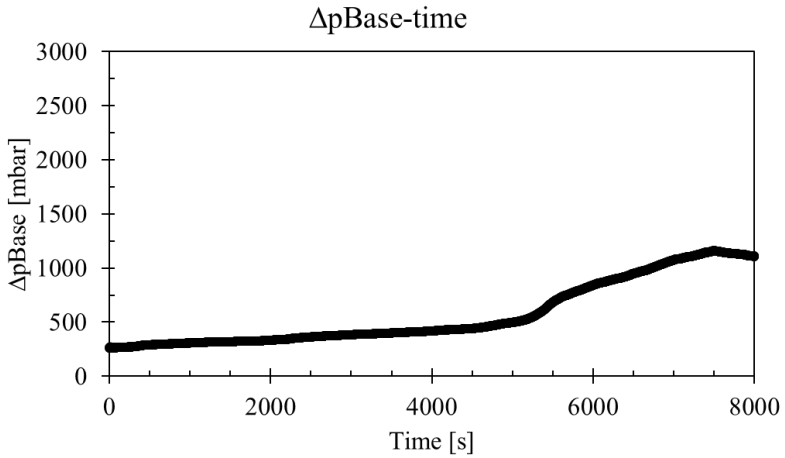

Figure 55, pressure drop increase over the base compartments with 12.5 mA·cm^2 and 72 mL·min^{-1} per compartment for an AEM-BPM cell pair configuration.